Valsts pētījumu programma

„INOVATĪVO DAUDZFUNKCIONĀLO MATERIĀLU, SIGNĀLAPSTRĀDES UN INFORMĀTIKAS TEHNOLOĢIJU IZSTRĀDE KONKURĒTSPĒJĪGIEM ZINĀTŅU IETILPĪGIEM PRODUKTIEM"

Projekts Nr. 2 „Inovatīvas signālapstrādes tehnoloģijas viedu un efektīvu elektronisko sistēmu radīšanai"

vadītājs Dr. M. Greitāns

INFORMATĪVĀ ATSKAITE PAR PROJEKTA OTRĀ ETAPA REALIZĀCIJU

(2011. gada janvāris - decembris)

PASŪTĪTĀJA līguma uzskaites Nr. 2011.-10-4/VPP

Programmas vadītājs: Dr.habil.phys. A. Šternbergs, LU Cietvielu fizikas institūts

Projekta vadītājs: Dr. sc. comp. M. Greitāns, Elektronikas un datorzinātņu institūts.

ELEKTRONIKAS UN DATORZINĀTŅU INSTITŪTS

INSTITUTE OF ELECTRONICS AND COMPUTER SCIENCE

Table of Contents

1 Notikumu reģistrācijas moduļu izstrāde uz specializētas mikroshēmas bāzes un tās eksperimentālie pētījumi jaunu digitālas apstrādes algoritmu pārbaudei

The event timing is simply a measuring of time at instants when some pulses (events) arrive at the input of a measuring device. Conventionally the devices of such kind are called event timers. The modern event timers can provide such measurement with picosecond precision at pulse rate up to tens of MHz, and gradually become basic timing devices for various applications.

There is a method for high-precision event timing (called EET-method) which is based on digital processing of specific analog signals generated in response to input events [1.1]. Practical implementation of this method has allowed achieving the performance characteristics quite comparable with the world's best event timers currently available [1.2]. The event timers based on EET-method comply with all requirements of latter-day event timers. In addition, replacement of usually intricate analog circuits by widely used DSP tools allows to significantly simplify the timer's hardware, resulting in higher integration and lower unit cost. That affords grounds to speak about innovative technology for creating a new generation of compact, high-performance, and reasonably priced event timers.

Applied potential of EET-method is very wide and further improvement of technologies based on this method seems very promising and quite practicable. For these reasons we are continuing R&D activity in this area, and this annual report briefly represents the current results of such activity. The main object of this year activity is the event timing module development with improving of timing technologies and using of modern chips.

During this period the following problems were researched:

- high-precision event timer calibration
- correction function temporal stability
- secondary signal processing dependence on signal variation
- digital functions integration in one chip
- event timing module implementation and approbation
- short-distance transmission of event timing information

The first problem solving allows defining the nonlinearity correction function minimizing expenditure of time and computing resources. The correction function stability means that external environment variation in time and temperature has minimal influence on the measurement precision. Solving of the third problem allows to get the same results, but with other methods. The forth and fifth problems solving is dedicated to compact event timing module development. And the last problem is related to the effective event timing information transfer at short distances.

1.1 High-precision event timer calibration problems

Event timers based on EET-method contains a special Time-to-Digital Converter (TDC), which is responsible for the interpolation measurement within the period T_R of the

master clock. For any event that occurs at the instant t_j, the TDC converts the value $\tau_j=t_j(\mathrm{mod}T_R)$ to its digital estimate $D_j=F(\tau_j)$. Conversion of all possible τ_j values is defined by particular TDC transfer function.

The TDC implementation is quite simple since it contains only an edge-triggered pulse shaper and a typical Analog-to-Digital converter. However this advantage is accompanied by considerable integral non-linearity of TDC transfer function [1.3] that is caused by a non-linearity of the shape signal being digitized. Specifically, for typical TDC implementations such non-linearity can reach unacceptable level of hundreds picoseconds (Figure 1.1).

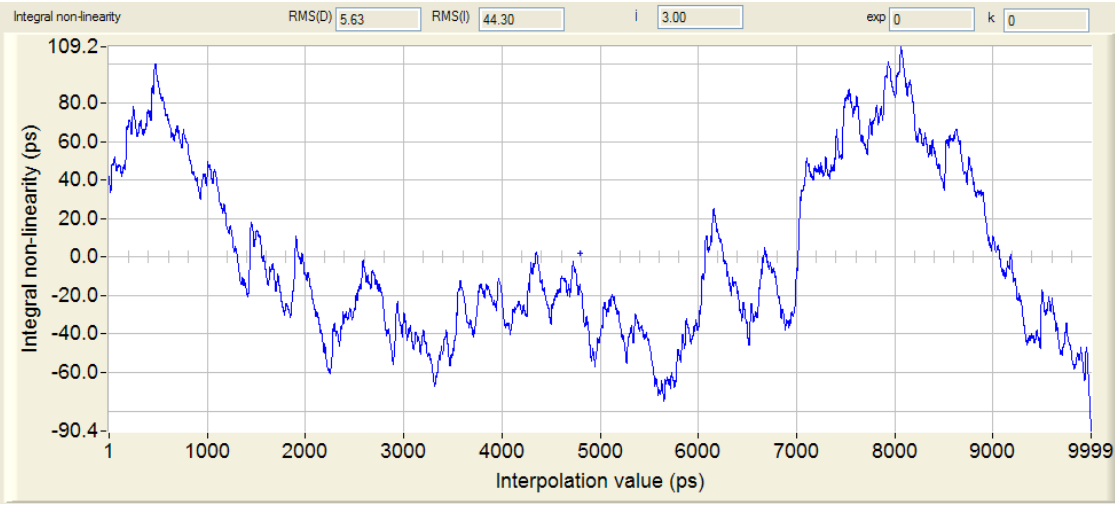

Fig.1.1. Typical TDC non-linearity error over 10 ns interpolation interval.

Correspondingly the key operation of EET-method is a digital correction of this non-linearity. Such correction is based on the using of the experimentally predetermined correction function $F_C(D_j)$ which is mirrored to the actual TDC transfer function (Figure 1.2).

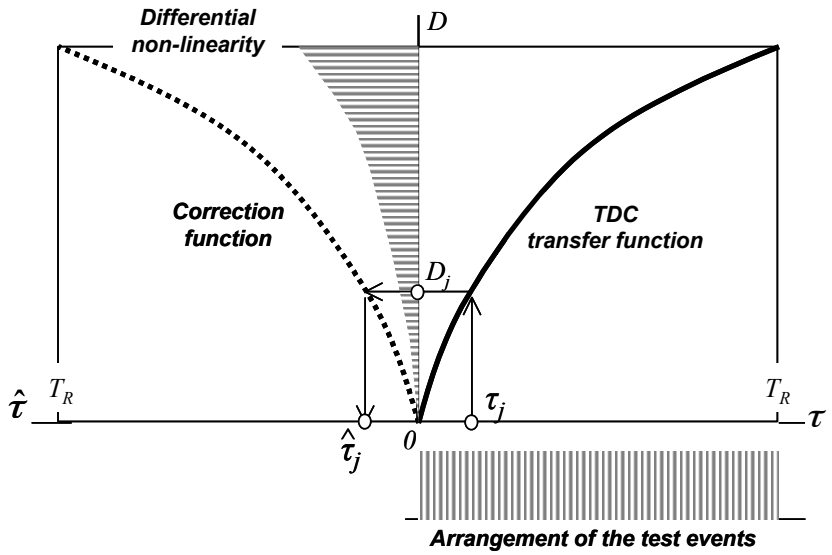

Fig.1.2. The TDC transfer function and nonlinearity correction function.

In this case the estimate D_j is converted to estimate $\hat{\tau}_j$ where the nonlinearity error is subtracted. In this way initial TDC nonlinearity error can be reduced many times. However, it is possible only if the correction function adequately reflects actual non-linearity of the TDC transfer function.

For high-precision event timers the correction function predetermination (also referred to as TDC calibration) should be performed with picosecond precision. In addition, taking into account a possible time and temperature instability of the TDC transfer function, the TDC calibration should be performed expeditiously to trace such instability, when it is necessary using built-in calibration means. The problem is to find the best technique for such TDC calibration.

There are various approaches to TDC calibration, including well-proved approach based on generation of a special sequence of test pulses [1.4]. In this case it is assumed that the instants $\{\tau_j\}$ of the test event occurring will be arranged within the interpolation interval T_R nearly uniformly and with sufficiently high density. Under this condition the histogram of digital values $\{D_j\}$ will reflect the differential TDC nonlinearity (Figure 1.2). Then the corresponding correction function (reflecting the integral TDC nonlinearity) can be constructed by direct summation of the normalized frequencies $\{f_i\}$ of the $\{D_j\}$ realizations:

$$F_C(D_j) = T_R \sum_{i=1}^{j} f_i \ . \tag{1.1}$$

Evidently the achievable precision of such TDC calibration depends mainly on the proper arrangement of the test events, i.e., high uniformity and high density of the instants $\{\tau_j\}$ distribution. Possible techniques for such test event generation with required properties will be considered below.

1.1.1 Vernier technique

The first (Vernier) technique is based on a generation of low-jitter test pulses with the period

$$T_G = kT_R + \Delta_T, \tag{1.2}$$

where T_R is the master clock period, k is an integer, which results in time interval kT_R greater than the TDC "dead time", and Δ_T – the predefined step between adjacent events.

In this idealized case a sequence of $M=T_R/\Delta_T$ test pulses provides required uniform arrangement of the instants $\{\tau_j\}$. The main advantage offered by this technique is the smallest time of TDC calibration, but its practicability for the calibration with picosecond precision is doubtful.

For example, let us assume that the step Δ_T = 1.0 ps, master clock period T_R = 10 ns, and the "dead time" = 50 ns. These parameters are near to the case of practical implementation of the EET-method. Than k = 5 and M = 10000. In this case the minimal time for calibration will be 0.5 ms and the test pulses should be related with the master clock frequency with stability at the level of $2 \cdot 10^{-6}$, and this is quite possible if the test pulse generator has not own instabilities. But any instability of the generator requires checking and repeating the generation, and, correspondingly, increases the time for calibration, and dramatically increases requirements to relative stability of generator and master clock. Achievement of such stability represents a complicated engineering task and seems currently unavailable.

Theoretically it is very attractive to use the modern Direct Digital Synthesis (DDS) Generators for Vernier technique. Such chips use the external reference signal and may provide very fine phase offset adjusting for the synthesized frequency relative to the external reference. It seems that, if we set the synthesized frequency $F_G = 1/kT_R$, then we can accumulate interpolation code statistics for each preset phase (Figure 1.3).

If this process is repeated with the step of phase shifting, providing picosecond resolution for interpolation values, we will get the full correction function. All this would be perfect if the DDS did not have such big phase jitter of analogue outputs and the statistic distribution were normal. But both these requirements are currently unavailable. Moreover the best known chips AD9835 and AD9959 from Analog Devices, Inc. have only 12 and 14 bits for the phase offset adjusting. This provides for $F_G = 1/kT_R$ = 1/50ns the step = 12 and 3 ps, correspondingly, but theoretically they have 32-bit phase accumulation register and it can provide 12 attoseconds (!).

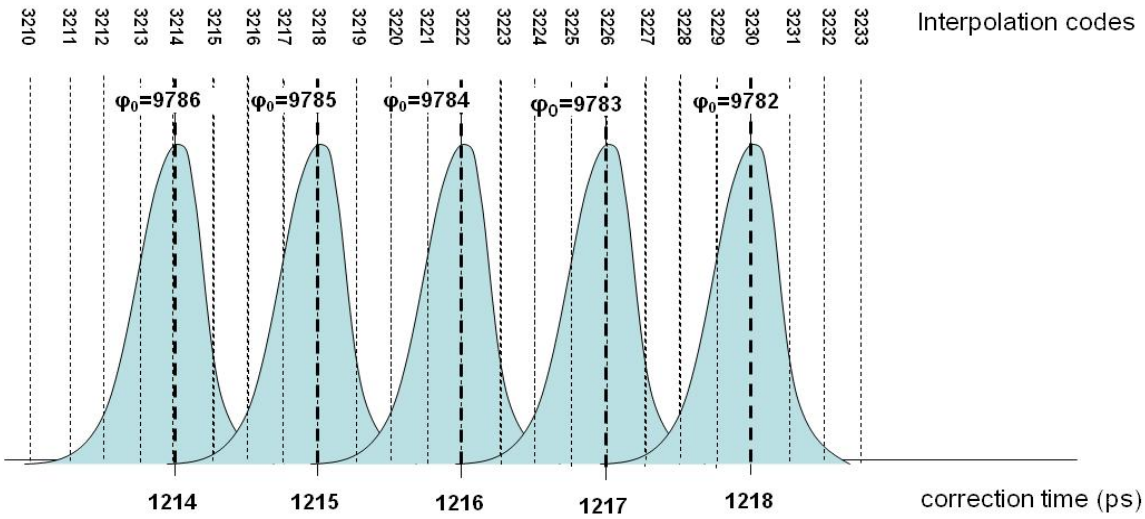

Fig.1.3. Statistic accumulation for each step of phase shift between the generated frequency and the master clock

1.1.2 White noise generator

The second technique is based on the test pulse generation with deliberately unstable repetition period. Taking into account conversion of such period to the instants $\{\tau_j\}$ by modular operation, actually it can be close to true statistical testing. This technique is simple for implementation, but supposedly needs a very large amount of statistical data to achieve required precision of TDC calibration.

To analyze practicability of this technique we used computer simulation that imitates all steps of correction function constructing under near real parameters of test pulse sequence. TDC transfer function is assumed as strongly linear so that integral nonlinearity of the correction function (namely, standard deviation of nonlinearity errors) reflects the quality of TDC calibration (Figure 1.4).

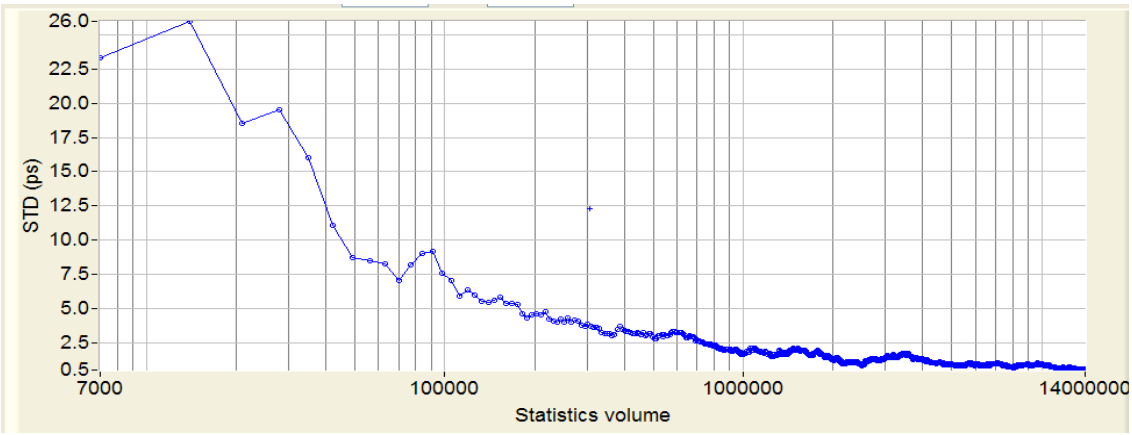

Fig.1.4 Standard deviation of non-linearity error versus statistic volume

In the Figure 1.4 the calibration precision dependence on statistic volume is shown for generator having the random jitter 10 ns (period jitter more than 14 ns !). To evaluate the

time needed to get the good calibration precision the data for three different random jitter values are shown in the Table 1.1.

Table 1.1 The time of calibration to get the good precision.

Randoms jitter (ns)	Calibration error < 1.0 ps		Calibration error < 0.6 ps	
	Statistic volume (M)	Calibration time (s)	Statistic volume (M)	Calibration time (s)
2	15	0.75	110	5,5
4	12	0.6	70	3,5
10	5	0.25	25	1,25

It should be taken into account, that this evaluation is done for the minimal possible period of calibration generator equal to „dead time". For the Riga event timer A033-ET the period of scaling generator about 16-17 us is chosen, taking into account the interval nonlinearity of the TDC. In this case the time of calibration lies in the range of 10 - 30 minutes, which is too much for expeditious TDC calibration.

1.1.3 Off-The-Shelf generators

Commercially available Off-The-Shelf (COTS) is a term defining a nondevelopmental item of supply that is both commercial and sold in substantial quantities in the commercial marketplace. It will be very attractive if there are such Off-The-Shelf generator chips that can be used for the TDC calibration and may offer significant savings in procurement, development, and maintenance.

There are many generator chips, having a great variety of frequencies, stabilities and other parameters. A choice problem is "What parameters are important and what values they should have?".

To make the choice let us consider an idealised case of pulse sequence with a constant period T_G. The instants $\{\tau_j\}$ of corresponding events occurring are defined as follows:

$$\{\tau_j = (\tau_{j-1} + T_G) \bmod T_R. \tag{1.3}$$

It is obvious that an arrangement of the events essentially depends on the period T_G. For example, if the generator period is equal to T_R and it has small random jitter $\sigma >> T_R$ than all events will have the normal distribution with parameter σ and the correction function F_C will be wrong and actually defined in narrow range (5σ - 6σ). The same can be sad about the periods equal to $T_R/2$, $T_R/3$, and so on. To verify an existence of the "bad" T_G values we do experiments with our event timer A033, using a slight adjusting of a frequency of generator chip EXO [1.4]. For each adjusted period we make the calibration of the A033 and evaluate a measurement error. It can be seen (Figure 1.5) that this error significantly varies depending on the calibration generator period.

At the same time the number of "good" frequencies is big, too. However, generally, the realisation of "bad" value T_G is not excluded absolutely. So there is a particular task to detect and avoid such cases. To solve this task, it was supposed that normally two separately obtained correction functions should be similar. If such similarity is not observed, probably it is caused by realisation of "bad" value T_G, i.e. by spurious bursts in

estimation of the differential non-linearity. In this case the frequency of test pulse source should be slightly corrected, and the TDC calibration is performed once more. The acceptable level of similarity can be defined empirically so that in average not more than some defined part of TDC calibrations could be detected as “bad” ones.

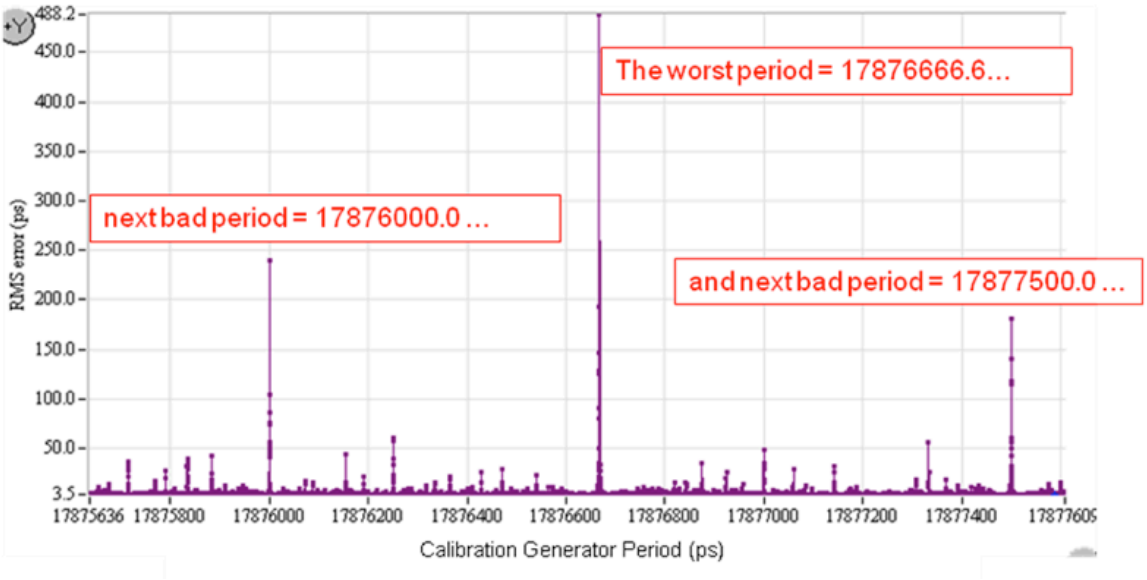

Fig.1.5 Measurement error dependence on calibration generator period

Application of this technique has allowed achievement of calibration precision at picosecond level using the test pulse sequence with not more than 150 000 pulses (Figure1.6). In this case the average time of TDC calibration does not exceed 15 seconds, which is quite allowable for its expeditious application.

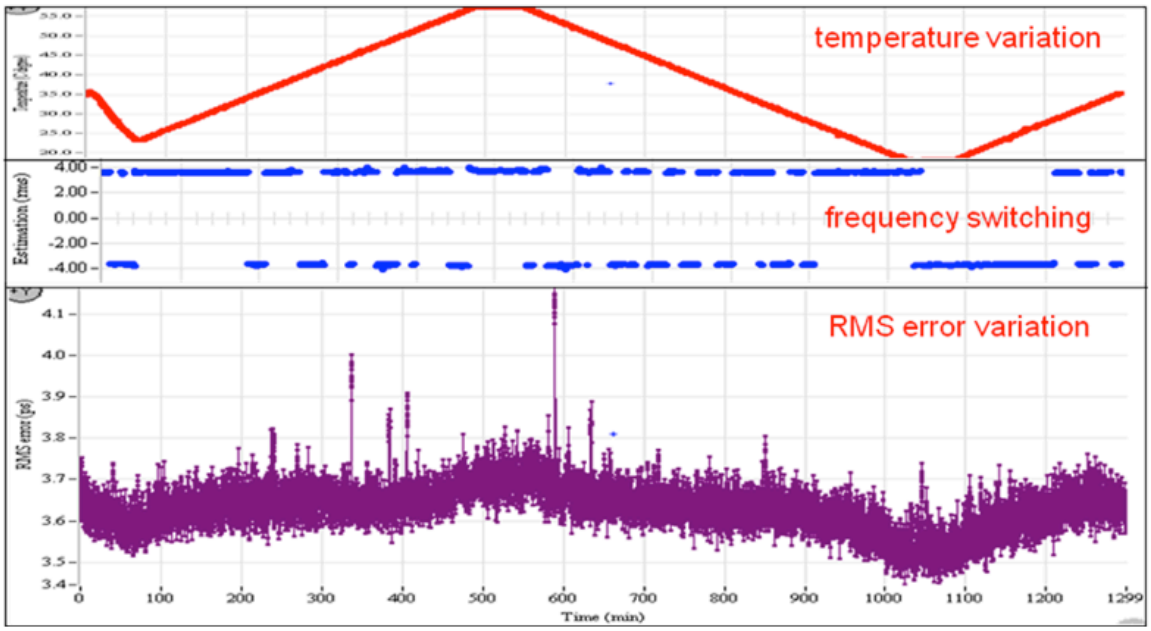

Fig.1.6 Calibration quality testing in temperature range 5 – 45 ^{o}C

A temperature is a main factor effecting on period. As result the „bad" values of period practically are inevitable. In last models of Riga event timer the calibration generator EXO has 1-bit controllable adjusting, which swithes the period between two values, differing for 5-7 ps. To control this switching the following procedure is used. All digital values $\{D_j\}$ presenting instants $\{\tau_j\}$ of the events from the calibration generator are divided into two sets and for each set the correction function (1.1) is built. If these functions are similar, it is supposed that they are "good" and they are merged into one correction function. In other case the calibration generator is switched to adjust frequency. The result of the measurement error estimation (Figure 1.6) presents the calibrations under external temperature variation in the range from 5 up to 45 ^{o}C. The bottom plot shows the measurement error for calibration, which was made under temperature, shown in the upper plot. The middle plot shows the switching of the calibration generator.

The offered technique of TDC calibration combines simplicity of its implementation with relatively high performance. Effectiveness of this technique has been tested experimentally in a number of event timers. Specifically, the event timers employing such calibration have provided the timing RMS precision in the range 2.5-3.0 ps, where fraction caused by the errors of TDC calibrations does not exceed 15%.

1.1.4 Locked Loop generators

The above empirical approach provides the best resolution "almost always", but it cannot exclude the worse result in some specific conditions. To avoid this it is preferable to keep the calibration generator frequency in a narrow range, which does not include the "bad" values for calibration. Such technique is known as the Locked Loop generators. We consider two types of such generators:

- Frequency Locked Loop (FLL) based generator and
- Phase Locked Loop (PLL) based generator.

Because such technique allows realization of any function it is necessary to define the "good" period value and stability parameters of developed generators.

To simulate the calibration pulse sequence we concern a theoretical model of clock oscillators and experimental evaluation of its parameters [1.5]. In particular, we suppose that high-performance clock oscillator is used for the event sequence generation to build the correction function, and the simulation model of this oscillator is defined as follows:

$$\{t_k = kT_G + \sum_{i=1}^{k} \Delta_i^A + \Delta_k^S \}_0^N , \tag{1.4}$$

where k is serial number of event, T_G – event generation period (an average), Δ_i^A - accumulative jitter component (A-jitter) and Δ_k^S - superimposed (non-accumulative) jitter component (S-jitter) of event sequence.

The "good" period must provide the uniform distribution in the master clock interval T_R all instants $\{\tau_j\}$ for the generated events. In case of an ideal generator the uniform distribution can be ensured if

$$mT_G = kT_R , \tag{1.5}$$

where m and k are integers with no common factors.

For example, if we want to get 1 ps step for these instants we take m = 10000, which has only two factors 2 and 5. The second integer may be, for example, k = 50001 or 53137,

taking into account the "dead" time 50000 ps for TDC and 3137 as a prime number. In result we get the corresponding periods:

$$T_G = 50001 \text{ ps and } T_{G'} = 53137 \text{ ps.} \quad (1.6)$$

The first period we name as Vernier generator (one can see the analogy with part 1.1.1), and the second period we name as pseudo-random (PRand) generator (the events in generated sequence will be distributed almost randomly in accordance with (1.3)). But as mentioned above this is the "good" period for the ideal generators, which hasn't S-jitter or A-jitter. To evaluate the impact of these jitters on the nonlinearity error we simulate the calibration generators with periods (1.6) and for different values of A- and S-jitters. In jitter existence circumstances it is obvious that we could not get by one pass through the interpolation interval (Table 1.2).

Table 1.2. The nonlinearity errors calculated from the simulation

10000 events			100000 events		
AJ (ps)	Vernier (ps)	PRand (ps)	AJ (ps)	Vernier (ps)	PRand (ps)
0.0	0.5	0.5	0	0.5	0.5
0.2	12.8	0.9	0.2	1.6	0.9
0.4	26.1	1.8	0.4	3.4	1.8
0.6	39.6	3.1	0.6	5.5	3.1

The impact of S-jitter in the reasonable range up to 5 ps on the nonlinearity error is apparent only in case of A-jitter equal to 0. If A-jitter is more than 0 it becomes deciding. For this reason for data in the Table1.2 S-jitter is fixed at the value 3.0 ps and the nonlinearity errors are calculated for four values of the A-jitter. In the left part of the Table 1.2 the nonlinearity error estimates are for minimal statistic volume, and in the right part – for ten times greater volume. The simulation results show that in all cases the pseudo-random generation is better.

We made experiments with A033-ET, taking as the calibration generator a low-jitter VCO from Fordahl Inc. and adjusting its period T_G in the range from 17876950 ps up to 17877600 ps with the step 1 ps. For each preset period the calibration was done and at this calibration the measurement error was estimated (Figure 1.7).

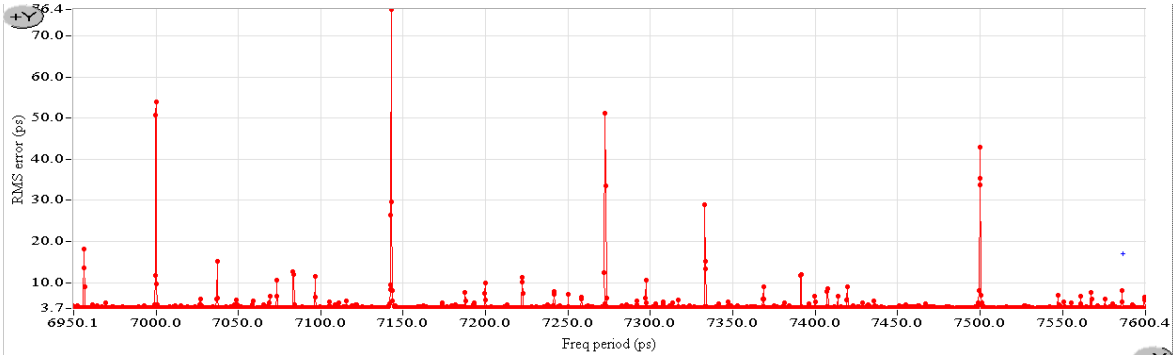

Fig.1.7. The measurement error dependence on the calibration generator period.

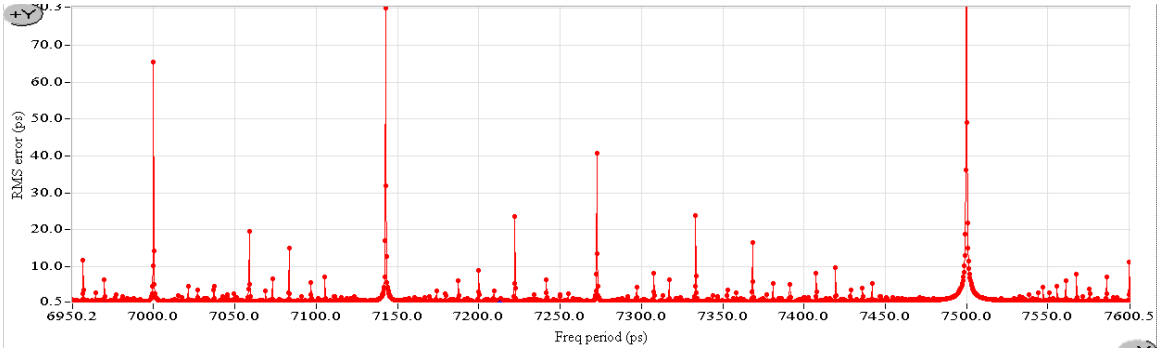

Fig.1.8. The nonlinearity error dependence on the simulated calibration generator period.

To compare the experimental data with the simulation data the calibration generator with Δ_k^S = 2.0 ps and Δ_i^A = 0.3 ps in the same range was simulated. For each period with 1 ps step the nonlinearity error was calculated (Figure 1.8).

As can be seen the simulation result shows a good coincidence with the experimental one, taking into account a complexity of functional relation between the measurement error and nonlinearity error. Such simulation allows finding the "good" frequency value for the developed FLL- or PLL-based generator and defining acceptance limits for A-jitter and S-jitter.

Frequency Locked Loop generator. To check an efficiency of the FLL-based calibration generator a small module (40x50 mm) was developed. As can be seen from this module block diagram (Figure 1.9) there are two inputs from the main control FPGA of the event timer and one output with calibration signal.

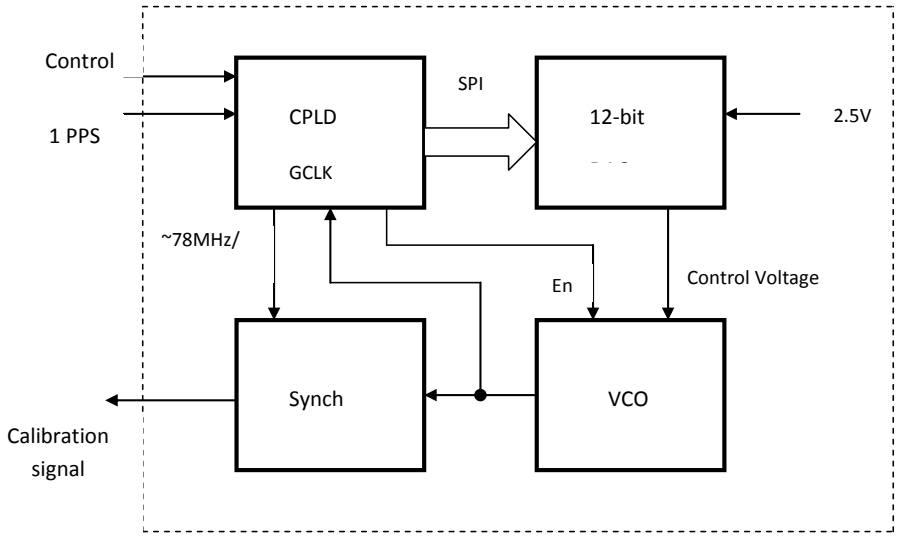

Fig.1.9. Block diagram of the FLL-based calibration generator

The plug-in connector of the module allows replacing the existing EXO-type calibration generator by this module. The input signal 1PPS is produced by the special logic block in the main FPGA of the event timer and provides the adjusting of the calibration signal period to the "good" value.

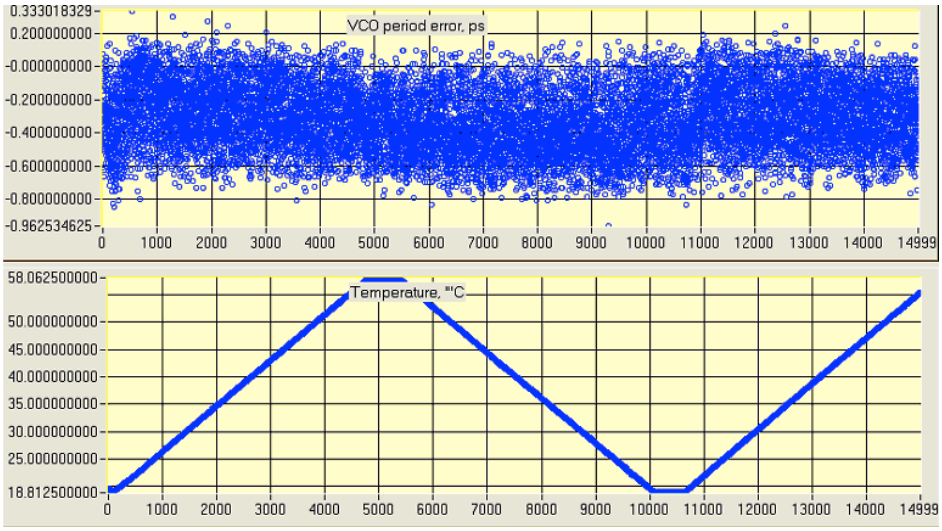

Fig.1.10. The temperature stability of the FLL-based calibration generator.

The calibration generator period stability in the wide external temperature range from 5 ^{o}C up to 45 ^{o}C is very good (in Figure 1.10 in the bottom plot an internal temperature is shown). The upper plot in Figure 1.10 shows the averaged values on the set of 1000 periods. Period jitter for this FLL generator, taking into account very slow temperature change (0.1^{o}C/min) is about 4 ps.

Phase Locked Loop generator. The other way is employment of PLL based frequency synthesis. It is suggested that the calibration signal frequency offset should provide covering the interpolation interval with a step of a few picoseconds. A standard approach assumes using one PLL and (so as to guarantee a very low jitter) a Voltage Controlled Crystal Oscillator (VCXO). Typical frequency tuning range of VCXOs is 50..100 ppm. So that some frequency offset of 20...30 ppm could be provided, the PLL prescalers coefficients have to be big enough to satisfy the equation:

$$Fbase/N = Fvcxo/M, \quad (1.7)$$

where Fbase – time base frequency, Fvcxo – calibration VCXO frequency, N and M – frequency division coefficients. 25 ppm offset is provided by the coefficients 4000 and 4001. On the other hand such offset results in 2.5 picoseconds period difference for the typical time base frequency of 100 MHz, which should be enough for covering the interpolation interval (that is the time base signal period). However, having such big numbers of division coefficients is not very good for synthesizing a very low jitter pulse signal – the delays between the charge pump actions are too long.

To improve the quality of the synthesis an additional PLL based on very high frequency VCO (GHz range) could be used. The advantage of such VCO is that the

absolute period jitter at GHz range becomes proportionally smaller with the same typical relative period jitter of non-crystal VCOs.

To improve the quality of the synthesis an additional PLL based on very high frequency VCO (GHz range) could be used. The advantage of such VCO is that the absolute period jitter at GHz range becomes proportionally smaller with the same typical relative period jitter of non-crystal VCOs. Using prime numbers for coefficients N and M allows synthesizing frequencies, which results in desired small steps of covering the interpolation interval.

The described above approach to PLL has been realized by using an off-shelf frequency synthesis and clock distribution chip. The task of the research was to investigate the effectiveness of the suggested calibration method on the basis of an experimental PLL block that is built with the employment of the PLL ICs AD9524. Moreover, such block could combine the time base signal synthesis with that of the calibration signal. The design of the time base and calibration signal synthesizer (TBCSS) has been done according the architecture shown in Figure 1.11. The TBCSS consists of two PLL ICs (PLL IC1 and PLL IC2) and VCXO1. Each PLL IC contains the following (essential for the design description) components: Phase-Frequency Discriminators (PFD1 and PFD2); several frequency dividers; Charge Pump and Filter stages (CPF1 and CPF2); internal 3.5-4 GHz VCO.

The external VCXO is running at 40 MHz. A high stability 10 MHz reference signal is applied to the reference input of the PLL IC1. The reference frequency is multiplied by 4 by means of the first PLL of the PLL IC1 (consisting components PFD1, CPF1, divider by 4, and VCXO1). The resulting frequency (40 MHz) is then multiplied by 100 (4.0 GHz of the internal VCO). The frequency of the VCO is then divided by 4*10=40 so as to provide the timer time base frequency (100 MHz). The former is also divided by 4*67=268 to feed the PLL IC2. And the frequency of the VCO of second PLL IC is divided by 251. The obtained frequency of that VCO is then divided by 11*1023=11253 so as to obtain the final frequency of the calibrating signal.

The PLL ICs AD 9524 are configured by means of an on-board microcontroller (PIC18Fxxx).

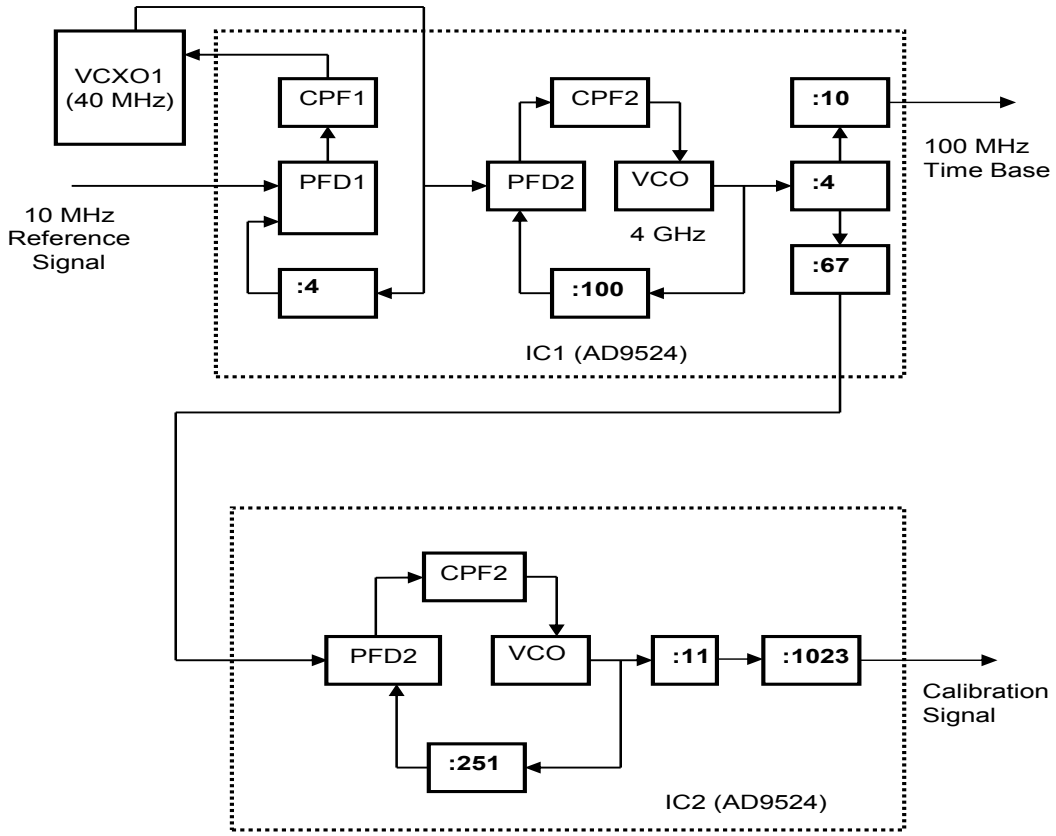

Fig.1.11. Block diagram of time base and calibration signal synthesizer

Using the FLL- and PLL-based generators with „good“ period for calibration allows to get the correction function with very stable and repeatable quality characteristics. The experiments with the measurement error evaluation in the wide temperature range from 5 ^{o}C up to 45 ^{o}C confirm the best and stable precision (Figure 1.12).

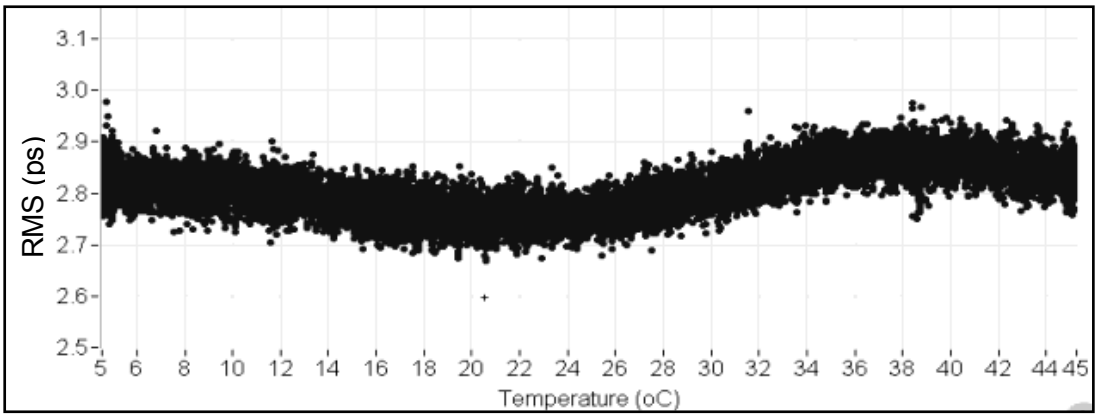

Fig.1.12. The measurement error in the wide temperature range after re-calibrations by means of the PLL-based generator

1.2 Correction function temporal stability problem

The main factor impacting on Riga ET measurement precision is a temperature variation. Due to the environment temperature variation all electronic components of the timer's hardware change their characteristics. As a result, the transfer function, describing the event-to-time conversion, slightly changes, too. At the beginning of the A033-ET development the single-shot RMS resolution degradation by more than 10 percent occurred beyond the range of calibration temperature ±3 ^{o}C (Figure 1.13).

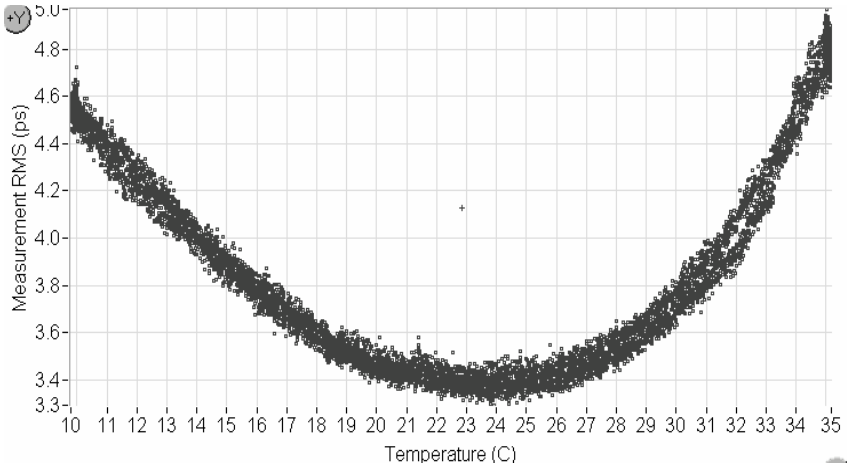

Fig.1.13. Single-shot RMS resolution dependence on temperature.

1.2.1 Oven control of the measurement node

We thought it would be enough if a thermostat were effectively employed. For this reason firstly we have made some experiments with a placement of the measurement node into a self-made small thermostat. Our experiments showed that neither thermostat with heating (Figure 1.14) elements nor thermostat with cooling on the base of Peltier elements (Figure 1.15) could not provide a sufficient precision stability and were not the best solution in terms of the hardware simplicity, compactness and power consuming.

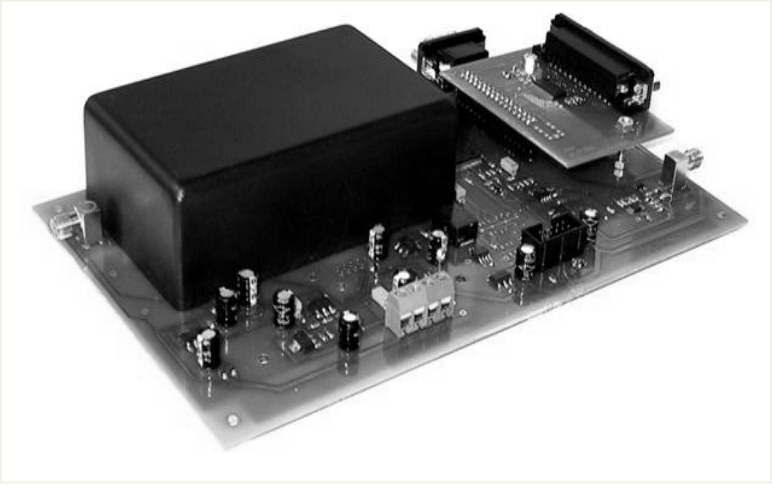

Fig.1.14. Event timer module with the measurement node placing in the thermostat with heating

Fig.1.15. Event timer module with the measurement node placing in the thermostat with cooling on the base of Peltier elements

The both approaches allowed to expand the external temperature range only by 20-40 percent, retaining the measurement precision. In such circumstances it would be better to support the constant temperature in a room, where the event timer is.

1.2.2 Temperature dependence compensation circuits

EET-method is based on digital processing of special analog signals generated in response to input events [1.1]. While the external temperature is stationary the precision remains the same. But if the temperature changes the derived analog signal changes, too (Figure 1.16). An approach allowing to hold, or minimize analog signal change was investigated. A main attention was devoted to thermistors using in signal forming circuit.

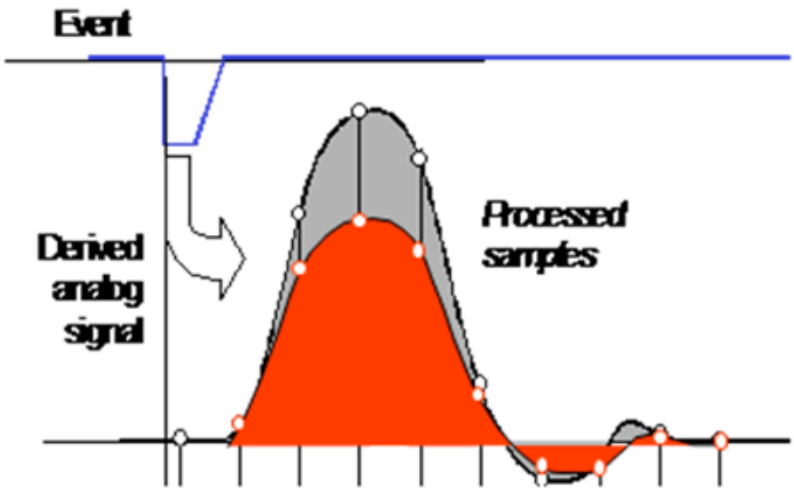

Fig.1.16. A temperature distortion of the event derived analog signal.

For experiments with analog signal monitoring in different temperatures a specific setup, including a chamber with thermostat functions, a specialized source of events, which are constantly shifted relatively to the master clock signal [1.6], and software, allowing to monitor the secondary signal shape and place, was developed (Figure 1.17).

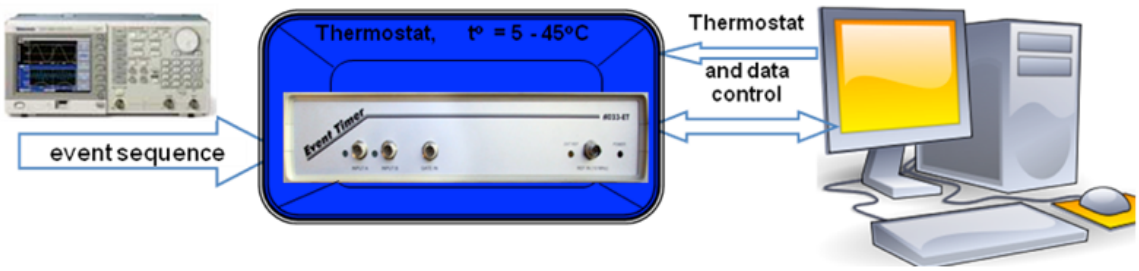

Fig.1.17. Setup for derived signal monitoring in different temperatures

Using this setup we are adjusting the thermistor values in such a way, that the signal degradation in temperature is a minimal. Unlike the temperature stabilization, right temperature compensation, where it is possible, leads to a sufficiently effective solution. Such temperature compensation is applied in the latest versions of the A033-ET. Temperature dependences typical for the A033-ET precision is presented in Figure 1.18.

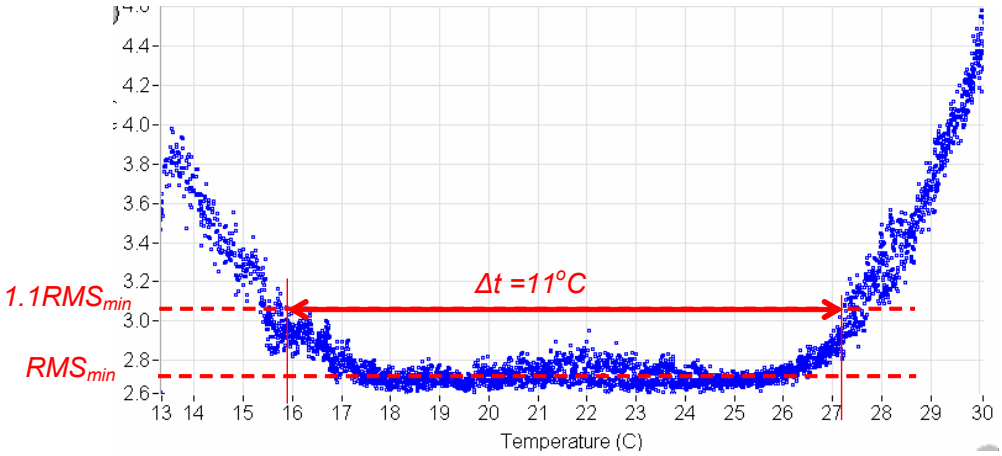

Fig.1.18. Temperature impact on precision degradation with compensation elements

One can see in Figure 1.18 that, as the result of temperature compensation, temperature range is considerably extended around the temperature, when the device calibration has been performed. In this case the single-shot RMS resolution degradation by more than 10 percent occurs beyond the range of 11 ^{o}C.

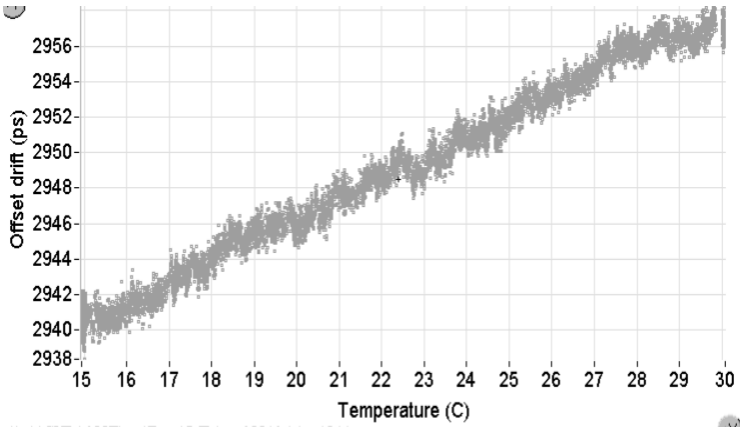

Fig.1.19. Temperature impact on a single-input offset drift

Another important event timer characteristic is a single-input offset drift, which shows the timer time scale drift in temperature. The temperature compensation also decreases this drift and, as can be seen from Figure 1.19, this drift is only a little greater than 1 ps/ ^{o}C.

This characteristic is not essential in case of interval measuring, because the interval origin and end are very close in time and have the same time shift. But in tasks, which are related with the one-way laser ranging and Time Transfer, it has become very important.

1.2.3 The set of correction functions

As an alternative solution to obligatory re-calibration in case of temperature drift, it is possible to create preliminary the calibration tables for different temperature ranges of the event timer operation, and automatically select one of the tables, taking into account the current internal temperature. Evident advantage of this approach is an actual exclusion of the calibration as a complicated online operation, requiring the essential processing and time resources, and intensive data transferring through the interface with PC.

Practicability of this approach has been experimentally proven in an event timer module to be developed. To get the correction tables for supposed temperature range we used a special chamber with possibility to set and keep a temperature in a wide range (our chamber supports the temperature from -5 ^{o}C up to 110 ^{o}C). The correction functions were built for the following temperature values: $q^1 = 20$, $q^2 = 25$, $q^3 = 30$ ^{o}C. It means that at each temperature we wait while the process is stabilized in temperature and then build thoroughly the correction function at a great statistic volume. At the same time an internal temperature of the measurement node is registered.

As result we have three correction functions $F_C^1(D), F_C^2(D), F_C^3(D)$ for three internal temperatures q^1, q^2, q^3. In a real operation process in parallel with the measurement a current internal temperature q is monitored and to convert the digital estimate D_j to time instant $\hat{\tau}_j$ the correction function $F_C(D)$, corresponding to the closest temperature is used in accordance with the expression (1.8).

$$F_C(D) = \begin{cases} F_C^1, if\ q < q^1\ or\ abs(q^1 - q\ ) < abs(q^2 - q)\ else \\ F_C^2, if\ abs(q^3 - q\ ) > abs(q^2 - q)\ else \\ F_C^3. \end{cases} \quad (1.8)$$

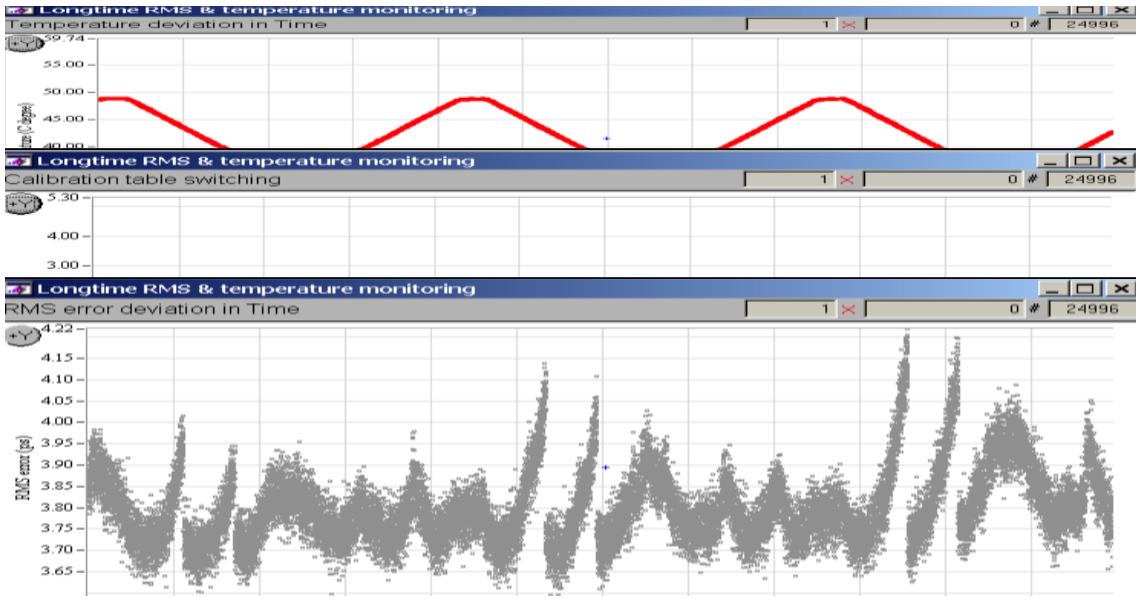

Fig.1.20. The measurement error variation with the calibration switching

As a result in the external temperature range 12.5 – 32.5 ^{o}C the single-shot RMS resolution remains in the range 3.5 – 4.2 ps (Figure 20). The bottom plot shows the measurement error evaluation, which was made under the internal temperature, shown in the upper plot. The internal temperature is changing in accordance with the external one. The middle plot shows a moment of switching from one correction function to another, which corresponds to the current internal temperature.

It seems that, in combination with the right temperature compensation, this approach can provide the stability of the precision characteristics of the event timers.

1.3 Time evaluation of the secondary signal without calibration

And finally the most effective solution could be secondary signal time position estimation method that is not critical to signal form temperature changes or doesn't need a special calibrating procedure executing for every external temperature change. This method theory is expounded in detail in [1.7], but here the main results will be presented.

The method is based on the theoretical and experimental research of interpolative measurement that does not require extra correction of the evaluations of the analog signal time position and therefore makes it unnecessary to preliminarily identify the transfer function of the interpolator. The studied technique evaluates the characteristics of the regression model of an analog signal according to a sequence of samples. The processing is confined to matching the regression function describing the *waveform* of an analog signal with signal samples. The regression function coefficients chosen as informative parameters of the modeled signal must depend on the level of the signal shift relative to a certain initial moment of time. The signal referred to is a *wave train* generated by a triggered relaxation oscillator, when each event occurs (Figure 1.21).

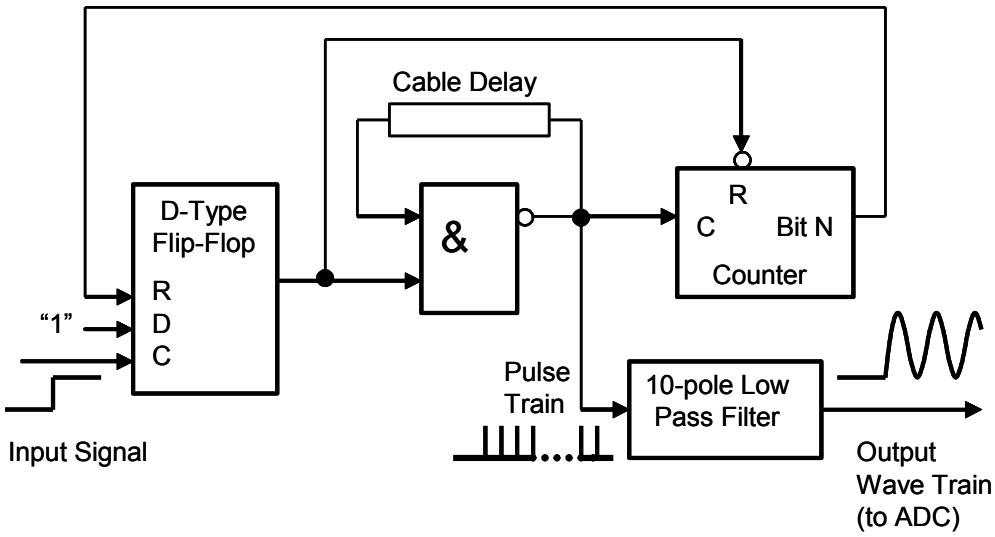

Fig. 1.21. Converter of input events into the output oscillation wave train of the triggered relaxation oscillator.

The triggered relaxation oscillator consists of a *D-Type Flip-Flop* logical element "I" (*gate &*) with a *cable delay* in the delayed feedback chain, an impulse *counter*, and a *10_pole low pass filter*. The converter functions as follows. The D-trigger switches on to the state of the logical unit along the input signal front, i.e., the event occurrence mark, and the logical element "I" and the impulse counter are therefore unblocked. The "I" element and the cable delay line constitute a triggered relaxation oscillator that starts to produce rectangular impulses with a period equal to a doubled sum of the cable and logical element delays. After the set number of countings is reached, the counter registering the impulses generates a logical unit according to its output charge Bit N. The D-trigger and the counter are reset, and impulses cease. The series of impulses generated at the outlet of the relaxation oscillator goes through a low pass *Chebyshev Filter* with a cut-off frequency exceeding the impulse recurrence in the series. A fairly even oscillation wave train is therefore generated at the outlet of the filter and fed to the inlet of a 12-digit analog-to-digital converter (ADC).

The accuracy of the studied interpolation technique was illustrated with experimental results of determining event occurrence instants. To generate an event flow, a highly consistent impulse generator was used. The sequence of impulses generated was linked to the flow of periodic events. The interval between the events was about 204.794968 μs, while the total number of events was 160. When an event occurred, a wave train of 25 oscillations with the filling frequency = 27.9 MHz was generated by the converter of the incoming events into wave trains (see Figure 1.21). To digitize the instant values of the wave train, a 12-bit AD converter with a discretization frequency of 100 MHz was used. The number of wave train samples used in the processing was 35. However, the samples taken at the initial, i.e., the unsettled, stage of the wave train were not considered, were discarded, and were not used for the processing. The time position of the wave train was evaluated.

As an example, the fluctuations of the evaluations of the event flow time values relative to the linear trend (event occurrence time jitters) are shown in Figure 1.22. The evaluation of the linear trend of the determined temporal values of the event flow was displayed in the form of a straight line of regression, the characteristics of which were determined using the least-squares method. The lower curve in Figure 1.22 shows the

sequences of errors in measuring the intervals between the events from the flow. Calculated using the sequence of intervals, the mean square error of the measurement was 2.885 ps.

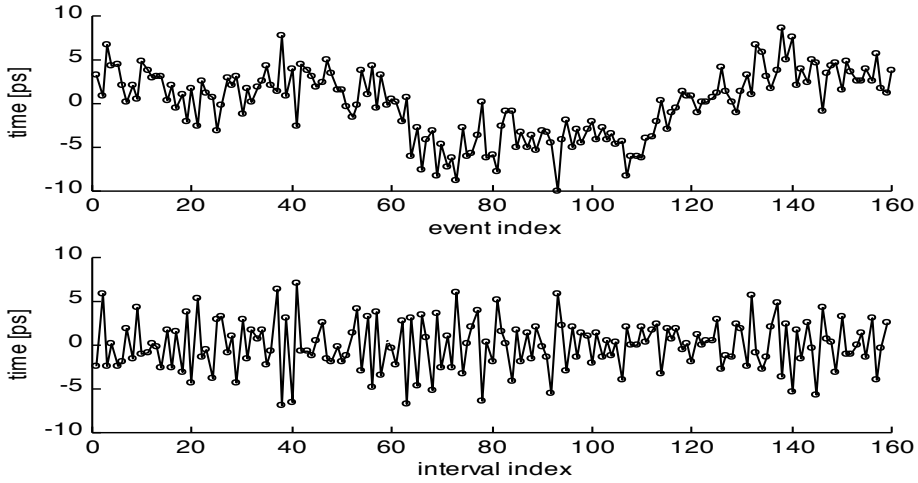

Fig.1.22. Jitter of the event occurrence instants (upper curve) and the sequence of errors in measuring the time intervals between the events (lower curve).

Comparing the experimental outcome with the results of the specially executed computer modeling, the following conclusion can be reached: the mean square error obtained in the experiment during the measurement of the time intervals by the event timing was 2.885 ps. Nevertheless, this value does not allow one to make an ultimate judgment about the accuracy of the interpolation. The given value is overestimated since it contains not only errors in the interpolation measurement but also inconsistencies stipulated by the unsteady frequency of the generator producing event streams similar to Palm flows. The outcome of the modeling allows one to assert that, if real measurements of time intervals between events are made, the type of interpolation in question (using a 12-bit AD converter) will ensure that the mean square error in the separate measurements does not exceed 2.5 picoseconds.

The processing of the samples is realized using the regression model of an oscillation wave train with linear information-bearing characteristics. The model is a finite sequence of harmonic components with frequencies divisible by the basic oscillation frequency. The time shift of an event occurrence from the beginning of the corresponding discreteness interval is determined using the evaluated amplitudes of the quaternary harmonic components. It is shown that the use of linear algorithms of evaluating the characteristics of the regression model of the oscillation wave train allows one to ensure the pico-second accuracy of the interpolation measurements. It is shown that the considered type of interpolation does not require extra correlation of the obtained evaluations of the oscillation wave train time position. The latter evaluations can therefore be used directly as interpolation evaluations of event occurrence instants, which allows one to avoid the provisional identification of the interpolator's transfer function.

1.4 Digital Functions integration in one chip

Considering the performance of modern super-high integration chips that have more and more integrated functions and provide higher operation speeds, it is possible to make the event timer design more compact, operating at higher frequencies, and having a faster interface with user tasks in PC.

One of the most resource expensive tasks in the event timer is the correction function constructing task usually named as calibration. Currently in A033-ET the calibration includes the following operations:

- Start event registration from the calibration generator;
- Calibration program reads ADC samples of the secondary signal and tied rough clock counter values;
- Program checks data on "goodness" of the current generator frequency; if the data don't pass the test, these data are discarded, program slightly adjusts the period of the generator and continues the data accumulation;
- When the predefined volume of data is accumulated (in case of A033 it is 160000 events or 1.28 megabytes) program constructs the correction function $F_C(D)$ in accordance with (1.1).
- The device is ready for measurements.

In the A033-ET device the functions, associated with the control of measurement process in accordance with commands from PC, and the timing data recording into a buffer memory chip, are implemented in CYCLONE-II from Altera Corp. Now there are more complicated FPGAs containing a few millions of logic gates and tens millions bits of memory. This will allow implementing in FPGA all digital functions of the event timer, including the calibration. And only the interpolator node, which executes an analog-to-digital conversion of the secondary signal and requires a sophisticated adjusting, isn't now realizable in FPGA (Figure 1.23).

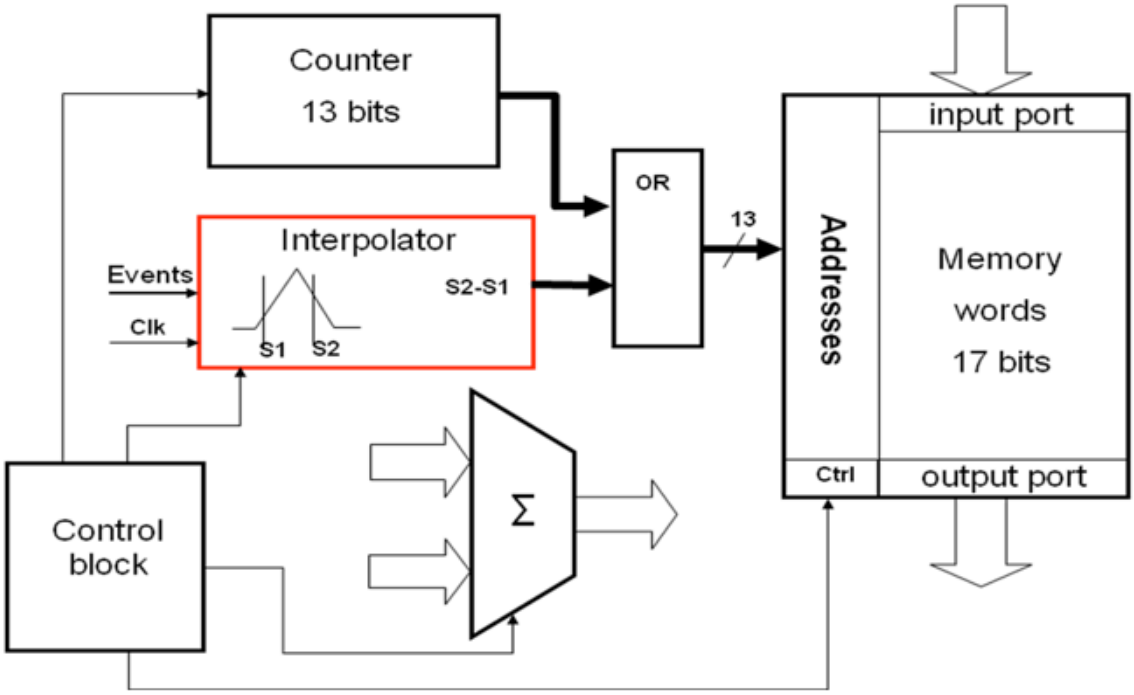

Fig.1.23. Schematic block diagram for the calibration process

In Figure 1.23 the blocks, which are directly used for the calibration, are shown. Calibration control functions and all other functions, related with a control and command processing from the PC are combined into Control block.

In accordance with the above stated calibration procedure after the calibration generator starts the events are coming into Interpolator (Figure 1.24).

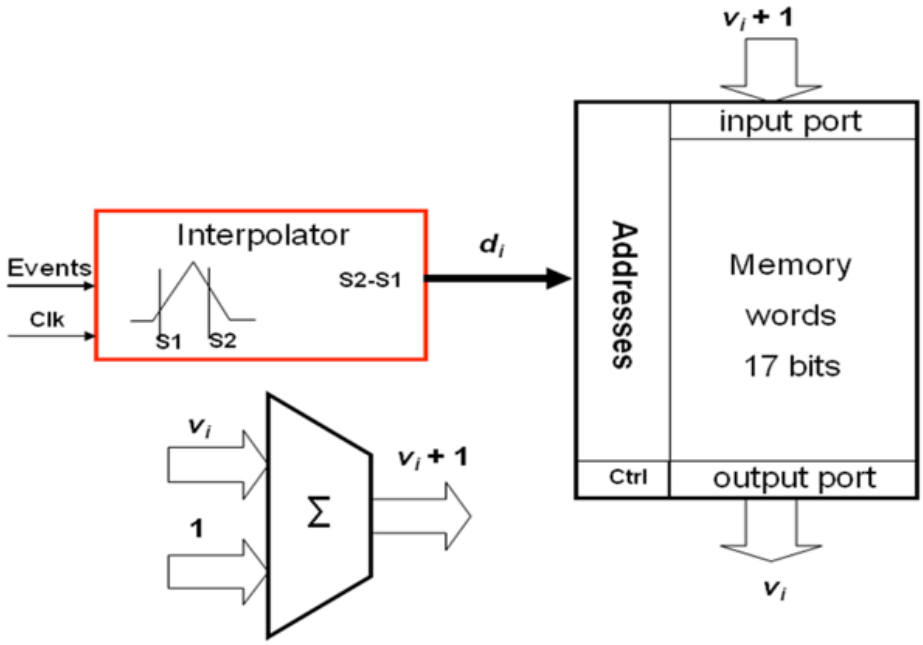

Fig.1.24. Working diagram in statistic collection mode

At the first stage Memory with Adder are working as an accumulator, which counts how much the digital output d_i from Interpolator was appearing. Number of bits in Memory address should be the same as a bit number of the Interpolator output. In accordance with (1.5) after the k events, coming into interpolator, Memory contains quantities of each appearing d_i. It is the event distribution within the master clock period.

To find the correction function $F_C(D)$ in accordance with (1.1) all this quantities are integrated beginning from zero address up to maximal. The addresses are formed by the Counter (Figure 1.25).

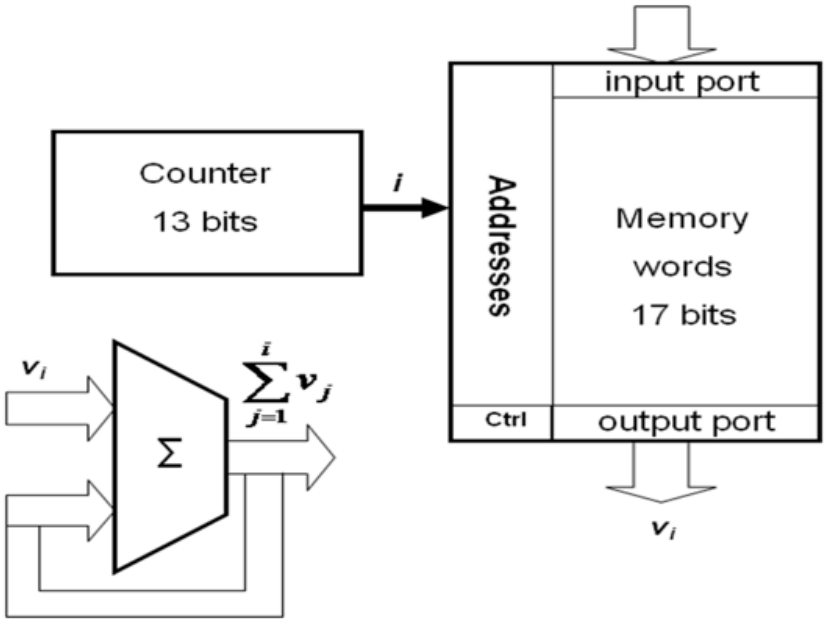

Fig.1.25. Working diagram in correction function constructing mode

The correction function values, stored in Memory in result of executed procedures are not normalized. The multiplication coefficient can be accounted in PC when the time-tags for measured events are calculated, but it is more efficient, if the user task gets the time-tag directly in seconds.

This can be done if the volume of the statistic is accordingly chosen. For example, if we choose k = 10,000,000 we will get interpolation time values directly in femtoseconds (!). But this is too much for existing memory volumes in manufactured FPGA. To match our hopes with manufacturer possibilities we have chosen k = 100,000, and in result we have the interpolation time with the resolution 0.1 ps (Figure 1.26).

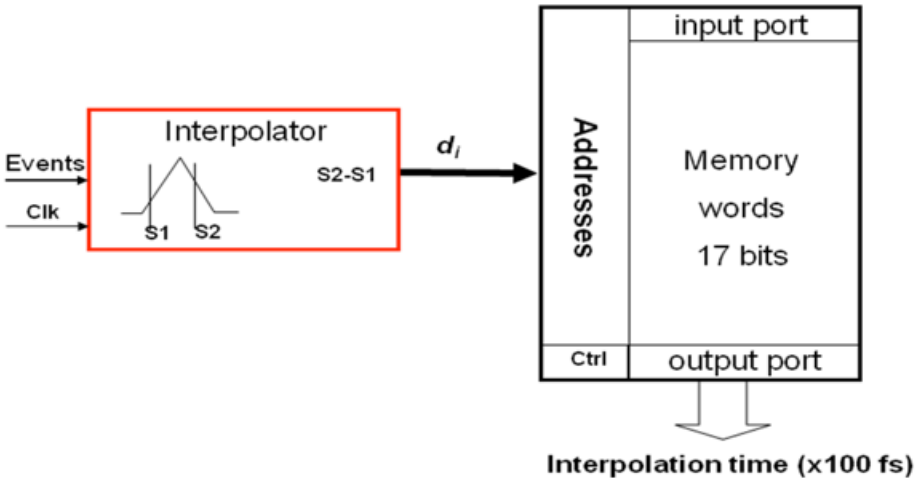

Fig.1.26. Working diagram in the measurement mode

In the measurement mode the Interpolator output value defines an address of Memory word with the corresponding interpolation time. Taking into account that a rough time is counted in 10 ns intervals a full time-tag for each event will be directly in seconds and doesn't require additional calculations from a user application-specific task.

The next subject to integrate into FPGA is the procedures related to user interface. The A033-ET operation is fully controlled by the ET-client via TCP/IP network or directly by a user program, which is built on the base of the sample program delivered with the A033-ET. To prepare the A033-ET for measurements the user executes the following procedures (Figure 1.27):

- calibration procedure to get an interpolation table;
- time synchronization with external GPS to get an offset of time scale; and
- arming command sequence for certain measurement mode.

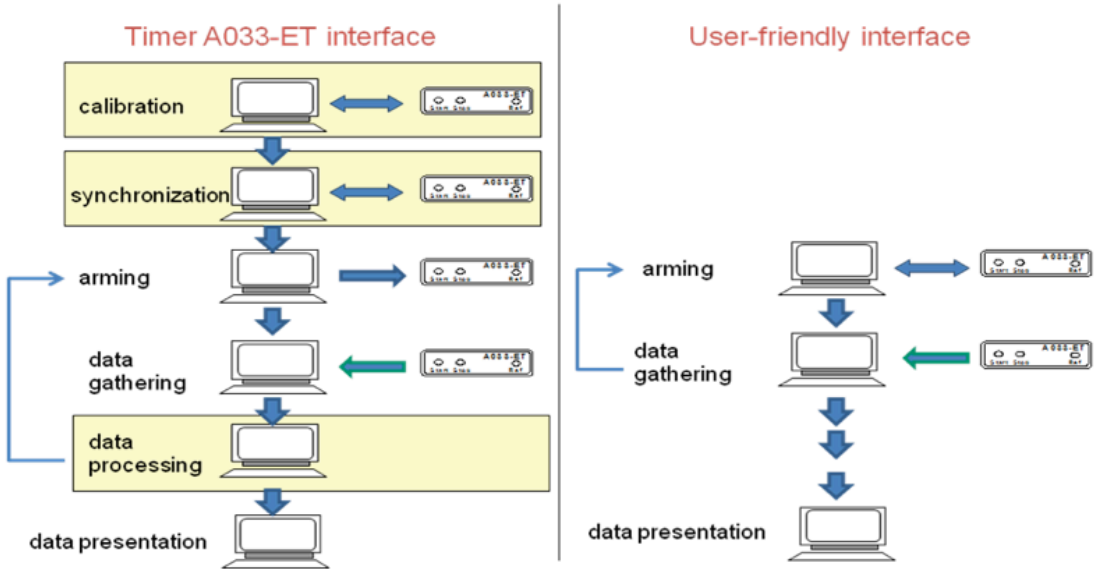

Fig.1.27. The user interface of the A033-ET (on the left) and its optimization (on the right)

After that the events coming at the inputs of the device are logged in the internal buffer memory and this timing information can be read into PC. To get the epoch time-tag in seconds for logged events the user reads from the device 8 bytes containing the number of hardware internal clock counts and ADC samples for each event, and converts these bytes to epoch in seconds, using the interpolation table and offset. If the event timer gating mechanism is used it is necessary, on a base of the time of the Start event marked by a special flag, to calculate the time until Stop event and write this time back to the device.

To make the user interface with the Riga event timer friendlier, it is necessary to minimize a volume of processed data and the number of executed commands. We plan to transpose some procedures, currently executed in PC, into hardware device, leaving to user only the main functions: start measurement in desired mode, and get directly the epoch time-tags expressed in seconds for all registered events.

Higher FPGA performance allows increasing the device master clock frequency. Higher clock will allow getting the better RMS resolution and shorter “dead time”, which are considered as the main performance characteristics of the event timers. But with higher clock the problem of logic competitions in ADC and FPGA can appear, so the alternative choice between speed and safety should be done.

FPGA big resources and existing libraries of ready-to-use blocks in VHDL for different types of interfaces allow realizing more effective connection with the user task in PC. The most popular for measurement devices connections are: new USB3, providing data transfer at 400 Mbyte/s; PCI Express, having exchange speed from 250 Mbyte/s up to 1Gbyte/s; and Gigabit Ethernet – from 12 Mbyte/s up to 3Gbyte/s. Application of such high-speed interfaces will allow considerable increasing the average rate of continuous event timing and extending the control functionality from the user tasks.

1.5 Event timing module implementation and approbation

To realize not all, but at least some of the above presented improvements the new Event Timing module (ET-module) has been developed (Figure 1.28).

Fig.1.28. Event Timing module

In the ET-module for compactness a different method for secondary analog signal forming is implemented. The same DSP using as in the A033-ET didn't provide the same precision. We find a problem in an essential correlation of ADC samples was used. To provide a functional for more effective multiple samples utilization special experiments were done. In a result of these experiments we define weighting coefficients for all samples. In the measurement error dependence on temperature plot (Figure 1.29) it can be seen the effect of weighting coefficients (red points) in comparing with a previous method (blue points). The single-shot RMS error is decreased by more than 1 ps in a case of temperature variation.

The ET-module presents the main event timers performance characteristics achievable with application of the innovative DSP-based technology (precision, resolution, measurement rate, etc) as well as physical hardware characteristics (complexity, size, power consuming, etc). The performance characteristics following below refer just to the ET-module features, they are related to the main features of the technology, but not cover them. There are many technical details in ET-module implementation that can be modified depending on specific needs of potential users and further technology progress.

Single-shot RMS resolution is the main parameter specifying the practicable ET-module precision. It is defined as the standard deviation of total error in measurement of time intervals between events. To estimate the standard deviation a high stable pulse generator with own RMS~1ps is used. Measurement of intervals between these pulses showed that the ET-module supports single-shot RMS resolution better than 4 ps (Figure 1.30).

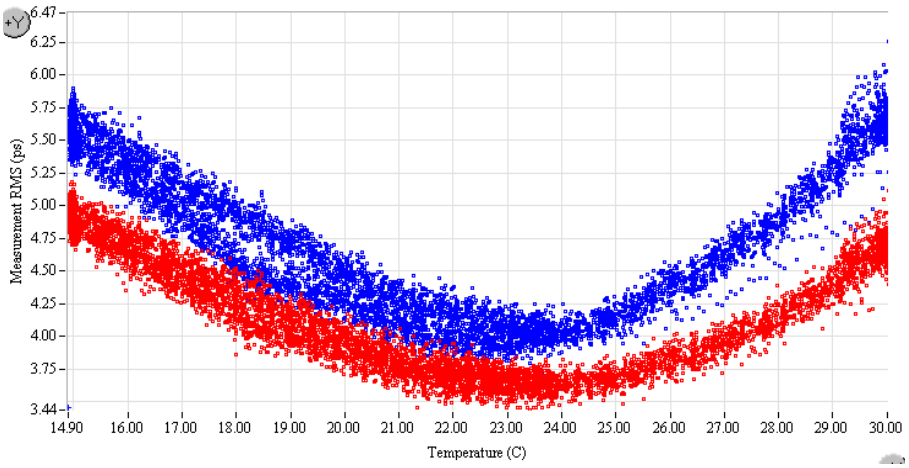

Fig.1.29. Effect of coefficient weighing on the measurement error

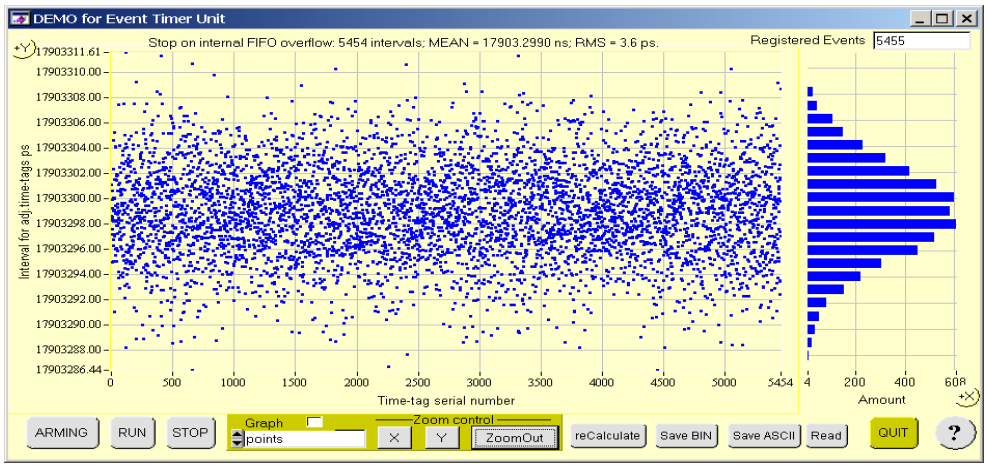

Fig.1.30. Measurement results: intervals deviation and histogram.

Integral non-linearity error is a systematic error in event measurement that depends on the position of measured event over interpolation interval. In the average this error is specified by the value of its standard deviation over interpolation interval. The ET-module integral non-linearity RMS error is ranged from 1 to 1.5 ps (Figure 1.31).

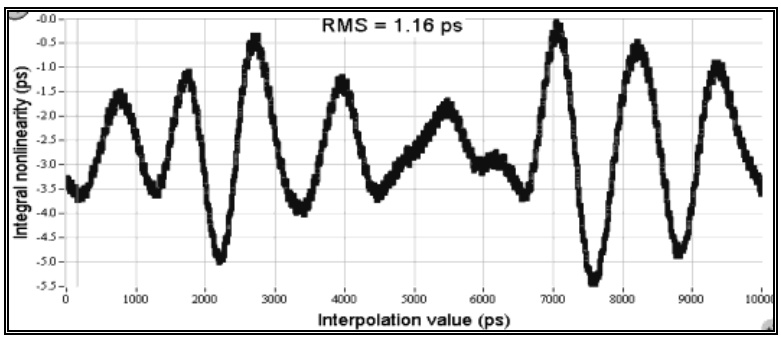

Fig.1.31. Integral non-linearity error over 10 ns interpolation interval

Interval non-linearity error is a systematic error in measurement of time interval between adjacent events that depends on the value of this interval. The ET-module interval nonlinearity error does not exceeds ±0.5 ps for time intervals greater than 100 ns. For smaller time intervals such errors can be a little greater (especially for time intervals that are near to the 50 ns dead time (Figure 1.32)).

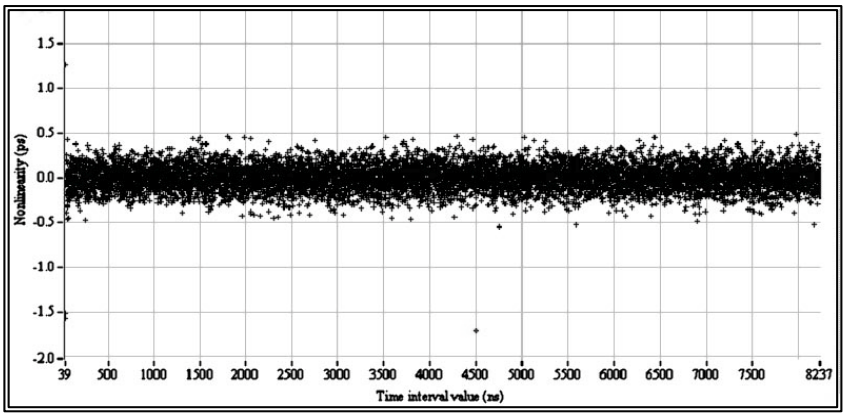

Fig.1.32. Interval non-linearity error versus time interval

Single-input offset drift is seen as **a** long-term deviation of systematic error in measurement of events. Such drift reflects long-term instability of the internal time-base relative to the external 10 MHz reference frequency, depending mainly on the ambient temperature variation. The ET-module single input offset drift is about 1 ps/^{o}C (Figure 1.33).

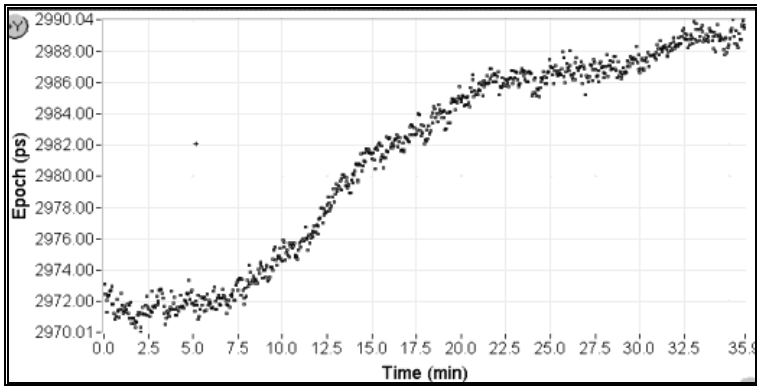

Fig.1.33. Single-input offset drift variation in temperature range from 15 up to 30 ^{o}C.

Maximum burst rate means maximum rate of continuous measurement for limited sequence of sequential events. The ET-module supports the maximum burst rate 20 MSPS for 1K events in conformity with its dead time (50 ns) and size of buffer memory.

Maximum average rate means maximum rate of continuous (gapless) measurement for unlimited sequence of sequential events. The ET-module supports the maximum average rate 1 MSPS in the mode of data acquisition (without displaying any data during acquisition process). When the data are displayed partly or fully, the maximum average rate is decreased down to 75 KSPS and 512 SPS respectively.

The ET-module is tailored to operating conditions when ambient temperature is in the range from 15 to 30 ^{0}C. In this range the ET-module supports the specified precision without any calibrations due to special means for compensating of hardware temperature instability. If the ambient temperature is outside the mentioned range, the specified precision is not guaranteed.

The ET-module hardware consists of special time-to-digital converter, FPGA-based logic circuit, clock synthesizer and circuit providing USB 2.0 interfacing of the hardware with PC. The hardware is realized as a single board (Figure 1.28) having size 160x175x20mm, need power supply about 6 W and has weight 0.3 Kg. The board can be housed in a standard plastic box with dimensions - 180x55x215 mm, but in this case a fan is required. Power supply should have three voltage: +7.5V (0.8A), +12V (0.2A) and –12V (0.05A).

1.6 Short-distance transmission of event timing information

Both analog and digital information representations are used for event fixing in time and either analog or digital carriers can be used for transmission of this information. While the end-result of event timing typically has to be given as a picosecond-resolution digital quantity, transmission of this information can be performed in two different ways, analog or digital. Both analog and digital information transmission options have their advantages and drawbacks. In general, they are well known, however the conditions for transmitting event timing information are specific. They are investigated theoretically and experimentally for two typical types of applications, namely, for:

(1) gathering and transmission of data from a cluster of remote samplers to the master part of the respective distributed ADC (Figure 1.34);

(2) high-speed short-distance transmission of digital data.

These two cases are considered as generalized models of two types of specific event timing information transmission subsystems. Each of them covers a number of various specific applications.

In the first case the event timing information is given in an analog form and short pulses are used as analog carriers for transmission of this information, as shown in Figure 1.34. In the considered case they, specifically, carry the input signal and reference function crossing event timing information form a multitude of front-end devices to the distributed ADC reconstructing and displaying the received information. Outputs of all front-end devices are connected through a single OR logic element to the transmission line.

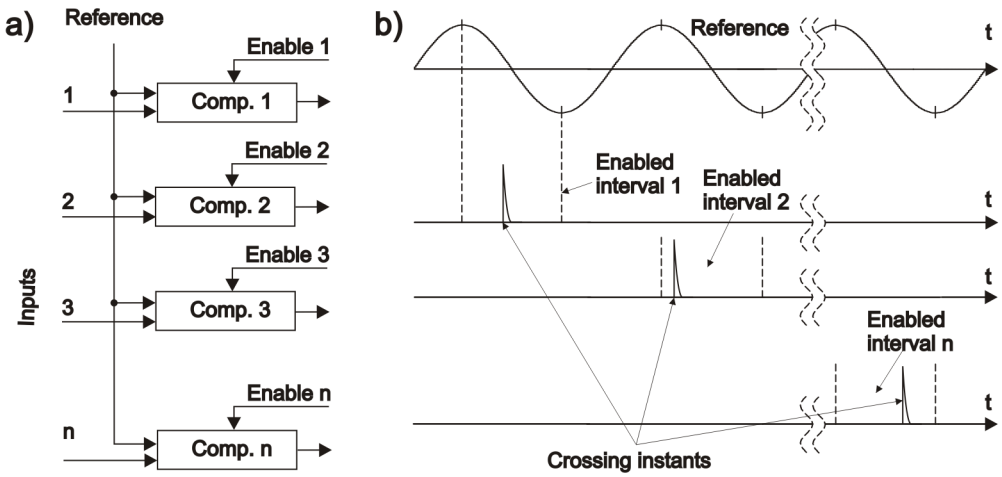

Fig.1.34. Typical conditions for gathering and transmission of timed event data from a cluster of remote samplers.

Using this type of analog information carrier effectively provides for data compression and for increasing the operational speed of the system in this way. Indeed, the transmitted data are compressed because transmission of a single pulse in this case is equivalent to transmission of a multi-bit word. This approach to transmission of the event timing information has been used and it works. As it leads to data compression in a simple way, it is of high practical interest to extend the application area of this method. However to widen its application range, a number of essential problems have to be investigated, in particular, the following:

- Analog event representation of the respective digital inputs with subsequent digital representations of the respective analog data.
- Taking into account that the time intervals between timed events are non-uniform and not necessarily random.
- Specifics of the considered timed event signals having features unparalleled by other types of digital signals.

Both computer simulation and experimental studies have been carried out to make these investigations. The basic features of this type of data compression, in particular, for high-speed short-distance transmission of digital data needed for many various applications have been experimentally investigated on the basis of a system having the basic configuration shown in Figure 1.35.

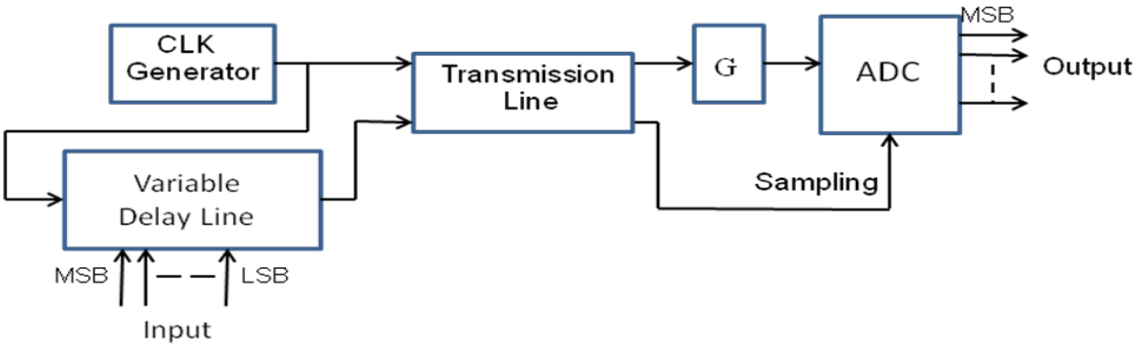

Fig.1.35. Structure of the experimental device.

The further described experimental set-up was built in accordance with this principal structure. As can be seen it consists of two parts connected by a transmission line. The first part serves for input signal encoding and the second part performs recovery of the encoded signal received over the transmission line. Both parts are synchronized by a common clock sequence. A variable picoseconds-resolution delay is used for delaying the clock pulses proportionally to the respective input signal values. These variably delayed pulses are used for initiating sampling of a reference signal put to the input of ADC. While various reference functions could be used, preference is given to sine-waves as it is easy to generate them and to stabilize their parameters, they have extremely simple and well-defined spectra and they are convenient also for reconstruction of the sampled signals. As this structure is used for multi-purpose experimental investigations, the reference signal at the output of the generator G in this case is such sine function.

According to the considered functional structure, the digital carrier of event timing information is formed by the ADC at the stage of transmitted data reconstruction. While this type of signal digital representation is specific and successful using of it requires some skills, it leads to obtaining significant benefits. Specifically:

- Achieving time and energy saving at data transmission (each single symbol carries multi-bit information).
- Compatibility with the Ultra-wideband wireless data transmission technology.
- Complexity-reduction of algorithms for data pre-processing.

Whenever this device is used for multi-channel data acquisition according to the principles illustrated by diagrams given in Figure 1.34, only those signal-reference crossings are taken into account that happen during the time intervals when the respective comparator is enabled by a specially generated enabling function. This enabling function is also used for executing the input multiplexing. The analog input signal switching are voided in this way and that certainly represents a significant advantage.

Diagram of the developed and made experimental set-up is given in Figure 1.36. It is computerize, input and output data sequences are monitored and analyzed.

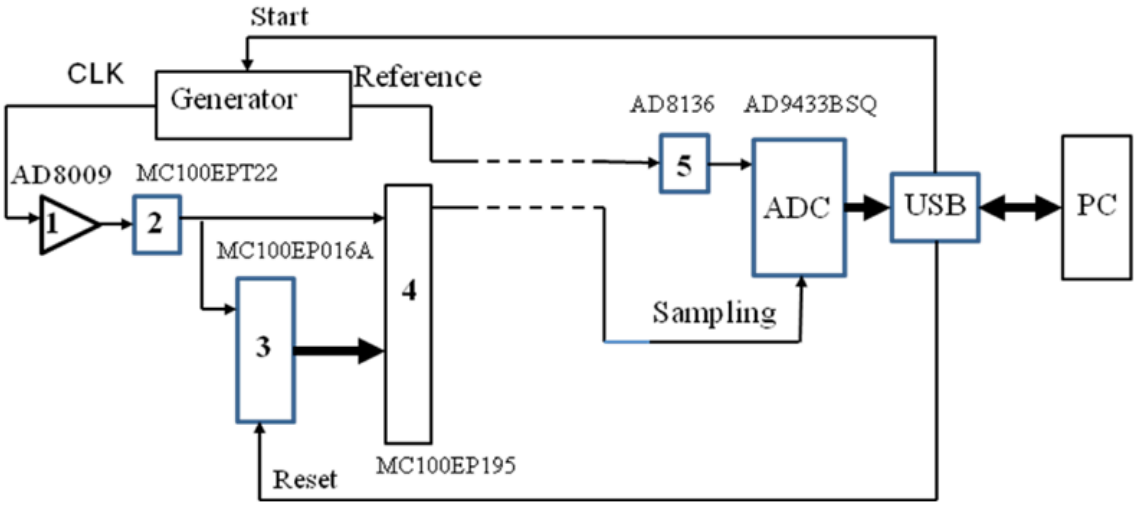

Fig.1.36. Experimental set-up: 1 – clock signal former; 2 – TTL/PECL translator; 3 – binary counter; 4 – variable delay line; 5 – reference signal former.

The basic experiments are carried out to estimate the upper limits for the transmitted data bit rate and transmission speed under different conditions, including varying external noise and length of the transmission distance.

1.7 Conclusions

Earlier well-proven technology for event timing based on EET-method is considerably advanced both in theoretical and practical aspects. Especially that concerns the techniques of event timer calibration which allow significantly improving the precision of the event timer, precision stability in variating environment temperature, repeatability and rubustness of calibration results.

In the framework of general concept of DSP-based event timing theoretical basis of a new promising method is offered and investigated by computer simulation and experimental research.

Taking into account an escalating integration and performance of modern chips there are developed new methods to transfer an essential part of timing-related functions into hardware, optimizing the application-specific task and user interface, increasing the speed and reliability of operation.

Some results such as stable single-shot RMS resolution, weakened dependence on temperature, robust calibration that is independent on temperature variation, and modular design with USB2 interface are already implemented in the Event Timing module realization.

The approach to short-distance transmission of event timing information was developed and experimentally estimated under different conditions.

All other results and further technology improvement are planned for realization in the near future creating the high-performance event timing system for different specific measurement applications (satellite laser location, fluorescence describing time measurement spectroscopy, *time-of-flight* mass spectroscopy, etc.).

References

[1.1] Yu. Artyukh, “A method for continuous superprecise time-interval measurement”. Automatic Control and Computer Sciences, Vol. 35, No.5, pp. 11-18, 2001.

[1.2] Yu. Artyukh, V. Bespal’ko, E. Boole, “Potential of the DSP-based method for fast precise event timing”. Electronics and Electrical Engineering, Kaunas: Technologija, No. 4(92), pp. 19–22, 2009.

[1.3] Yu. Artyukh, V. Bespal’ko, E. Boole, “Non-linearity errors of high-precision event timing”. Automatic Control and Computer Sciences, Vol. 42, No. 4, pp. 191-196, 2008.

[1.4] LR Patents Nr. 14358 „*Interpolācijas „laiks-kods” pārveidotāja kalibrēšanas metode*”. Izgudrotāji: V.Bespaļko, J.Artjuhs, J.Buls, A.Mezeriņš. Īpašnieks: Elektronikas un datorzinātņu institūts, publicēts 07.03.2011.

[1.5] Yu.Artyukh, E.Boole. Jitter Measurement on the Basis of High-precision event timer, Metrology and Measurement Systems, 2011, No.3, pp.453-460

[1.6] Eksperimentālais makets Nr.01/2011-IMIS/2. Sinhronizēto testa signālu formētājs. Izpildītāji: V. Bespaļko, A. Veršinins.

[1.7] A.Rybakov, V.Vedin. Precise Measurement of event Flow Time Coordinates Based on the Digital Processing of a Triggered Relaxation Oscillator Wave Train, Automatic Control and Computer Sciences, 2011, Vol. 45, No. 3, pp. 162–173.

2 Ultraplatjoslas impulsu ģenerēšanas moduļa izveide (t.sk. tā salāgošana ar UWB antenām) un ar platjoslas stroboskopisko pārveidotāju iegūto signālu analīze (t.sk. izmantojot vairākas uztverošās iekārtas)

2.1 TWV radar signal processing

TWV radar signal processing was modeled using one transmitting antenna and two receiving antennas. Digital sampling converter was used as receivers; signals are registered with „up-and-down" method and additional signal processing.

Let us assume that distance between two receiving antennas is d_0 and distance to target is d_1 and d_2 accordingly. Then we can easily calculate target coordinates against receiving antennas using equation (2.1).

$$d_1^2 = d_2^2 + d_0^2 - 2d_2 d_0 \cos(D_1), \qquad (2.1)$$

where D_1 – angle against edge d_1.

Distances d_1 and d_2 we can estimate using TOA.

We assume that transmitting pulse can be described as

$$u_1(t) = A_1 e^{-\alpha t} \sin\left(\frac{2\pi}{T} t\right) + u_n(t), \qquad (2.2)$$

Where A_1 – signal amplitude, T – sine period, $u_n(t)$ additive Gaussian noise with standard deviation $\sigma_1 = 1$.

It is assumed that sampling receiver has its own phase jitter.

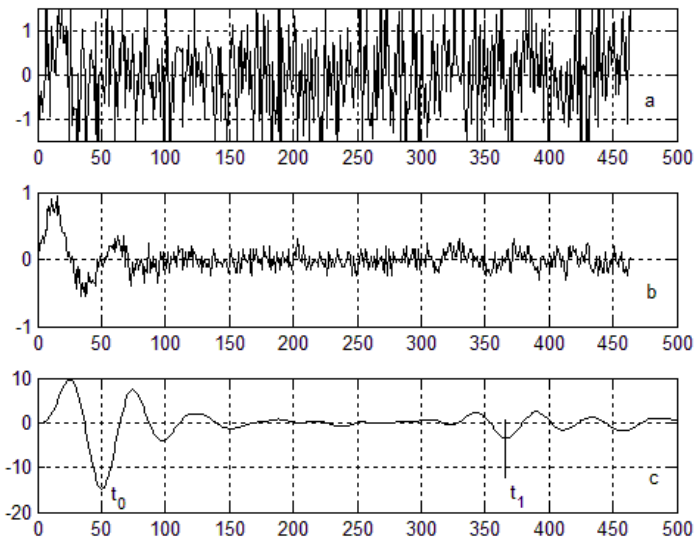

Fig. 2.1 a – received signal; b – signal processed with „up-and-down method";
c – signal after convolution.

Signals (2.2) were converted with „up-and-down" method and following convolution operation, where as a template signal sine monoimpulse with period T was used. One

antennas received signal is shown in **Fig. 2.1**. Time delays t_0, t_1 were estimated and d_1, d_2, D_1 were calculated.

Attenuation as function of distance and antenna directivity was taken into account.

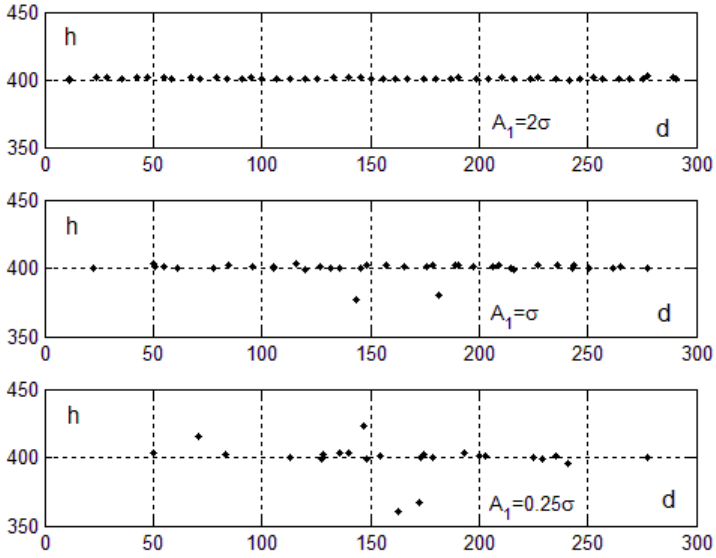

Fig. 2.2 Target trajectory estimation with different A_1

Distance between receiving antennas is 3m. Target is moving evenly parallel antennas plane in 4m distance. Target coordinates were calculated in 50 time moments, marked as dots in **Fig. 2.2**. Modeling is done using 3 different received signal amplitudes:$A_1 = 2\sigma_1; A_1 = \sigma_1; A_1 = 0.25\sigma_1$. 50 sampling operations were done, to estimate one sample`s value using $0.015\sigma_1$ equivalent resolution. Results are shown in **Fig. 2.2**.

In **Fig. 2.2** can see that with $A_1 = 2\sigma_1$ calculated target trajectory matches the given trajectory. Calculated distance error $\varepsilon \leq 1\%$. Certain unevenness in sampled coordinates can be observed. With $A_1 = \sigma_1$ separate samples significantly differs from given trajectory or even were not calculated, motion unevenness is getting more significant. But in general the result is acceptable. With $A_1 = 0.25\sigma_1$ calculation error is too significant.

Similar results are shown in **Fig. 2.3** with $A_1 = 0.5\sigma_1; A_1 = \sigma_1; A_1 = 2\sigma_1$ (accordingly a, b, c). Target is moving at twice as large distance as previously in **Fig. 2.2**. Target coordinates were calculated in 65 time moments, marked as dots in **Fig. 2.3**. Given trajectory is shown with continuous line. In this case acceptable results can be achieved only with $A_1 = 2\sigma_1$.

In both cases it is assumed that scattered impulse registering time for each target coordinate is small enough so target motion can not be taken in account. That means that sampling frequency should be higher than 1Mhz.

Modeling experiments allows estimating necessary received signal amplitude with different receiving antenna and target distance. It gives us information about necessary transmitted signal amplitude and results can be used for TWV radar designing.

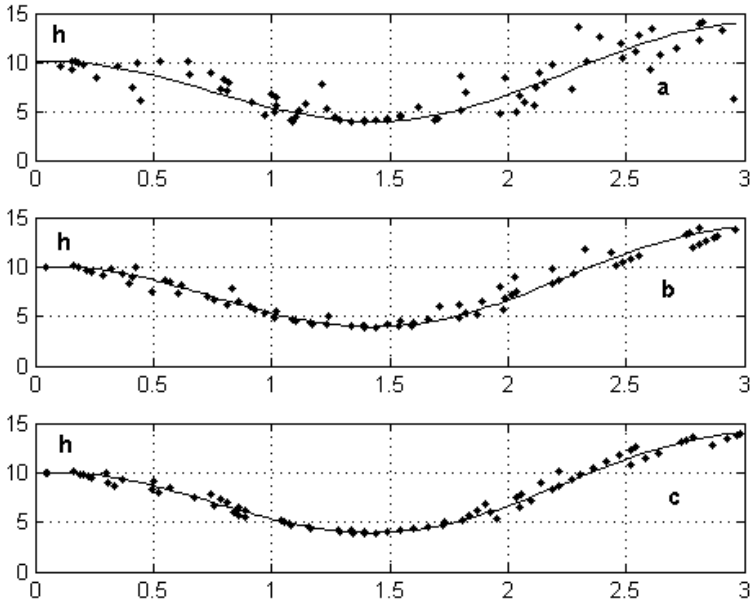

Fig. 2.3 Target`s trajectory with different A_1

2.2 Signal matched filtering for TOA estimation for UWB radars

Signal matched filtering for UWB radar signal processing was studied. Measurements were done with 6 Ghz real time oscilloscope.

Receiving and transmitting antenna was placed next to each other facing the target. Target was metal box with 0.5m^2 front surface area. In **Fig. 2.4** direct impulse and scattered impulse can be seen.

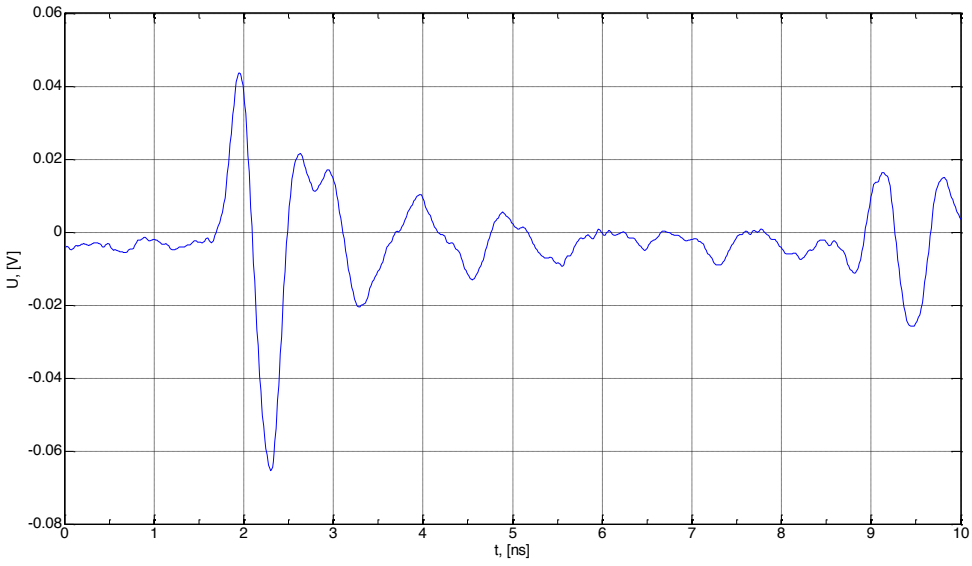

Fig. 2.4 Received signal

As template in signal matched filtering we have to use signal as similar to transmitted signal as we can. In this case the template signal is approximation of 1.5T of direct signal, where T is one sine impulse period (**Fig. 2.5)**.

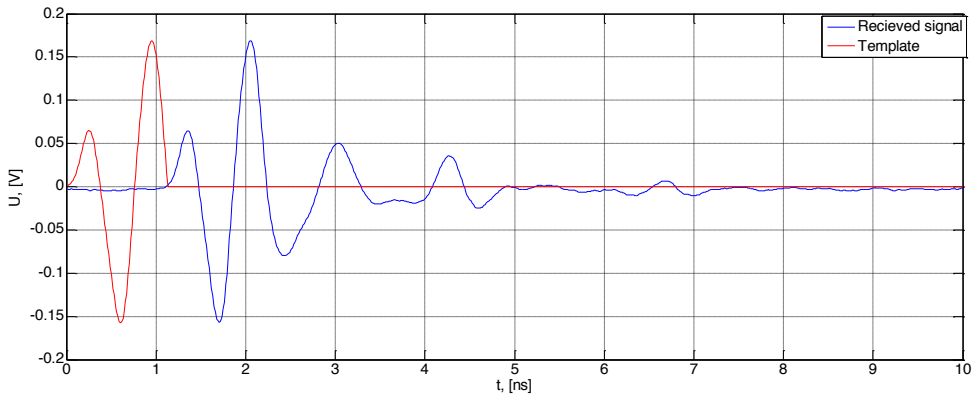

Fig. 2.5 Template signal

In signal matched filtering it is necessary to work exactly with transmitted impulse. In this case a certain part of transmitted pulse is used, because it is hard to tell where the transmitted impulse ends and another scattered impulse starts. It is more precise to call it two signals cross correlation function.

Received and template signal correlation function`s maximums points out the template signal position (**Fig. 2.6**).

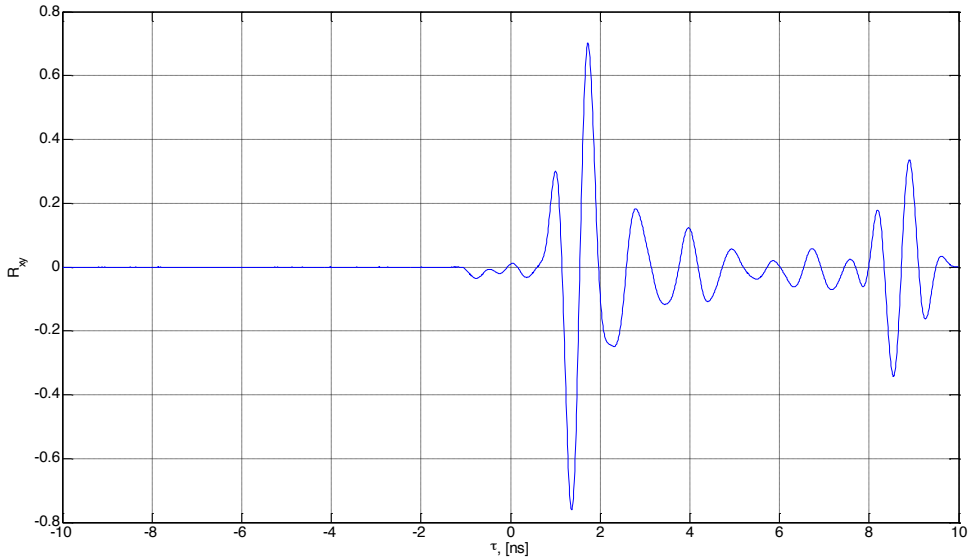

Fig. 2.6 Correlation function

Scattered signal`s cross correlation function`s maximum is negative, because the target was metallic. It is know that object with good conductivity scatters the signal in 180° phase shift. Also the direct signal`s correlation function`s maximum is negative. In this case it is negative, because antennas reflector has changed the transmitted signal different as it was when antennas was facing each other. When the target`s material is unknown it is useful to estimate the mean time between correlation function`s positive and negative maximums to minimize possible errors.

2.3 Antenna directivity

Transmitting antennas directivity was measurred. Butterfly shaped antenna with 90° angle refflector was used. (**Fig. 2.7**).

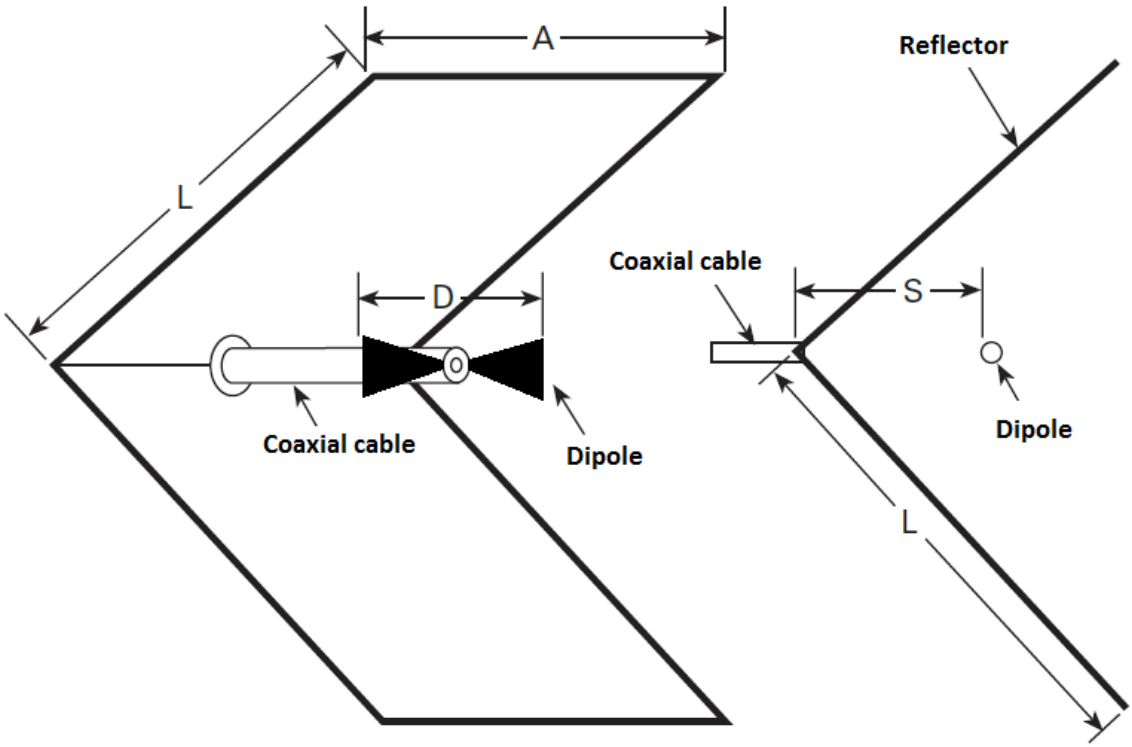

Fig. 2.7 Used antenna

Dimensions:

- L = 20cm
- A = 20cm
- D = 10.5cm
- S = 14cm

Used butterfly shaped antennas directivity without reflector is the same as classic Hertz dipole. Reflector narrows the directivity of the antenna. (**Fig. 2.8**).

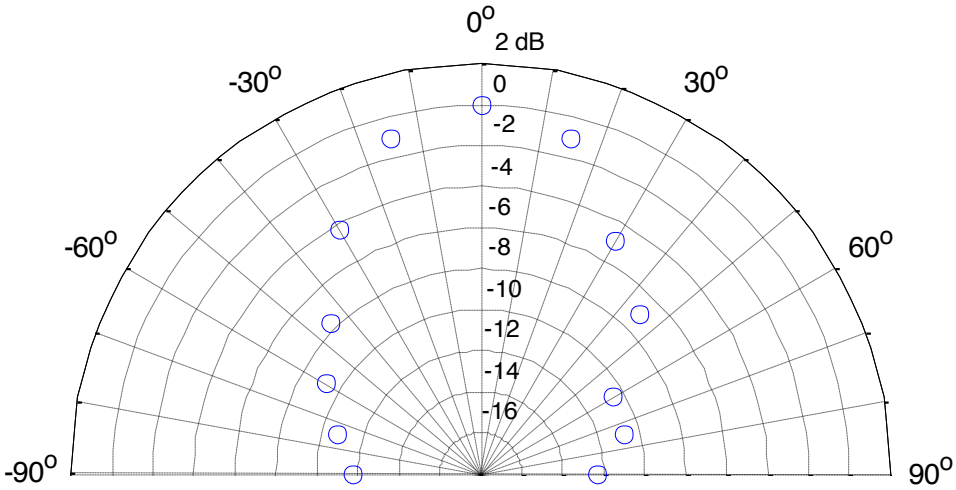

Fig. 2.8 Antennas directivity

2.4 Experiments with the model of receiver and antenna system

Calculations have been done to determine the locator input RMS value, depending on the tunnel diode parameters used in the receiver. It`s capacity is $C_1 = 0{,}84pF$ and RMS of input noise is $\sigma_1 = 198{,}49\ mkV$ at peak current $I_p = 5mA$, Theoretical calculations and experimental obtained values of noise are equal. The results can be used to choose the correct parameter for ("up-and-down") method.

During the research we made antennas with different types of reflector (shapes and sizes), tested many options how far the reflector stands from antenna, we found the optimal reflector set in antenna and its configuration (Figures 2.4.1, 2.4.2).Transmitting and receiving antenna have been made. Directional sensitivity is shown in Figure 2.4.3.

Fig. 2.4.1 Optimal reflector of antenna

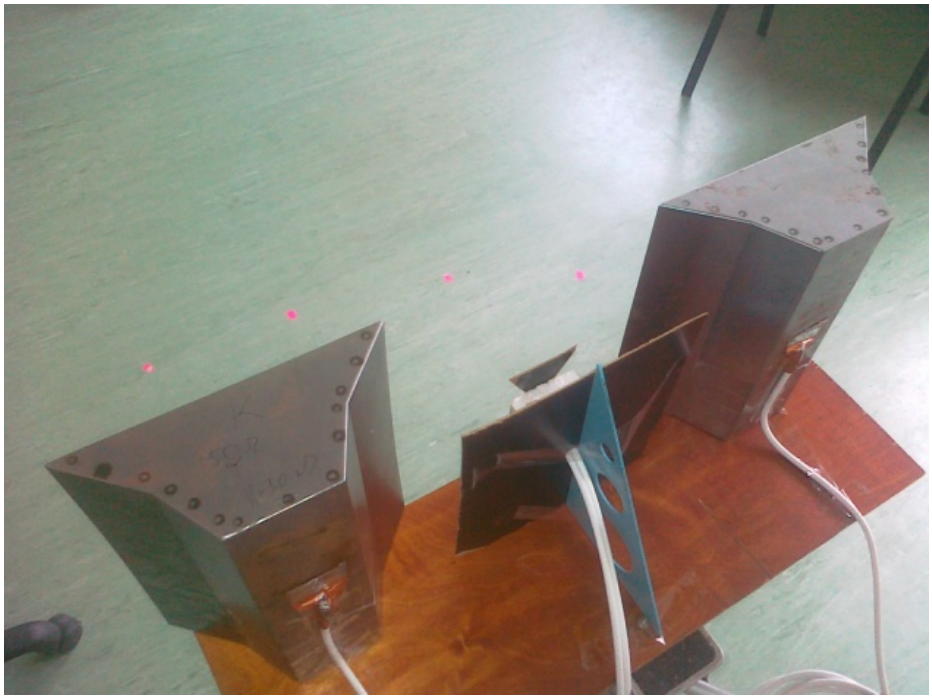

Fig. 2.4.2. Optimal reflector of antenna top view

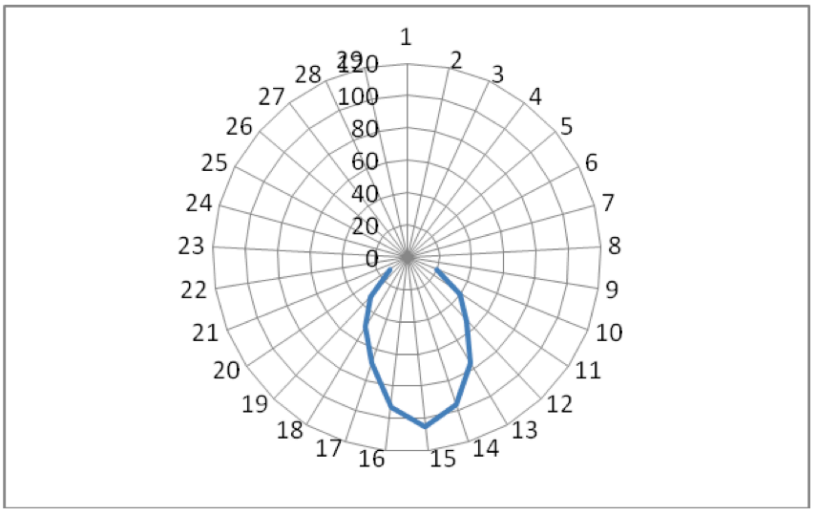

Fig.2.4.3. Experimentally obtained directional sensitivity graph

Using the locator layout and the fabricated antennas, we have obtained data from the objects in reflected signal. This data has been used for a number of signal processing algorithm evaluation (averaging, convolution, window filter, etc.). Results so far have shown, that convolution method is the most promising for TWV applications.

We have started to develop a mobile and compact signal processing unit, based on TQ6410 S3C6410 ARM11 Dev Kit with 4.3" TFT Touchscreen running Windows CE 6.

2.5 Future plans

Experiments with the model of receiver (digital sampling converter was used, signals registered with „up-and-down" method) show that the configuration can be used in TWV signal processing because of its very low input RMS.

One of the main tasks we are planning to do is signal processing in multiple receiving antenna system. Hopefully it would allow to locate a targets in 3D.

3 Transportlīdzekļu kā sensoru un aktuatoru mezglpunktu attīstīšana viedu transporta sistēmu izveidei, ietverot dažāda veida iegulto sistēmu pielietojamības izpēti, precīzas pozicionēšanas, adaptīvās kruīzkontroles, efektīvas bezvadu komunikācijas izstrāde

IEEE 802.11p is a novel international standard, approved in 2010, for intelligent transportation system communication, having wide range of applications. Device with 802.11p support has a huge economical potential, when industrial partners are involved. In addition, rapidly increasing popularity of smartphones, Android platform in particular, motivates research of this platform as a sensor node solution. Potential economical applications are related to commercial Android sensor network software solution development for intelligent transportation system applications and road infrastructure damage identification, using participatory sensing approach.

The results obtained in this period:

1. Intelligent transportation system communication platform prototype supporting IEEE 802.11p protocols developed, Section 3.1;
2. Computer-driven brake pedal management solution, based on pneumatic system, implemented, Section 3.2;
3. Practical cooperative cruise control tests in Grand Cooperative Driving Challenge (GCDC 2011) [3.1] performed, Section 3.2;
4. Hybrid positioning algorithms, fusing GPS and IMU using Kalman filters, implemented, Section 3.3;
5. Android smartphone applicability for vehicular sensor network applications, including pavement quality analysis, researched, Section 3.4
6. Directional antenna testbed improvement and test automation performed, Section 3.5

Future work:

1. Wireless car node development and testing
2. Vehicular sensor network application research

3.1 ITS Communication Prototype, Supporting IEEE 802.11p

Although 802.11p standard is evaluated in the research community for a while already, commercial 802.11p solutions are available for research only, not real users. We have created a car 802.11p wireless communications platform using commercially available components. System performance and usability tests show that our platform is well suited to car communication on distance up to 1.2km.

3.1.1 Hardware

To provide a low-cost 802.11p communication solution between participating vehicles, a router was used (Figure 3.1.1) as a bridge between wired car-area-network and 802.11p wireless network. It consisted of PC Engines ALIX.2D2 router [3.1.1] with 500 MHz AMD Geode LX800 CPU (x86 architecture), 256MB SDRAM, 8GB Kingston CompactFlash memory, Unex DCMA-86P2 miniPCI 802.11p wireless module [3.1.2], two 100Mbps Ethernet ports. Powered by 12V DC, the energy consumption was below 10W (below 5W with radio turned off). External antenna (omnidirectional vertical collinear antenna with 20 1/2 wave elements and approximate gain 10 dBd) was used.

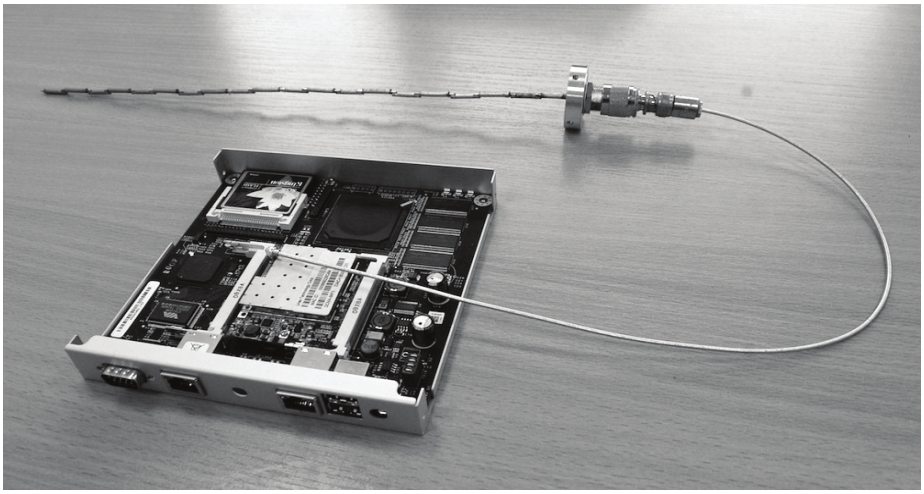

Fig. 3.1.1. 802.11p router with external antenna

3.1.2 Software

This section describes the central part of our software solution: test controlling application, running on the ALIX2 wireless router with OpenWRT Linux OS. It communicates with Laptop (Ubuntu Linux 11.10), using Ethernet connection. GPS receiver is connected to Laptop's USB.

One process was running on the Laptop logging GPS data and providing IP socket (for processes that run on ALIX boards) with precise GPS time. Another process was created on one of routers that simultaneously ran 3 programs (iperf in server mode, ping and iw), saved data to log files and converted these log files to MATLAB script files. Second router was continuously running iperf (UDP client with maximal bandwidth set) process that provided UDP connection to the first router.

Used software tools:

1. IPERF – measure jitter, bandwidth and packet loss;

2. PING – measure packet travel time;
3. IW – measure received signal strength.
4. Custom server program – saving log with GPS data and providing IP socket for other processes with accurate GPS time;
5. Custom client program – receive accurate time from the server;
6. Custom test program – simultaneously run 3 programs (iperf in server mode, ping and iw), log the data to MATLAB script files.

3.1.3 Test setup

Several tests were performed, to assess connection performance and reliability dependence on distance between a static base station and a vehicle passing by at different speeds.

Tests were carried out on an aerodrome, on a rainy day, having humidity level at 96%. The antenna was positioned on the roof of a vehicle passing by a static base station on the roadside, 1.5 meters above the ground, representing roadside unit. Direct visibility was ensured between both ends.

Three tests were running simultaneously:

1. Sending a UDP packet with a maximum rate once a second;
2. PING with 160b packet;
3. RSSI signal testing every 4.2s (with “iw wlan0 scan” Linux command).

Performed tests:

1. Distance test, driving back and forth 2.4km distance at speed 25 km/h. Maximal UDP data transmission mode, no ping.
2. Distance test, driving back and forth at speed 50 km/h. Maximal UDP data transmission mode, ping 160b;
3. Distance test, driving back and forth at speed 90 km/h. Maximal UDP data transmission mode, ping 160b;
4. Motion along an ellipse stretch, base station located in the center of it. Largest radius 1.2km, two full laps repeated. Maximal speed 50 km/h.

3.1.4 Results

Results show, that reliable data transmission (more than -85dBm) can be maintained with the help of the given platform to 1.2km. Further link is unstable, however, partial communication is available up to 2.4km with the particular antenna.

Figure 3.1.2 shows received signal strength (RSSI) depending on the distance between vehicle and roadside unit. There is a difference in signal strength depending on the direction: the signal is weaker when leaving the base station, than when the vehicle is approaching it.

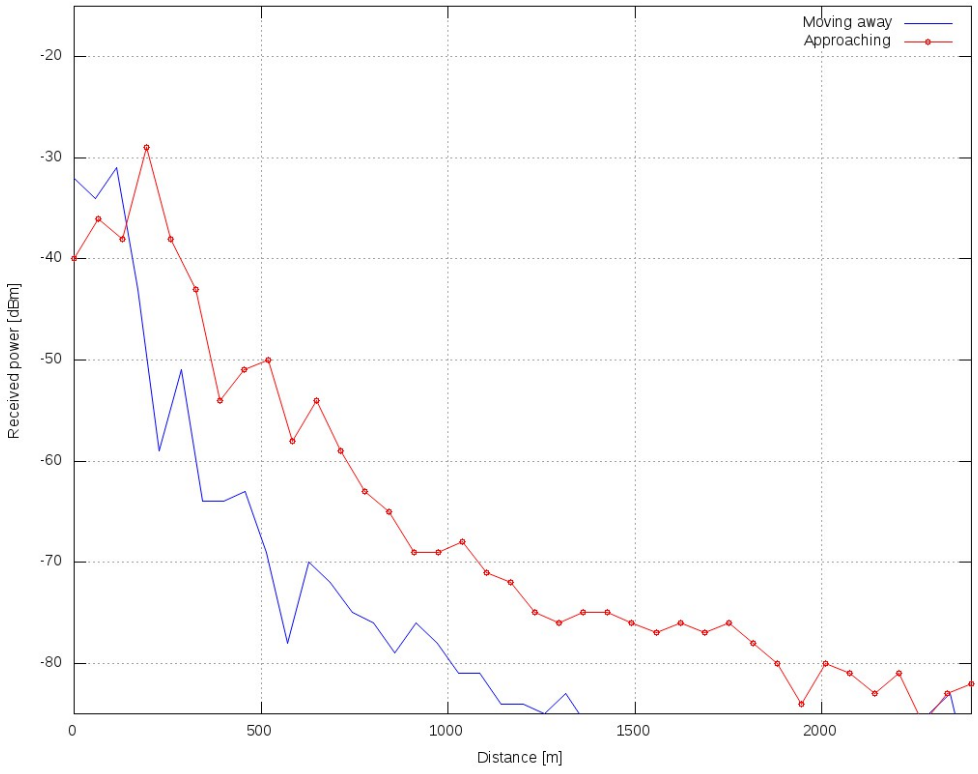

Fig. 3.1.2. Received signal strength dependence on distance and direction between the vehicle and base station: the vehicle is either approaching (red) or leaving (blue) base station

This issue is more expressed in Figure 3.1.3, which shows results of packet travel time measurements. One hypothesis is a potential directionality effect of the antenna. The true reasons should be further investigated.

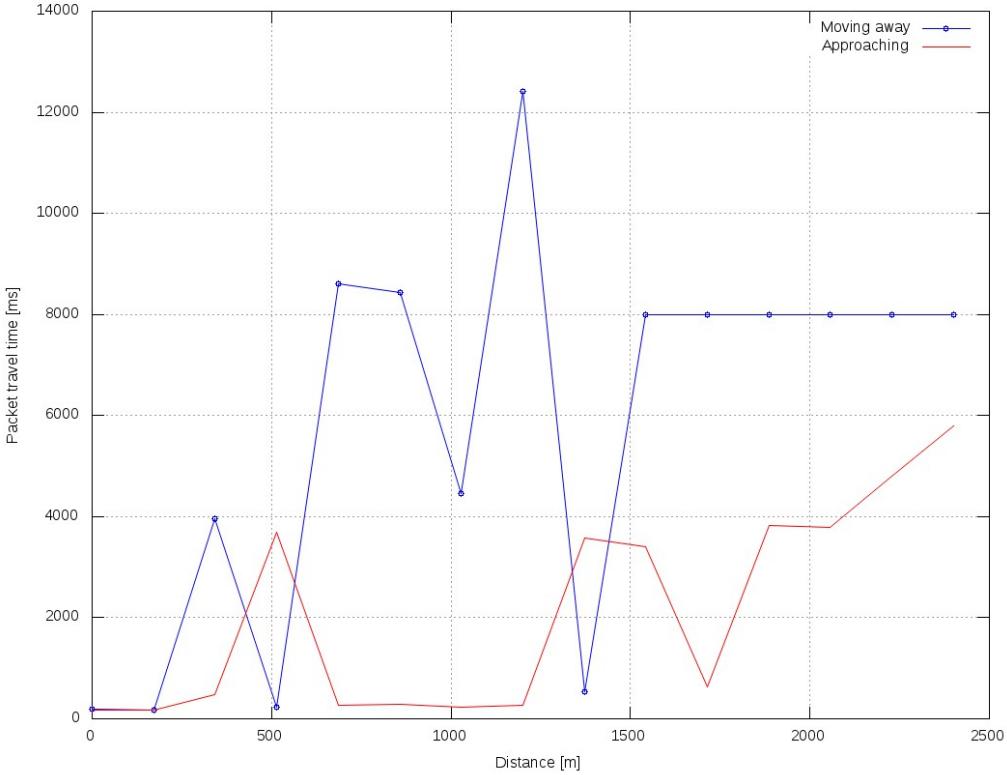

Fig. 3.1.3. Packet travel time dependence on distance and direction between the vehicle and base station: the vehicle is either approaching (red) or leaving (blue) base station

All tests are referenced to received power loss, therefore bandwidth (Figure 3.1.4), jitter (Figure 3.1.5), packet travel time, and packet loss are derivatives of signal strength.

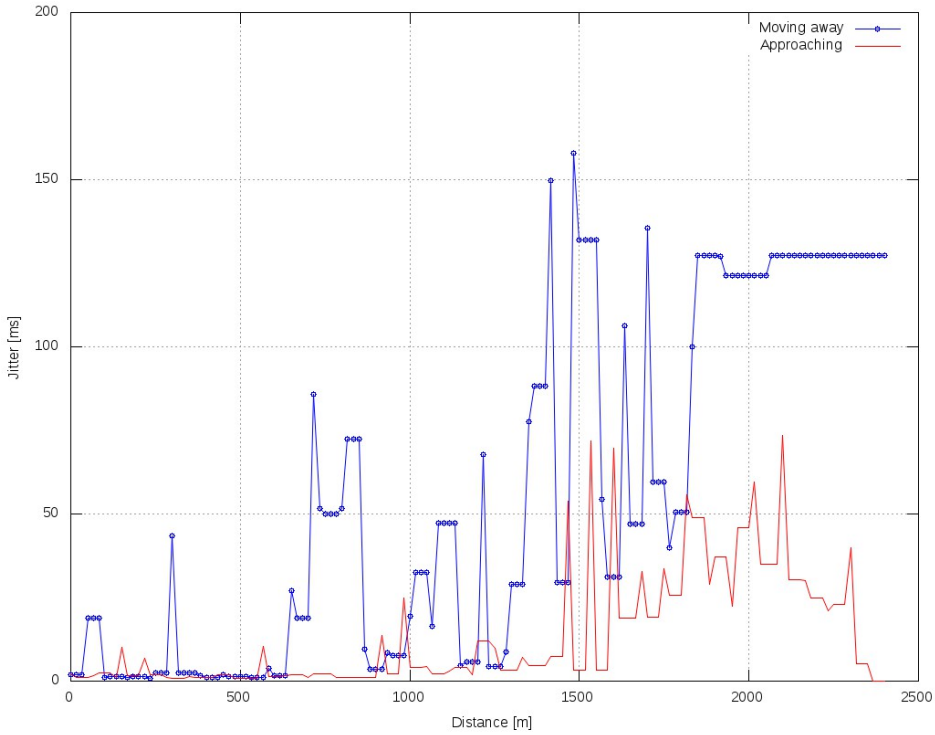

Fig. 3.1.4. Bandwidth dependence on distance and direction between the vehicle and base station: the vehicle is either approaching (red) or leaving (blue) base station

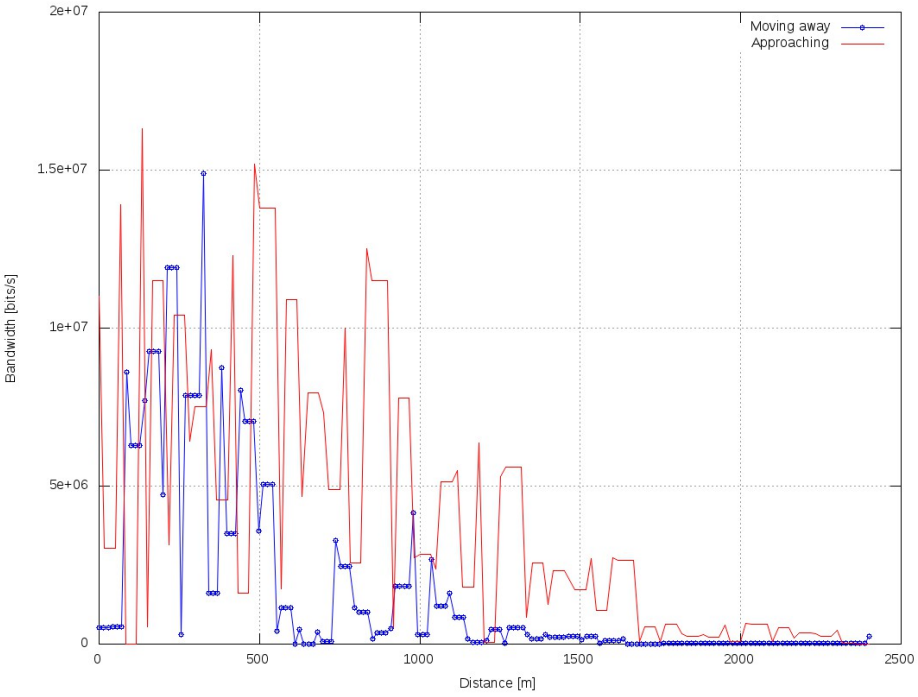

Fig. 3.1.5. Jitter dependence on distance and direction between the vehicle and base station: the vehicle is either approaching (red) or leaving (blue) base station

At higher speeds (80km/h) RSSI is slightly lower, see Figure 3.1.6.

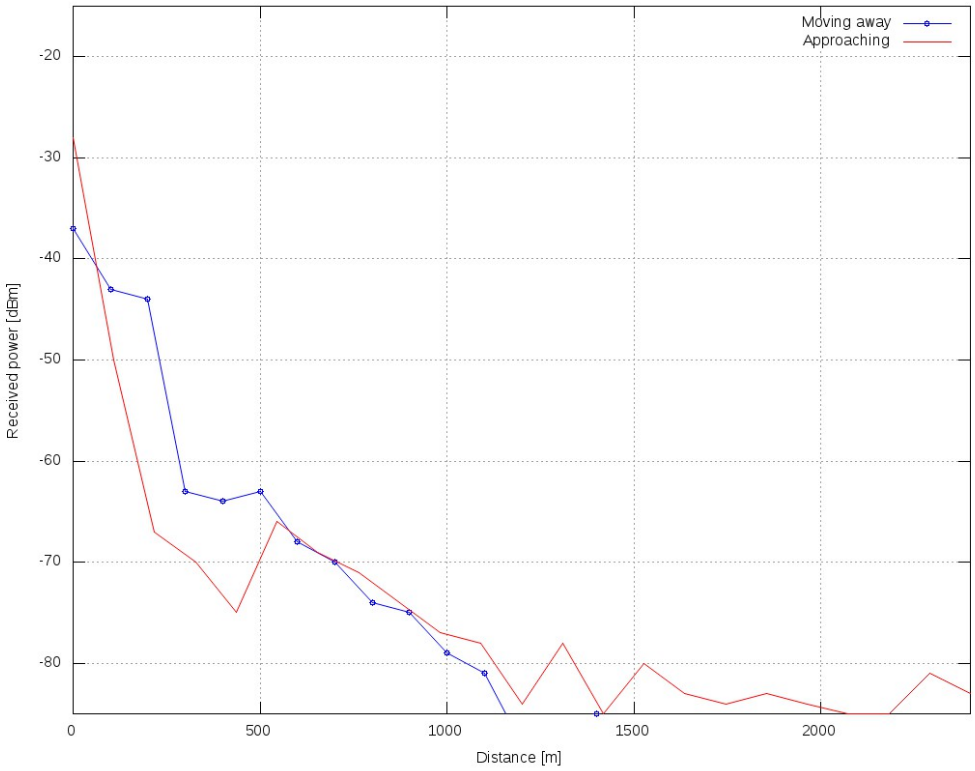

Fig 3.1.6. Third test: bandwidth dependence on distance, vehicle moving at 80km/h

Figure 3.1.7 shows RSSI in the 4th test: vehicle driving in elliptic circles with base station located in the center of it. RSSI is rather stable when leaving base station. However, it differs heavily when approaching it.

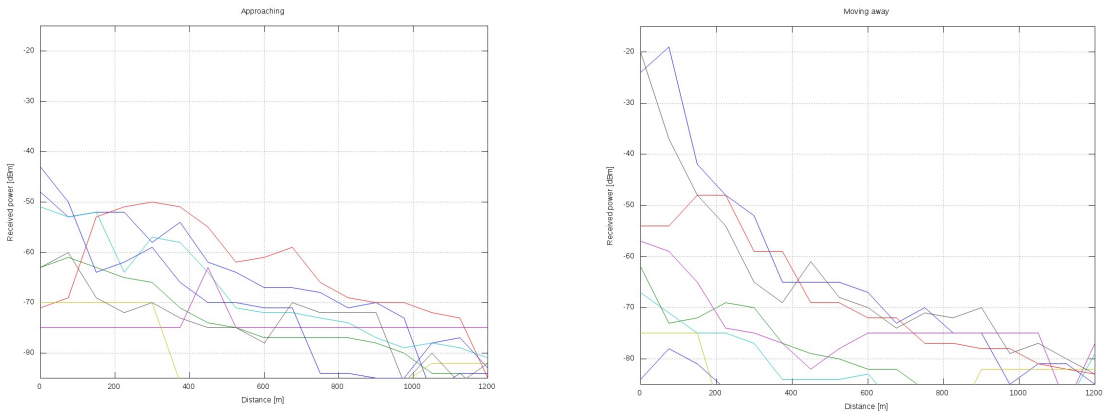

(a) (b)

Fig. 3.1.7. RSSI in the 4th test: vehicle driving (a – approaching, b – leaving) in circles, base station located in the center.

3.1.5 Discuccion and conclusions

A preliminary test was performed two days before the described tests. Environmental temperature was -6^0C, and routers were functioning unstable – data transmission experienced disturbance, probably caused by oscillator frequency shift. In the described tests incandescent was inserted into the case of each router to warm them.

Antenna was placed closer to one side of our vehicle in the tests. It should be placed in the middle of the roof to avoid effect of vehicle shape on the transmitted signal.

Nevertheless, communication range exceeding 1km is more than required in urban applications. Therefore even less sophisticated antennas are usable for vehicular communication scenarios.

Future work includes more deep analysis of communication directionality effect cause and platform applicability evaluation in real use cases.

3.2 Cooperative Cruise Control Implementation And Testing

First version of brake control system was built and successfully tested on GCDC competitions held on May 2011.

System tests have shown that brake control system is able to drive car brake pedal and stop car.

System disadvantages were:

- Small volume of receiver – in case of frequent and fast braking receiver pressure was falling too fast.

- It was hard to control smooth braking while car was almost stopped – it was needed to decrease slowly air pressure on the pressure cylinder, otherwise passengers felt shock caused by energy collected by car springs.

It was calculated that air consumption could reach up to 20l/min with nominal air consumption 5l/min. Because air compressor was fulfilling parameters (maximal supplied air flow 30l/min) larger (5l) air pressure receiver was put into system. It helped to decrease load on to compressor.

To control braking pedal precisely was planned to install electro pneumatic pressure control module.

Upgraded brake pedal control system (Figure 3.2.1) was simulated in FESTO FluidSim software [3.2.1]. It contains (1) air supply unit (compressor unit, air receiver and air pressure sensor on receiver), (2) pressure shut off electro pneumatic valve, (3) electro pneumatic pressure control unit, (4) pressure release electro pneumatic valve (5) pneumatic cylinder, (6) pressure sensor.

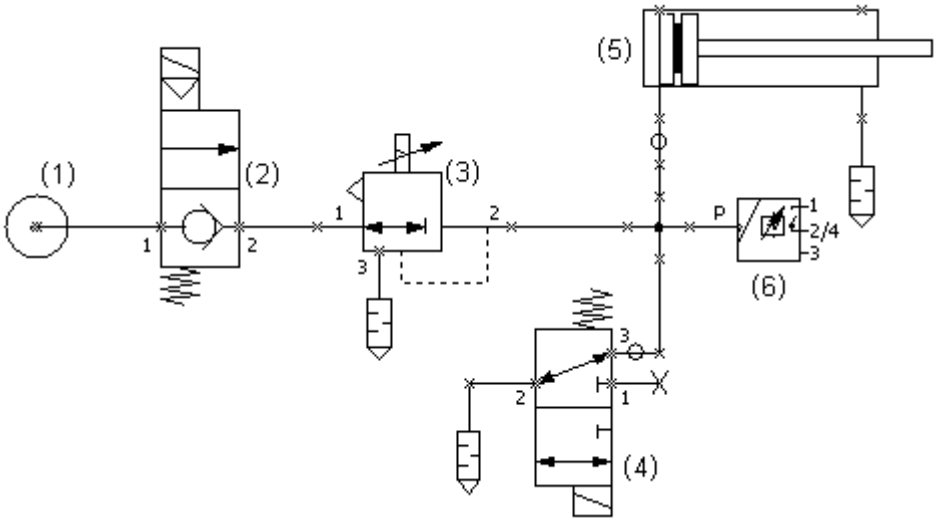

Fig. 3.2.1. Upgraded brake pedal control system

Other elements, not displayed on the diagram, are:

- Control system
- Brake pedal travel sensor
- Mechanical pressure sensor on the break pedal

Valves (3 and 4) were installed for emergency purposes. In case of emergency valve no. 3 will disable air pressure supply and valve no. 4 will drive all of the air pressure out of the pneumatic system, allowing user to control brake system.

Chosen electro pneumatic pressure control unit ITV1051-212BL3-Q is designed for pressure range up to 9bar, can supply up to 200l of air per minute. It can be powered by 12 to 15 VDC and driven using analogue voltage signal from 1 to 5 V.

As a feature it has analogue output and digital display for representation of output pressure.

Together with pneumatic scheme a simple control algorithm was created.

While driving the car, control unit is receiving data about environment around the car - distance to obstacles (other cars, pedestrians, road signs, road environment objects). Car control unit stores speed of the car and can calculate speed difference between the car and obstacle. It then calculates time in which an obstacle will be reached. If it is needed to stop near such object, or equalize speed of car and object on defined distance, next step is to calculate needed negative acceleration $\vec{a}_1$.

As a consequence, brake control system is being actuated by increasing air pressure in cylinder, and accelerometer measures real acceleration of the car $\vec{a}_2$. If the real acceleration is insufficient, air pressure in cylinder must be increased and brake system is being actuated. Else, if the real acceleration is higher and the car will stop significantly earlier then needed, air pressure in cylinder can be decreased.
After a time 3D matrix from aquired data is created. It includes information about speed of the car, distance to an object and needed pressure in the cylinder.
Each time, system is enabled new parameter is put into the matrix. Previous values help to operate cylinder faster, keeping system away from recalculation of data and significantly decreasing amount of iterations needed to make corrections.
This method helps to make algorithm adaptive, so it will change parameters with change of condition of braking system.

Planned future planned work includes simulation of brake control system operation using generated GPS and accelerometer data and development of brake control system physical model on the table and load-testing.

3.3 Hybrid GPS and IMU Positioning System Implementation

In our previous work, hybrid GPS and IMU positioning system implementation was proposed. This combination is possible and it has the performance superior to either subsystem because GPS and IMU have very complementary error characteristics.

Vehicle system state is represented by an n-dimensional random variable x with mean and covariance ($E(x)$, P_x). The main goal is to find mean and covariance ($E(y)$, P_y) where $y=f(x)$ is a transformed random variable and f is a non-linear function that defines time update transformation of vehicle position, velocity, attitude and sensor data biases. There are a lot of different algorithms that can be used for this non-linear function estimation. The Extended Kalman Filter (EKF) has been considered the *de facto* standard in the theory of nonlinear state estimation but it is difficult to tune, the Jacobian can be hard to derive, and it can only handle limited amount of nonlinearity. On the other hand, Particle Filter (PF) can handle arbitrary distributions and non-linearities but it is computationally very complex. Sigma-Point Kalman filter (SPKF) gives a nice tradeoff between PF and EKF so it was proposed to use for the defined non-linear system estimation and sensor data fusion.

SPKF is not a single algorithm. It is an algorithm family based on "Unscented Transformation". The main idea of this transformation is that the state distribution is represented by a Gaussian random variable, but is specified using a minimal set of carefully chosen sample points. These sample points completely capture the true mean and covariance of the Gaussian random variable, and when propagated through the *true* non-linear system, captures the posterior mean and covariance accurately to the 3rd order (Taylor series expansion) for *any* nonlinearity.

Several SPKF implementations exist, e.g. Unscented Kalman Filter (UKF), Square-Root Unscented Kalman Filter (SRUKF), Central Difference Kalman filter (CDKF) etc. Each of them implements "Unscented Transformation" with some specific modifications such as choice of sigma-point selection scheme (weights and scaling factors) and method by which the propagated sigma-points are combined in order to calculate the posterior covariance matrix. UKF was implemented in the navigation software first but it has two main drawbacks:

- Cholesky decomposition used to get a square root of a covariance matrix is computationally expensive;
- Covariance matrix should be symmetric and positive definite.

To overcome the above defined problems SRUKF was implemented. In SRUKF Cholesky decomposition is replaced by QR decomposition and rank 1 update to Cholesky factorization combination. As a result there is no need to compute square root of the covariance matrix on each iteration, there are no restrictions on the covariance matrix, algorithm asymptotic complexity is significantly decreased and numerical stability is improved.

3.3.1 Navigation system software

Navigation system software is implemented as a C/C++ Makefile project. The project can be divided into two main parts, i.e. release and sandbox code which are partially separated. Release code is a tested navigation system code that can be used on real data and applied in other applications. On the other hand, sandbox code is used for testing new features, algorithms, approaches etc. Both parts have several common modules, i.e. math structures and functions (includes Kalman Filter related things and motion analysis functions), UART communication module, user interface components, data conversion and parsing functions. However, "data simulation" is a sandbox specific thing that allows sensor data generation for easier algorithm testing and demonstration without having any sensor modules at all.

3.3.2 Navigation system testing in a virtual environment

To be sure that navigation system code (version 1.0) have no serious bugs, testing in a virtual environment (data simulation mode) was processed.

The first testing scenario task was orientation estimation where accelerometer and gyroscope data was used to compute orientation (orientation is represented by Euler angles) (Figure 3.3.1). Noise with a Gaussian distribution was added to sensor data. Accelerometer data (x, y, z axis) is shown on the left, gyroscope data (x axis) is shown on the right and an estimated orientation is shown on the bottom of the figure. As it can be seen, an estimated orientation using accelerometer data has no bias but it is very noisy. On the other side, an estimated orientation using gyroscope data has a bias but it is not so

noisy as a previous result. But an estimated orientation using both accelerometer and gyroscope data applying Kalman Filter is quite close to the ideal orientation.

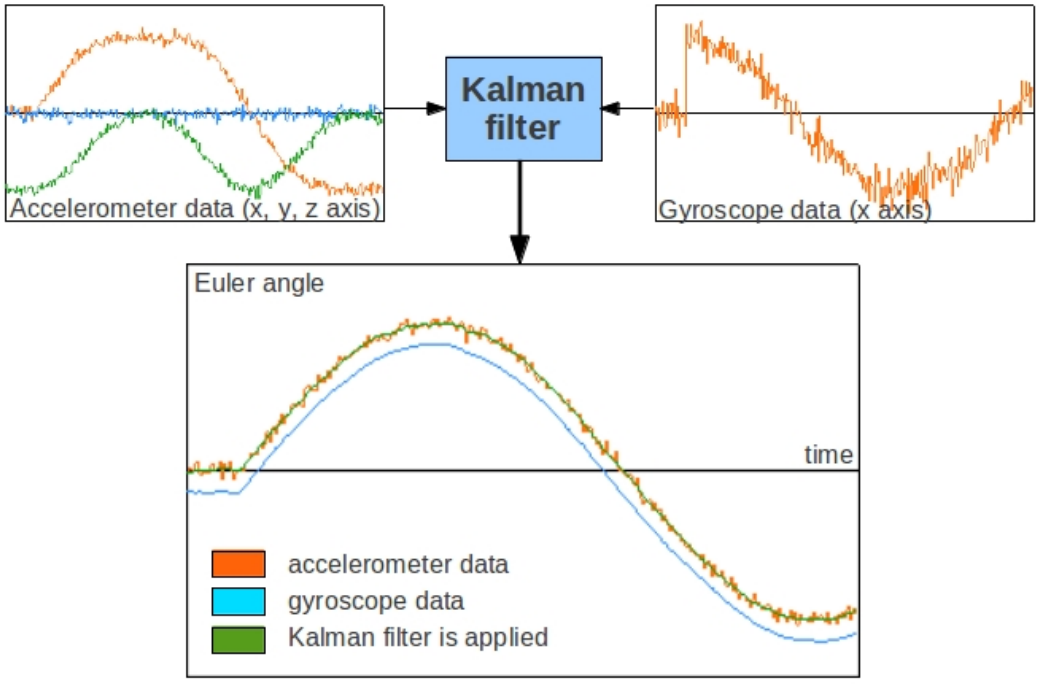

Fig. 3.3.1. Simulated orientation estimation

The second testing scenario task was position and orientation estimation where accelerometer, magnetometer and GPS data was used to compute position and orientation (orientation is represented by Euler parameters in a quaternion form) (Figure 3.3.2). Noise with a Gaussian distribution was added to sensor data. As it can be seen, an estimated trajectory using accelerometer and magnetometer data has a bias that accumulates in time due to noisy acceleration data integration process. On the other side, an estimated trajectory using GPS data has no bias and has no noise but it is not good due to the low position update frequency. But an estimated position using both, accelerometer, magnetometer and GPS data applying Kalman Filter is quite close to the ideal trajectory.

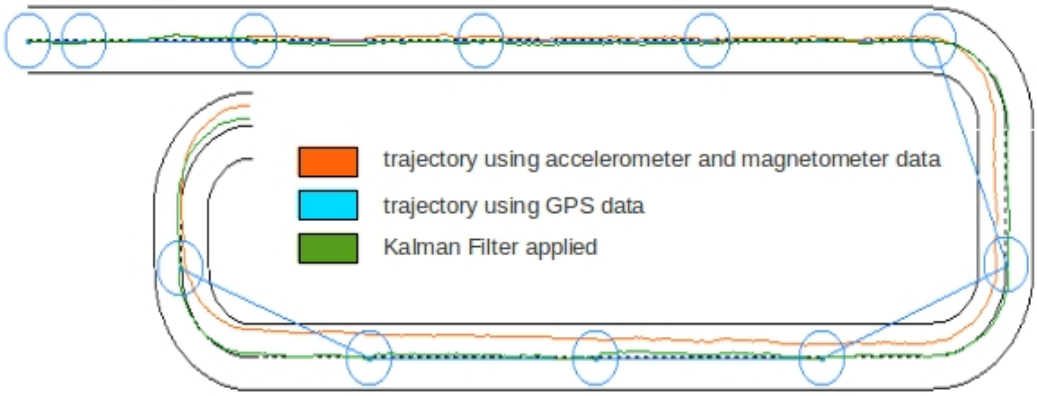

Fig. 3.3.2. Simulated position and orientation estimation

Future work would include testing navigation software in the real environment on real data and release of navigation system as a library to use in other projects.

3.4 Android Smartphones For Vehicular Sensing Applications

In our previous work, road damage detection using audio signal analysis was assessed [3.4.1]. Laptop computer with external microphone was used as prototype platform. The results showed feasibility of the approach. In the new research several questions were stated: "Is Android smartphone platform usable as an alternative to PC for pothole detection? What algorithms are reasonable? What accuracy can be expected?"

Sensing system architecture was developed, Figure 3.4.1. It consists of Android smartphones, carried in vehicles by the drivers [3.4.2]. Online pothole detection algorithms are running directly on the device, detected events are sent to a central server for data fusion and dissemination among interested parties. The proposed architecture is extensible to detection of other types of events, including weather conditions on the road, car accidents and other emergency situations.

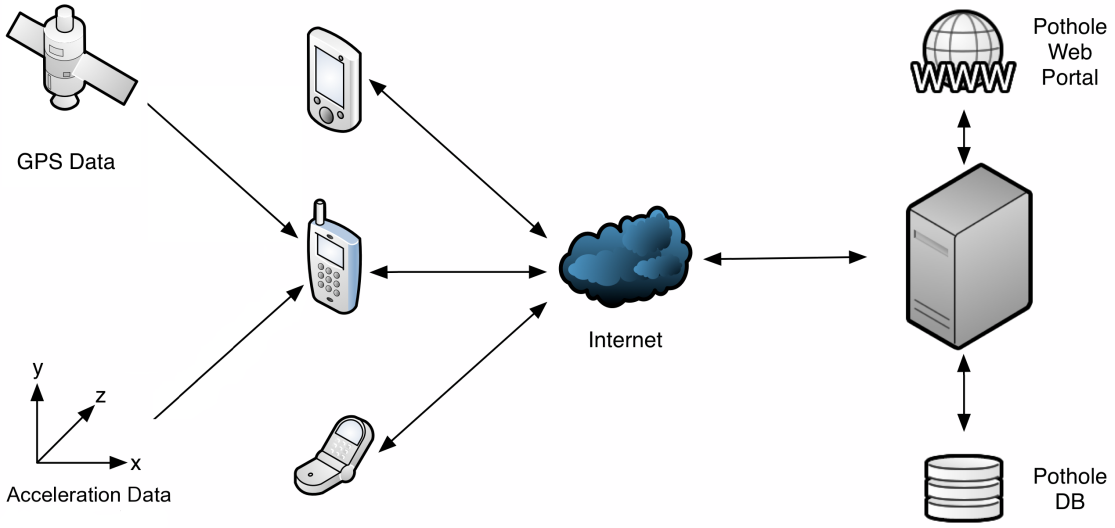

Fig 3.4.1. Architecture of vehicular sensing system using Android smartphones in driving vehicles for data gathering and event detection, and central server performing data fusion and dissemination

Experiments in realistic urban environment were performed to assess usability of the approach [3.4.3]. Positions of 108 potholes on a 4.4km long test track were marked manually, dividing them in 5 classes: large pothole, small pothole, pothole cluster, gap and drain pit. A test car with multiple android devices was driving 10 test laps on the track while recording accelerometer and GPS data for pothole detection. Audio signal processing proved to be not directly usable, as automatic gain control is performed by the operating system to mitigate background noise influence to phone conversation quality. Therefore sensors of another type were used: accelerometers, which are available on all Android phones produced at the moment. Accelerometer sensor data was processed, using 4 algorithms: Z-THRES, Z-DIFF, STDEV(Z) and G-ZERO, described in more detail in [3.4.4].

As shown in Figure 3.4.2, 92% of all manually marked potholes were detected by Z-DIFF algorithm, while maintaining 23% false-positive rate (which corresponds to 100% minus true_hits). While STDEV(Z) algorithm is slightly more inaccurate, it filters out drain pits more efficiently, see Table 3.4.1. Although, accuracy of single pothole detection algorithm running on a single Android device is unsatisfactory to be used alone, authors believe, that combination of multiple algorithms and fusion of detection results of multiple users (multiple devices) would provide accuracy high enough to be usable in industrial applications and public services.

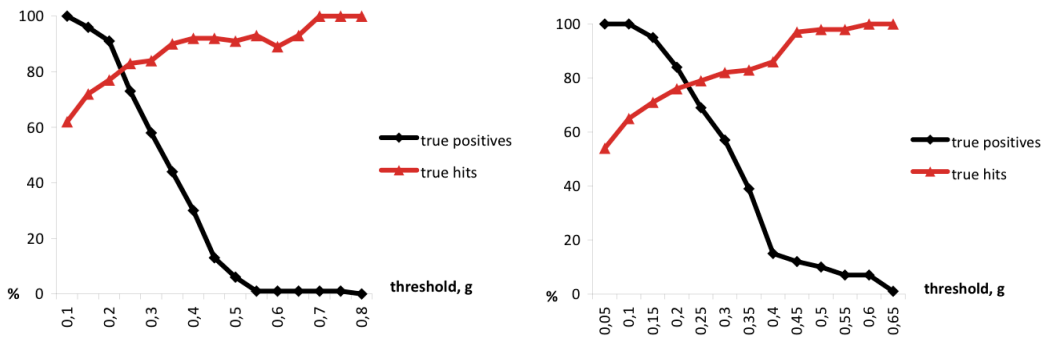

(a) (b)

Fig. 3.4.2. Pothole detection algorithm accuracy: (a) Z-DIFF algorithm finds 92% of marked potholes (true positives) while 77% of all detected events are in close vicinity of at least one marked pothole (true hits); (b) STDEV(Z) algorithm detects 81% of real potholes having 76% true hits

Table 3.4.1. True positive rate for particular road damage classes: while total detection rate is lower for STDEV(Z), it is more accurate in filtering out drain pits

Class	Z-DIFF	STDEV(Z)
Large potholes	3 (100%)	3 (100%)
Small potholes	16 (89%)	16 (89%)
Pothole clusters	27 (90%)	27 (90%)
Gaps	36 (90%)	30 (75%)
Drain pits	17 (100%)	11 (65%)
Total	99 (92%)	87 (81%)

Results of the research show that Android is a promising platform for vehicular sensing applications with potential to be used in public sector as participatory sensing approach for road maintenance task improvement. Further investigation on data fusion and cooperation among multiple sensing platform users would be required to draw more accurate conclusions about the systems accuracy.

3.5 Directional Antenna Testbed Improvement

Directional antennas are widely used in data transmission. In vehicular sensor networks there are number of requirements set for such antennas. Electronic change of transmission direction, low power consumption, limited size and shape and high gain are the most significant.

In our previous work, prototype of such antenna was designed. To explicitly evaluate antenna parameters and to find optimal regulations and tuning's of our built antenna prototype significant hardware upgrade of our previously built test bed was made:

- Stationary directional antennas added to support higher gain tests and to improve control channel stability. Using of stationary directional antennas also allow to test direction of attenuation
- More precise and less noisy stepper driver designed and installed, to reach direction measurements up to 0.45^{o} accuracy and to get less impact on radio measurements
- Optical start – stop position detector designed and installed, which helps in cases when two or more antenna prototypes should be compared in some direction with high accuracy
- Extra wireless sensor node added for control of communications, stepper driver and optical start detection module
- Attachable dipole antenna (2.15dBi) for calibration purposes added. Newly introduced calibration will allow us to reason not only about ratio of prototypes but also to measure explicit gain of antennas under test

The schematic representation of upgraded testbed is displayed on Figure 3.5.1. There you can see all the newly introduced parts of test system

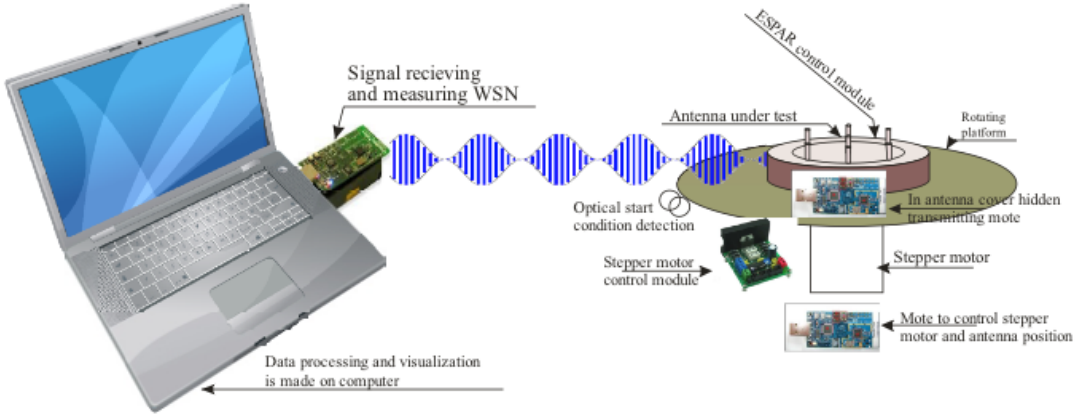

Fig. 3.5.1. Architecture of Antenna test bed hardware

For purposes of antenna parameter evaluation and tuning a computerized testbed control system was made.

The key features of designed software are:

- Ability to perform all actions remotely
- Set antenna under test to some exact position (accuracy 0.45^{o})
- Perform radiation diagram plot with selected accuracy (0.45^{o}, 0.90^{o}, 1.80^{o})
- Control antenna settings (capacitances of parasitic elements) from computer (though WSN via $I^{2}C$)
- Control transmit power in the input of antenna under test
- Calibrate testbed (based on analytical calculations of dipole antenna gain)
- Save test results weather as image or list of data acquired

In Figure 3.5.2 the result of test bed system's calibration phase is shown. The red grid line values are calculated on the basis of test (calibration) dipole (blue circle) measurements.

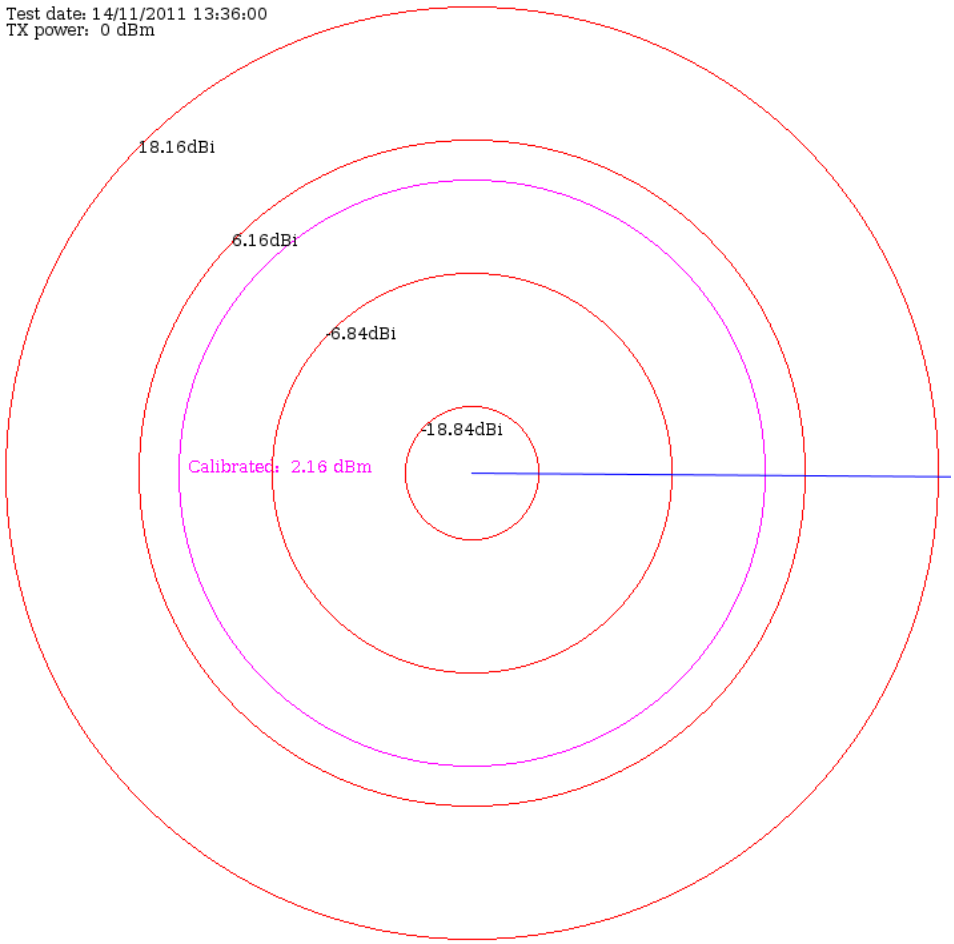

Fig. 3.5.2. Calibration result of antenna testbed software

The computer side software is coded in Java programming language. The source code is open source so there are many possibilities to adjust this software for user needs.

This testbed is designed especially for electronically steerable antenna testing, however, it could be used for testing other antenna types as well. There are interfaces allowing testing procedure automation when dozens of different antenna settings need to be tested and saved. This system is used in our research now, and it is supposed to be used in our future research of electronically steerable antennas, especially when real world tests of new algorithms of antenna "on the fly" adjustments will be necessary.

References

[3.1] Grand Cooperative Driving Challenge (GCDC 2011), [Online] http://www.gcdc.net [Online]

[3.1.1] PCEngines, Alix.2D2. [Online]. Available: http://pcengines.ch/alix2d2.htm

[3.1.2] Unex, DCMA-86P2: 5.9GHz DSRC wireless mini-PCI. [Online]. Available: http://www.unex.com.tw/product/dcma-86p2

[3.2.1] Festo FluidSIM®. [Online]. Available: http://www.festo-didactic.com/int-en/learning-systems/software-e- learning/fluidsim/

[3.4.1] A. Mednis, G. Strazdins, M. Liepins, A. Gordjusins, and L. Selavo, “Roadmic: Road surface monitoring using vehicular sensor networks with microphones,” in NDT (2), ser. Communications in Computer and Information Science, F. Zavoral, J. Yaghob, P. Pichappan, and E. El-Qawasmeh, Eds., vol. 88. Springer, 2010, pp. 417–429.

[3.4.2] G. Strazdins, A. Mednis, G. Kanonirs, R. Zviedris, and L.Selavo, "Towards Vehicular Sensor Networks with Android Smartphones for Road Surface Monitoring," in the 2nd International Workshop on Networks of Cooperating Objects (CONET’11), Electronic Proceedings of CPSWeek'11, April 11, 2011.

[3.4.3] G. Strazdins, A. Mednis, R. Zviedris, G. Kanonirs, and L.Selavo, “Virtual Ground Truth in Vehicular Sensing Experiments: How to Mark it Accurately”, in the 5th International Conference on Sensor Technologies and Applications (SENSORCOMM’11), pp. 295-300, August 21-27, 2011.

[3.4.4] A. Mednis, G. Strazdins, R. Zviedris, G. Kanonirs, and L. Selavo, “Real Time Pothole Detection using Android Smartphones with Accelerometers”, in the 2nd International Workshop on Mobility in Wireless Sensor Networks (MobiSensor'2011), pp. 1-6, July 29, 2011.

4 Bioloģiskas izcelsmes signālu ieguves un to ievades apstrādes sistēmās paņēmienu un apstrādes algoritmu attīstīšana, ieskaitot laika kodēšanas pieeju un kompleksās salāgotās filtrēšanas uzlabojumus

Acquisition and interpretation of biological signals is important not only as a powerful human-computer interface, but also can give great insight in the functions of human body. The goal of this research is to provide better insight and tools for reading and understanding biological signals, and also to use this knowledge as a tool for behavioral improvement by providing feedback to the acquired actions.

Uses of this research include, but are not limited to, person identification, using palm vein biometry, computer input driven by thoughts or body language, posture correction in scoliotic patients, replacing the more cumbersome back braces and gathering data about the state of the patients and monitoring their recovery.

This task consists of three separate sub-tasks: “Palm vein detection filter improvements” (Section 4.1), “Electroencephalographic helmet for analysis, interpretation and processing of cortical EEG signal” (Section 4.2) and “Smart solutions in diagnostics and hindering the development of scoliosis based on biofeedback generated by sensor networks” (Section 4.3).

4.1 Palm vein detection filter improvements

One of the problems in biometrics is the correct acquisition of the biometric parameters, which in case of palm vein biometrics is the pattern of palm veins. The palm veins are visible in infrared light and appear slightly darker than the surrounding tissue. Signal processing methods, such as line detection algorithms must be used to extract the information about the palm veins and to separate it from a noise and unwanted data. Because of the varying light conditions this task becomes challenging.

Following the idea of previously developed line-like object detection algorithm, named Complex Matched Filtering (CMF), which is an angle invariant line detection filter, the two successors were developed, published and presented in international conferences:

1. Generalized Complex Matched Filtering (GCMF) — a whole bank of angle invariant filters that can detect broader range of specific details including gradients, lines, line crossings [4.1.1].

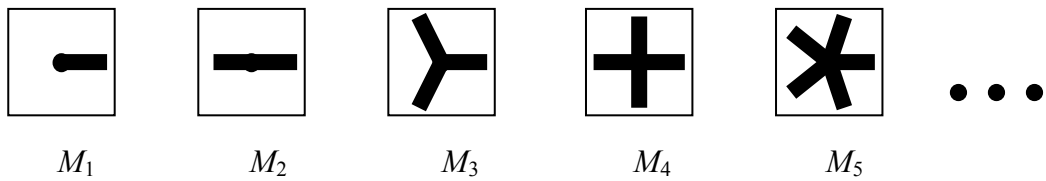

Fig. 4.1.1. First five MF masks used in the GCMF

Details, that are detectable by GCMF of some order K either partially, either fully match the MF mask of the same order from the bank of MF masks, given in Figure

4.1.1. Thus, the $GCMF_1$ is used to detect gradients, $GCMF_2$ — line-like objects, $GCMF_3$, $GCMF_4$, $GCMF_5$ and so on —line crossings of 3, 4, 5 and so on lines.

2. Non-Halo Complex Matched Filter ($NH\text{-}CMF_2$) — is developed to reduce the Halo artifacts, presented in original line-like object detection CMF_2, while leaving intact the desirable functionality of the CMF_2, which is 1) detection of line-like object of desirable intensity, and 2) acquiring the angular orientation of detected objects [4.1.2].

Figure 4.1.2 shows case of filtering the original image (a) with CMF_2 and $NH\text{-}CMF_2$:

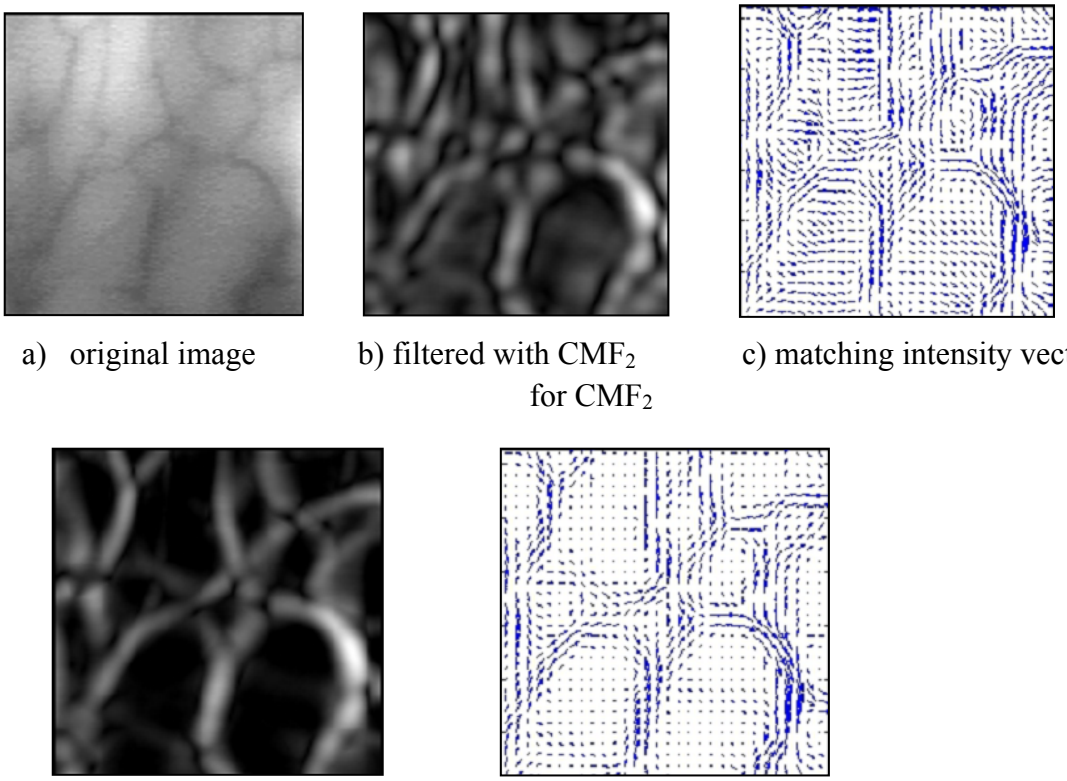

a) original image b) filtered with CMF_2 for CMF_2 c) matching intensity vectors

d) filtered with $NH\text{-}CMF_2$ e) matching intensity vectors for $NH\text{-}CMF_2$

Fig. 4.1.2. $NH\text{-}CMF_2$ comparison with CMF_2

It can be seen that proposed $NH\text{-}CMF_2$ doesn't produce the unwanted Halo artifacts, therefore, the image in (d) appear more pure than the image in (b). The same tendency is found between images (c) and (e).

4.2 Electroencephalographic helmet for analysis, interpretation and processing of cortical EEG signal

Systems based on EEG signal interpretation can alleviate daily routine of the disabled people, as applicability of these systems does not involve physical movement. They also can be widely used in the entertainment industry.

The results obtained in this period:

1) EEG 10-20 electrode montage map according to cortical activity (Section 4.2.1).

2) Evaluation of single chanel impact on EEG registration from scull (Section 4.2.2).
3) Design of Electroencephalographic helmet prototype (Section 4.2.3).

Future work:

1) EEG helmet prototype
2) Brain signal event detection

4.2.1 EEG 10-20 electrode montage map according to cortical activity

Before starting project on helmet design it was important to evaluate, which chanels are essential for brain computer interface and which electrode montage to choose for further experiments.

Signal recorded by single electrode (couple-primary and reference electrode) is dependent on the cortical activity of underlying cortical regions.

As a result of literature [4.2.1] review an EEG 10-20 electrode montage map according to cortical activity was developed (Figure 4.2.1).

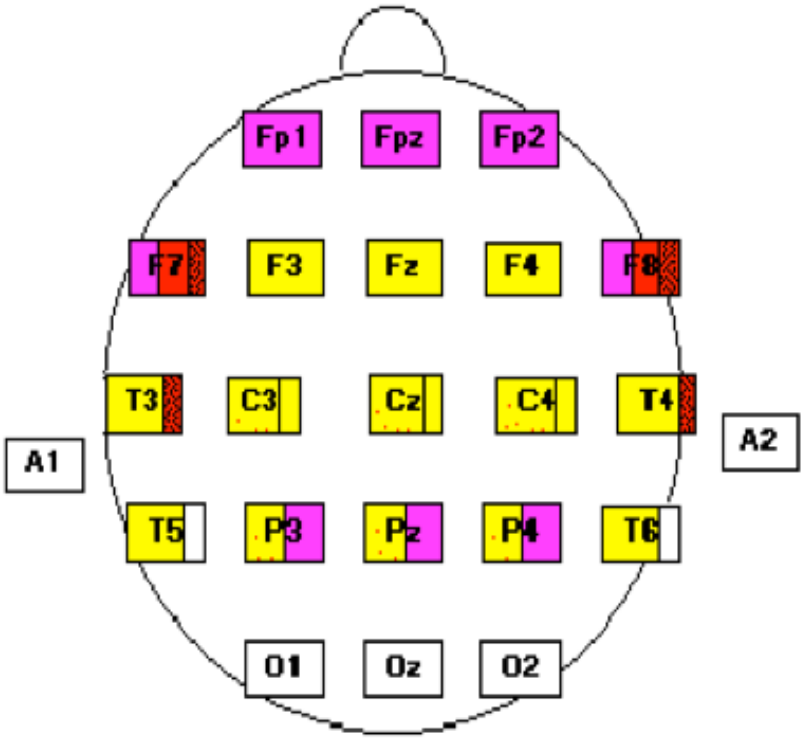

Fig. 4.2.1. Simplified figure of a map

Short explanation of highlighters:

Purple () - Cognitive activity – dicision making, knowlage, analysis, experience;

Yellow () - Movement generation;

Orange () - Sensory and positioning data;

Green () - Auditory reaction;

Blue () - Vision and visual memory;

Brown () - Emotions;

Red () - Broca's area.

4.2.2 Evaluation of single chanel impact on EEG registration from scull.

To evaluate single chanel impact it was necessary to evaluate impact of both – biological tissue and electrode. For this reason a scheme (Figure 4.2.2) resembling projection of pottentials on cortex and electrical properties of tissue and electrodes was designed [4.2.2].

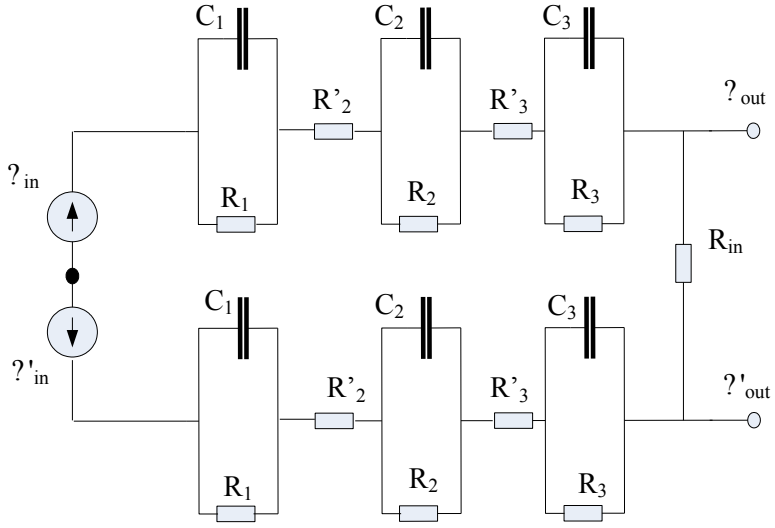

Fig. 4.2.2. This is a simplified figure of a scheme

In the next step, using real signal from free software EEGLab, a MatLab simulation was made.

4.2.3 Design of Electroencephalographic helmet prototype

Based on the 10-20 electrode montage map according to cortical activity, single chanel impact evaluation, anatomical characterictics of human head and analog products in the market project on EEG helmet design was started. Project is being made using SolidWorks2010 software.

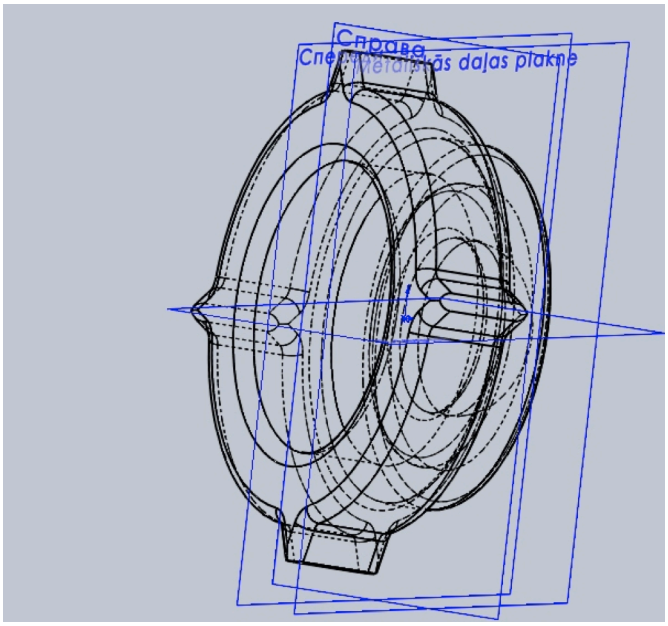

Fig. 4.2.3. Sketch of nod of reverse engineering project

4.3 Smart solutions in diagnostics and hindering the development of scoliosis based on biofeedback generated by sensor networks

In May of 2011 we launched a new research study in smart solutions in diagnostics and hindering the development of scoliosis based on biofeedback generated by sensor networks.

Scoliosis is a medical condition in which spine is curved form side to side and also vertebrae are rotated around spinal axis. It starts as some minor defect, but during rapid growth (usually teenage girls) the spinal defect is amplified. After the rapid growth cycle has ended, there are no effective means of correction short of surgery. The most common treatment is a hard material back brace which forbids the growing teenager from assuming the unwanted spinal posture, which would contribute to the growth of deformation. These braces must be worn for up to 23 hours a day and are both expensive and uncomfortable.

Usually patients are not aware that they are assuming unhealthy back position, and because of that we believe we can achieve the same adjustment effect as back braces just by providing smart feedback to the patient.

Fig. 4.3.1. Back brace used for scoliosis treatment

Our goal is to develop wearable smart device, which would replace these back braces. This device would consist of small sensor nodes embedded in clothing. By analyzing data from these embedded sensors we wish to provide feedback to the patient, which would allow him/her to adjust their posture accordingly. Also this device could be used for patient monitoring and long term statistics.

Benefits of such device would include easier and more cost effective treatment and monitoring of scoliosis patients. It will be especially beneficial to young teenagers, who also have social factors, such as peer ridicule, preventing them from correct brace use.

Our solution differs from similar devices in the sensor network approach – other solutions try to use small number of precise (and more expensive) sensors, but our plan is to gather and process data from larger network of partially redundant cheap sensor nodes.

The results obtained in this period:

1) Several existing methods of scoliosis detection were reviewed and also several new methods were proposed and analyzed (Section 4.3.1).
2) Developed a proof of concept scoliosis detection device with two sensors (Section 4.3.2).
3) Developed a prototype scoliosis detection device with twelve sensors (Section 4.3.3).
4) Developed software for data visualization gathered from the sensors of scoliosis detection device (Section 4.3.4).

Future work:

1) Gather real life data from static positions and measure them with acceptable precision.
2) Create next prototype – elastic shirt with wireless capabilities, containing sensor network, which can be worn all the time and does not restrict movement.

3) Gather and analyze real life dynamic data from both healthy people and diagnosed scoliosis patients.
4) Create algorithms for scoliotic posture detection
5) Develop software providing biofeedback to the scoliotic patient and also gathering data for later review by doctor.

4.3.1 Scoliosis detection methods – existing and proposed

As the problem of posture monitoring become more actual, many different methods are proposed for getting data about human spine position and producing biofeedback. The methods, which in many studies are used as the ground-truth reference for system testing, are optical 3D motion tracking systems. The biggest drawbacks of these kinds of systems are that they are expensive and limited to laboratory environment only. There are several low-cost approaches, which use tension sensors, strain gauges and other to get information about human spine position [4.3.1], [4.3.2]. In Austria University of Applied Sciences interesting approach was developed, by using office chair with built in tension sensors, to estimate sitting posture [4.3.3]. There are efforts made to develop portable electromagnetic system able to measure topographical features of the trunk [4.3.4].

As the advancement of microelectromechanical (MEMS) systems increase, there are many solutions proposed which uses inertial sensors such as accelerometers and gyroscopes. These kinds of sensors are available small in dimensions and weight, low-cost and low power, which makes them suitable for convenient, portable, battery-powered devices. Researchers in The Hong Kong Polytechnic University have developed device, which uses three sensor modules, to estimate the position of human spine [4.3.5]. There are several other similar approaches. For example [4.3.6], which offers real-time 3 dimensional measurement of spinal motion. Most of these systems use the phenomenon that in static conditions 3-axial accelerometer output is equal to gravitational vector, so it is possible to determine accelerometer position relative to the earth. In some systems there are additional gyroscopes or magnetometers to improve system accuracy in dynamic conditions. Most of these systems use small amount of sensors, so system resolution is limited.

We considered various sensor types. For our purpose we decided to base our approach on static position measurement with 3-axial MEMS accelerometers. These sensors are low-cost, small, lightweight and low power which makes possible to use multiple sensors in one wearable device to get high resolution for spine position measurements.

Our approach uses multiple 3-axial accelerometers arranged on spine surface in matrix style layout. By calculating each accelerometer's relative position to the ground, we can determine accelerometer mutual positions obtaining 3 dimensional model of human spine.

4.3.2 Proof of concept device

To validate our approach of using 3-axial accelerometers for calculation of relative angles to gravity vector we developed a proof of concept device consisting of two MEMS 3-axis low-power digital output accelerometers (LIS302DLH), Figure 4.3.3. Accelerometers have 16bit resolution on +/-2g acceleration. Data sampling from accelerometers is done by MCU (TI MSP430F2274) through SPI protocol and data is transferred from MCU to PC through UART connection for analysis.

We tested this device in a series of motions and static positions, and concluded, that the approach is sound and proceeded to the next step of prototype development.

4.3.3 Prototype scoliosis detection device

For our first prototype we chose a grid configuration of 12 accelerometers in a three by four arrangement (Figure 4.3.2).

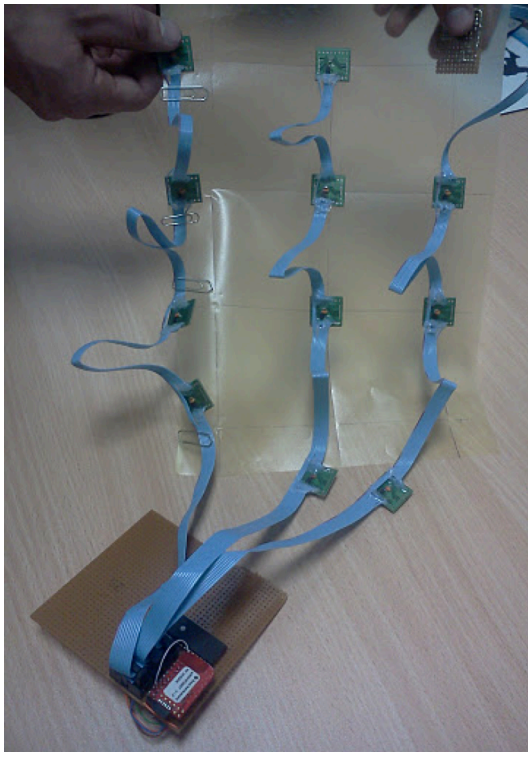

Fig. 4.3.2. Prototype device with 12 accelerometers

Each accelerometer node consists of a custom made board (Figure 4.3.3) holding a MEMS 3-axis low-power digital output accelerometer (LIS331DLH) and two capacitors. Accelerometers have 16bit resolution on +-2g acceleration and built in 50Hz low pass filter.

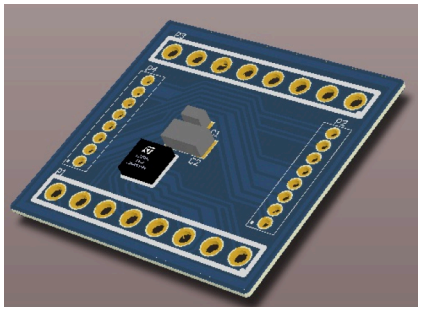

Fig. 4.3.3. Custom board for each accelerometer node

Data sampling from accelerometers is done by MCU (TI MSP430F2274) through SPI protocol. High-speed 4-16 line demultiplexer is used for twelve SPI chip select lines.

Data are transferred from MCU to PC through UART connection for analysis and data real time visualization.

4.3.4 Data gathering and visualization software

A software solution was developed for data gathering and visualization. System was developed in Mono/.NET C# and OpenGL. The main benefit of these platforms is independence of computer operating system – the same source code works on both MS Windows and any Linux distribution with Mono runtime.

The software consists of:

- Serial communication module – responsible for fast and reliable serial communication with the MCU.
- Data layer, which provides a safe data communication protocol between MCU and PC over the basic serial communication.
- Data objects, which contain:
  - Calibration data for each accelerometer
  - Raw accelerometer data as well as calibration adjusted data
  - Low pass filter for data
  - Calculated rotation angles form accelerometer data
  - Location of each accelerometer in the grid
  - Calculated position of each accelerometer based on its rotation and place in the grid

Visualization module, which can visualize acquired accelerometer network data in real time (Figure 4.3.4)

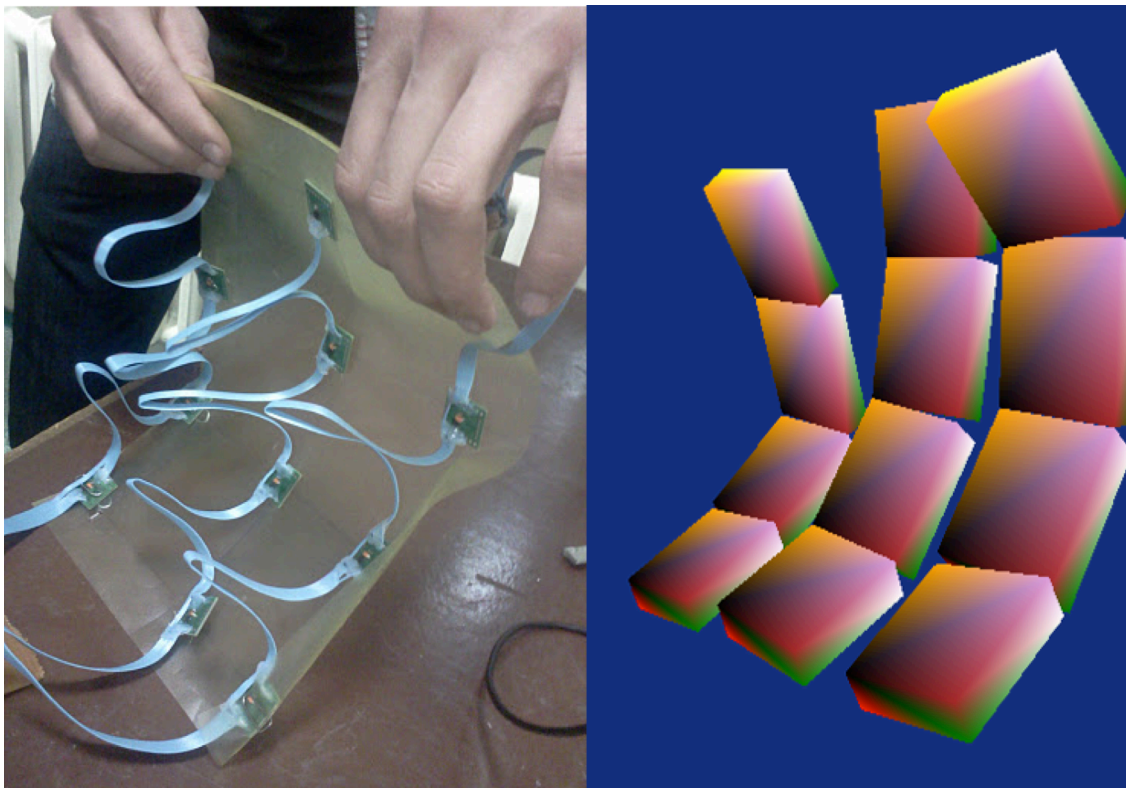

Fig. 4.3.4. Prototype device side by side with the matching visualization

References

[4.1.1] M.Pudzs, M.Greitans, R.Fuksis. "Generalized Complex 2D Matched Filtering for Local Regular Line-Like Feature Detection". 19th European Signal Processing Conference (EUSIPCO 2011), Barcelona, Spain, August 29 - September 2, 2011.

[4.1.2] M.Pudzs, M.Greitans, R.Fuksis. "Complex 2D Matched Filtering Without Halo Artifacts". 18th International Conference on Systems, Signals and Image Processing, IWSSIP 2011, Sarajevo, Bosnia and Herzegovina, June 16-18, 2011, pp. 109-112.

[4.2.1] Marc Heiser, Marco Iacoboni, Fumiko Maeda, The essential role of Broca's area in imitation, March 2003

[4.2.2] Webster J.G. Medical Instrumentation: application and design. Fourth Edition. – New Jersey: John Wiley & Sons, Inc., 2009. – 675 p.

[4.3.1] N. AZRIN, H. RUBIN, F. O'BRIEN, T. AYLLON, D. ROLL. BEHAVIORAL ENGINEERING: POSTURAL CONTROL BY A PORTABLE OPERANT APPARATUS. JOURNAL OF APPLIED BEHAVIOR ANALYSIS. 1968, p. 99-108.

[4.3.2] Gabriel J. Donatell, David W. Meister, Jeremy R. O'Brien, John S. Thurlow, John G. Webster. A Simple Device to Monitor Flexion and Lateral

Bending of the Lumbar Spine. IEEE TRANSACTIONS ON NEURAL SYSTEMS AND REHABILITATION ENGINEERING, VOL. 13, NO. 1, MARCH 2005

[4.3.3] Andreas Schrempf, Gerold Schossleitner, Thomas Minarik. PostureCare - Towards a novel system for posture monitoring and guidance. Upper Austria University of Applied Sciences, School of Informatics, Communications and Media, Softwarepark 11, A-4232 Hagenberg, Austria

[4.3.4] Edmond Lou, Nelson G. Durdle, V. James Raso, and Doug L. Hill. A Low-Power Posture Measurement System for the Treatment of Scoliosis. IEEE TRANSACTIONS ON INSTRUMENTATION AND MEASUREMENT, VOL. 49, NO. 1, FEBRUARY 2000

[4.3.5] Wai-Yin Wong, Man-Sang Wong. Measurement of Postural Change in Trunk Movements Using Three Sensor Modules. IEEE TRANSACTIONS ON INSTRUMENTATION AND MEASUREMENT, VOL. 58, NO. 8, AUGUST 2009 2737

[4.3.6] Christina Goodvin, Edward J. Park, Kevin Huang, Kelly Sakaki. Development of a real-time three-dimensional spinal motion measurement system for clinical practice. Med Bio Eng Comput (2006) 44:1061–1075

5 Uz rotācijas leņķiem balstītas vispārinātas signālu analīzes metožu attīstība, algoritmu realizācija, moduļu izstrāde un pielietojamības izpēte (t.sk. materiālzinātnē)

5.1 2D ātrie ortogonālie pārveidojumi

2011. g. tika turpināti pētījumi, kas ir saistīti ar jaunu 2D ortogonālu pārveidojumu sintēzi un tādu 2D pārveidojumu sintēzi, kuru bāzes funkcijām līdzīgi kā veivletiem piemīt kompaktums.

5.1.1 Reālo 2D pārveidojumu sintēzes algoritms

2D tiešo pārveidojumu definē kā:

$$\mathbf{Y} = (\mathbf{H} \cdot (\mathbf{H} \cdot \mathbf{X})^T)^T, \tag{5.1}$$

kur **X** – attēla elementu matrica, **Y** – attēla spektra matrica, bet **H** – ortogonāla pārveidojuma matrica. Savukār, inverso pārveidojumu var atrast kā:

$$\mathbf{X} = (\mathbf{H}^T \cdot (\mathbf{H}^T \cdot \mathbf{Y})^T)^T. \tag{5.2}$$

Pārveidojuma matricas pamatā ir retinātu matricu reizinājums

$$\mathbf{H} = \mathbf{P}_n \cdot \mathbf{B}_n(\varphi_n) \cdot \ldots \cdot \mathbf{P}_2 \cdot \mathbf{B}(\varphi_2) \cdot \mathbf{P}_1 \cdot \mathbf{B}(\varphi_1). \tag{5.3}$$

kur $\mathbf{P_k}$ – permutāciju matrica, $\mathbf{B}(\varphi_k)$ – retinātā blokveida ortonormētā matrica, kura pie N = 8 un k = 1 izskatās sekojoši:

$$\mathbf{B}(\phi_1) = \begin{bmatrix} s_1 & c_1 & 0 & 0 & 0 & 0 & 0 & 0 \\ c_1 & -s_1 & 0 & 0 & 0 & 0 & 0 & 0 \\ 0 & 0 & s_1 & c_1 & 0 & 0 & 0 & 0 \\ 0 & 0 & c_1 & -s_1 & 0 & 0 & 0 & 0 \\ 0 & 0 & 0 & 0 & s_1 & c_1 & 0 & 0 \\ 0 & 0 & 0 & 0 & c_1 & -s_1 & 0 & 0 \\ 0 & 0 & 0 & 0 & 0 & 0 & s_1 & c_1 \\ 0 & 0 & 0 & 0 & 0 & 0 & c_1 & -s_1 \end{bmatrix}, \tag{5.4}$$

kur $s_1=\sin(\phi_1)$, $c_1=\cos(\phi_1)$. Kāpņveida ortonormētās matricas pamatā ir elementārā rotācijas matrica:

$$\mathbf{R} = \begin{bmatrix} s_1 & c_1 \\ c_1 & -s_1 \end{bmatrix}. \tag{5.5}$$

Ja katrā no retinātajām blokveida ortonortmētajām rotācijas matricām tiek izmantots tikai viens leņķis (līdzīgi kā piemērā (5.4)), tad šie pārveidojumi tiek dēvēti par CRAIM (Constant Rotation Angle in Matrix Orthogonal Transform) tipa pārveidojumiem.

Savukārt, pārveidojumu, kuri atgādina Hāra pārveidojumus, nosaukumiem tiek pievienots piedēklis HT (Constant Rotation Angle in Matrix Transform) – CRAIM-HT.

5.1.1.1 Reālo 2D pārveidojumu klases

Dažas no iespējamajām pārveidojumu klasēm ir apkopotas nākamajā tabulā

Transform		Komentāri
RABOT – Rotation Angle Based OT	$\phi_{ij} = \phi_{ij}$	Katrā no rotācijām leņķi ir atšķirīgi
CRAOT – Constant Rotation Angle OT	$\phi_{ij} = \phi$	Visi leņķi ir vienādi
CRAIMOT – Constant Rotation Angle Inside Matrix OT	$\phi_{ij} = \phi_i$	Vienas faktorizētās matricas ietvaros **B** visi rotācijas leņķi ir vienādi
CRMOT – Constant Rotation Matrix OT	$\phi_{ij} = \phi_j$	visas **B** matricas ir vienādas
RAHT – Rotation Angle-based Haar-like Transforms	-	sk. iepriekšējo atskaiti

5.1.2 2D komplekso pārveidojumu sintēzes algoritms

Sintezējot kompleksos pārveidojumus, elementārās rotācijas matricas (5.5) vietā tiek izmantota elementārā vispārinātā Jakobi (*Jacobi*) rotācijas matrica:

$$\mathbf{T}(\phi_k,\psi_k,\gamma_k) = \begin{Vmatrix} T_{11k} & T_{12k} \\ T_{21k} & T_{22k} \end{Vmatrix} = \begin{bmatrix} \sin\phi_k \cdot e^{j\psi_k} & \cos\phi_k \cdot e^{-j\gamma_k} \\ \cos\phi_k \cdot e^{j\gamma_k} & -\sin\phi_k \cdot e^{-j\psi_k} \end{bmatrix} \qquad \textbf{(5.6)}$$

un matricas (5.4) vietā tiek formēta unitāra matrica

$$\mathbf{B}(\phi_k,\psi_k,\gamma_k) = \begin{bmatrix} T_{11k} & T_{12k} & 0 & 0 & 0 & 0 & 0 & 0 \\ T_{21k} & T_{22k} & 0 & 0 & 0 & 0 & 0 & 0 \\ 0 & 0 & T_{11k} & T_{12k} & 0 & 0 & 0 & 0 \\ 0 & 0 & T_{21k} & T_{22k} & 0 & 0 & 0 & 0 \\ 0 & 0 & 0 & 0 & T_{11k} & T_{12k} & 0 & 0 \\ 0 & 0 & 0 & 0 & T_{21k} & T_{22k} & 0 & 0 \\ 0 & 0 & 0 & 0 & 0 & 0 & T_{11k} & T_{12k} \\ 0 & 0 & 0 & 0 & 0 & 0 & T_{21k} & T_{22k} \end{bmatrix}. \qquad \textbf{(5.7)}$$

Sintezējot unitāros 2D pārveidojumus, ir jāpatur prātā, ka transponējot kompleksu matricas iegūst Ermita matricu (*Hermitian*).

5.1.3 Reālo ortonormālo vispārināto 2D BF izskats

Ja leņķu matrica (sk. [5.1.1]) ir definēta konkrēti kā

$$\boldsymbol{\varphi} = \begin{vmatrix} \pi/6 & \pi/6 & \pi/6 \\ \pi/6 & \pi/6 & \pi/4 \\ \pi/6 & \pi/4 & \pi/4 \\ \pi/6 & \pi/4 & \pi/4 \end{vmatrix}, \qquad \textit{(5.8)}$$

mēs iegūstam sekojošu bāzes funkciju komplektu:

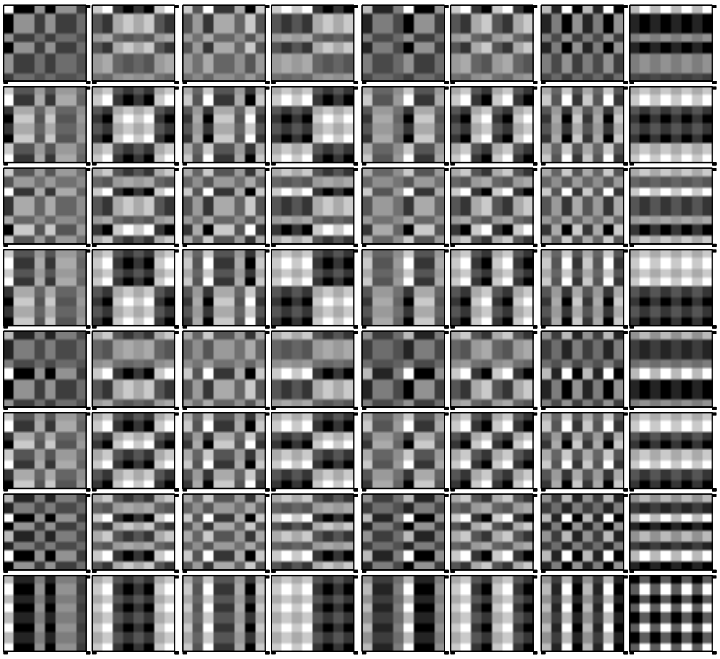

Att. 5.1. Pilna 2D bāzes funkciju kopa rotācijas leņķiem, kas ir definēti ar matricu (5.8)

Hārveidīgajiem pārveidojumiem leņķu matricai ir trīsstūrveida forma un matricas apakšējā daļa ir aizpildīta ar nulles leņķiem:

$$\boldsymbol{\varphi} = \begin{vmatrix} \pi/6 & \pi/6 & \pi/6 \\ \pi/6 & \pi/6 & 0 \\ \pi/6 & 0 & 0 \\ \pi/6 & 0 & 0 \end{vmatrix}. \qquad \textit{(5.9)}$$

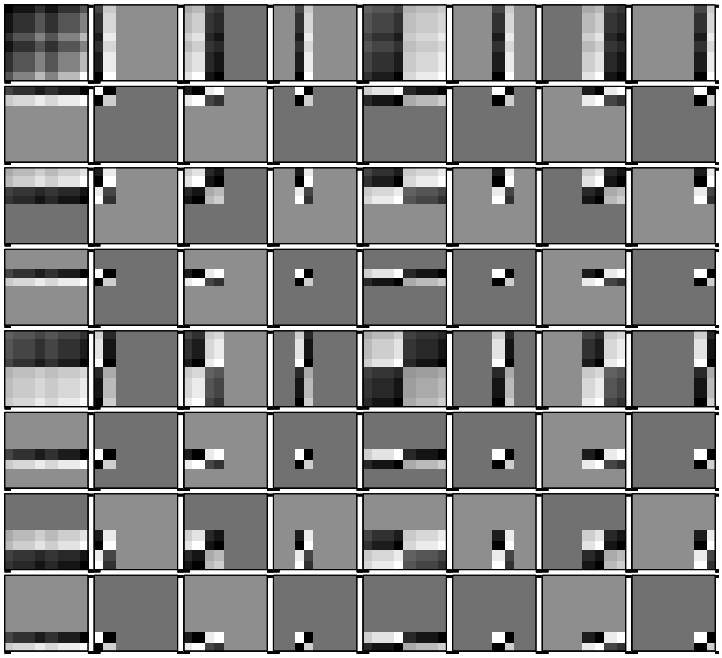

Att. 5.2. Pilna 2D bāzes funkciju kopa rotācijas leņķiem, kas ir definēti ar matricu (5.9)

Mainot rotācijas leņķus mēs varam iegūt bezgalīgi daudz dažādu veidolu bāzes funkciju.

5.1.4 2D pārveidojumu ātrie aprēķina algoritmi

Ņemot vērā izteiksmi (5.1), tiešais reālais pārveidojums ieejas attēla matricai **X** izskatās sekojoši:

$$\mathbf{Y} = (\mathbf{B}_l \cdot \ldots \cdot \mathbf{B}_2 \cdot \mathbf{B}_1 \cdot (\mathbf{B}_l \cdot \ldots \cdot \mathbf{B}_2 \cdot \mathbf{B}_1 \cdot \mathbf{X})^T)^T. \qquad \textit{(5.10)}$$

Savukārt inversais pārveidojums ļauj atjaunot oriģinālo attēlu no spektra:

$$\mathbf{X} = ((\mathbf{B}_l \cdot \ldots \cdot \mathbf{B}_2 \cdot \mathbf{B}_1)^T \cdot ((\mathbf{B}_l \cdot \ldots \cdot \mathbf{B}_2 \cdot \mathbf{B}_1)^T \cdot \mathbf{Y})^T)^T. \qquad \textit{(5.11)}$$

kur $()^T$ – transponētā matrica (vai kompleksajiem pārveidojumiem Ermita matrica). Kompleksajiem pārveidojumiem katra leņķa φ_k vietā tiek izmantoti atbilstoši trīs leņķi - ϕ_k, ψ_k, γ_k.

Tā kā pārveidojumu (5.10) un (5.11) faktorizētajās formās tiek izmantotas retinātās matricas, tad pārveidojumiem ir nepieciešams mazāks operāciju skaits nekā tad, ja pārveidojuma aprēķinam tiek pielietota pilnā pārveidojuma matrica **H**.

5.1.4.1 Operāciju skaits

Reizināšanas (*mult*), summēšanas (*sum*) un kopējo (*op*) operāciju ātrajam algoritmam var izteikt kā:

$$\begin{aligned} n_{mult\,2DFT} &= 2 \cdot l \cdot 4 \cdot N \cdot (N/2) = 4 \cdot l \cdot N^2 \le 4 \cdot n \cdot N^2 \\ n_{sum\,2DFT} &= 2 \cdot l \cdot 2 \cdot N \cdot (N/2) = 2 \cdot l \cdot N^2 \le 2 \cdot n \cdot N^2 . \\ n_{op\,2DFT} &= 6 \cdot l \cdot N^2 \le 6 \cdot \log_2(N) \cdot N^2 \end{aligned} \qquad \textbf{(5.12)}$$

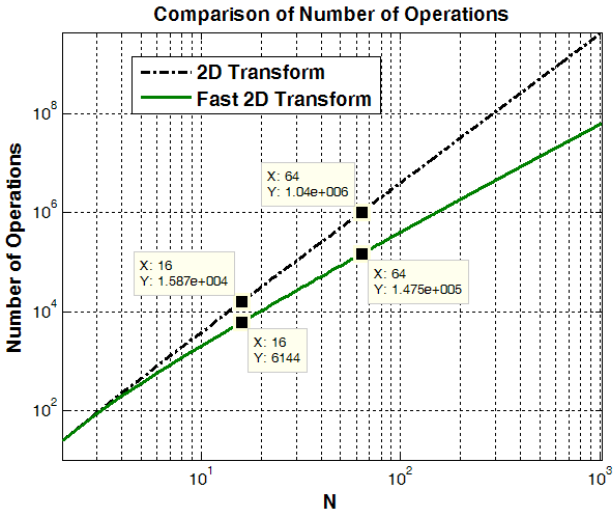

Att. 5.3. Operāciju skaits parastajam un ātrajam pārveidojumiem

5.2 Uz rotācijas leņķiem balstītu signālu ciparapstrādes ierīču moduļu izstrāde un mikrominiaturizācija (ASIC/FPGA)

Moduļu izstrāde un mikrominiaturizācija 2011.g. ir noritējusi vairākos virzienos. Šeit aplūkosim tikai galveno pienesumu VPP.

5.2.1 Komplekso pārveidojumu FPGA realizācijas automatizācijas līdzekļi

Kā jau minēts 2010.g. atskaites punktā 5.2.1., automatizācijas sistēmas nepieciešamība ir saistīta ar iespējamo milzīgo skaitu unitāro pārveidojumu un neiespējamību pārskatāmā laikā manuāli novērtēt paterētos ASIC/FPGA resursus. Tā, piemēram, vispārinātās Jakobi rotāciju dažādība var sasniegt vairākus tūkstošus. Automatizācijas līdzekļu izveides problēmas nepieciešamība detalizētāk ir aplūkotas publikācijā [5.2.1], bet publikācijā [5.2.2] ir aprakstīta reāli izveidotā sistēma **EGURIT** (**E**lementary **G**eneralized **U**nitary **R**otation **I**mplementation **T**ool - Elementārās Vispārinātās Unitārās Rotācijas Īstenošanas Rīks). Vienkāršoti rīka būtība ir izsakāma ar sekojošu ķēdīti:

Formula(s) ➔ VHDL kods ➔ Resursu novērtējums

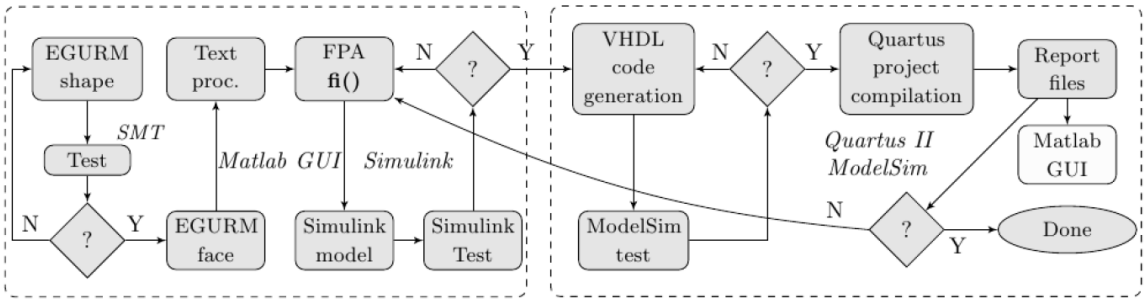

Att. 5.4. Vienkāršota automatizētā VHDL koda sintēzes EGURIT sistēmas blokshēma

Automatizācija tiek veikta izmantojot *Matlab/Simulink*, *Altera Quartus II* un *Mentor Graphics ModelSim* programmas. Minētās programmas tiek lietotas sekojošu uzdevumu veikšanai:

- *MatLab* – Automatizācijas vadība, rotācijas izteiksmju unitaritātes pārbaude, to sadalīšana reālajā un imaginārajā daļās, izmantojot Symbolic Math Toolbox(SMT). Rezultātu iegūšana izmantojot peldošā punkta aritmētiku (double precision) un iegūto izteiksmju pārveidošana fiksētā punkta aritmētikā ar **fi()** objektu.
- *Simulink* – Sistēmas simulēšana fiksētā punkta aritmētikā, VHDL koda ģenerēšana izmantojot *HDL coder*,
- *ModelSim* – VHDL koda simulēšana,
- *Quartus II* – VHDL koda kompilācija izvēlētajai FPGA mikroshēmai, FPGA programmēšana.

5.2.1.1 EGURIT uzbūves īss apraksts

5.2.1.1.1 Pārlūks Rotation Matrix Viewer

EGURIT no lietotāja viedokļa ir veidots kā saskarsņu (GUI) komplekss, daļa no kurām ir redzamas nākamajos attēlos. Pārlūkā *Rotation Matrix Viewer* (skat. Attēlu 5.5) notiek:

- Rotācijas matricu struktūru (shape) izvēle
- Rotācijas matricu vienkāršojumu (face) izvēle
- Vienkāršojumu parametru kombināciju izvēle
- Simbolisko izteiksmju LaTeX attēlojums

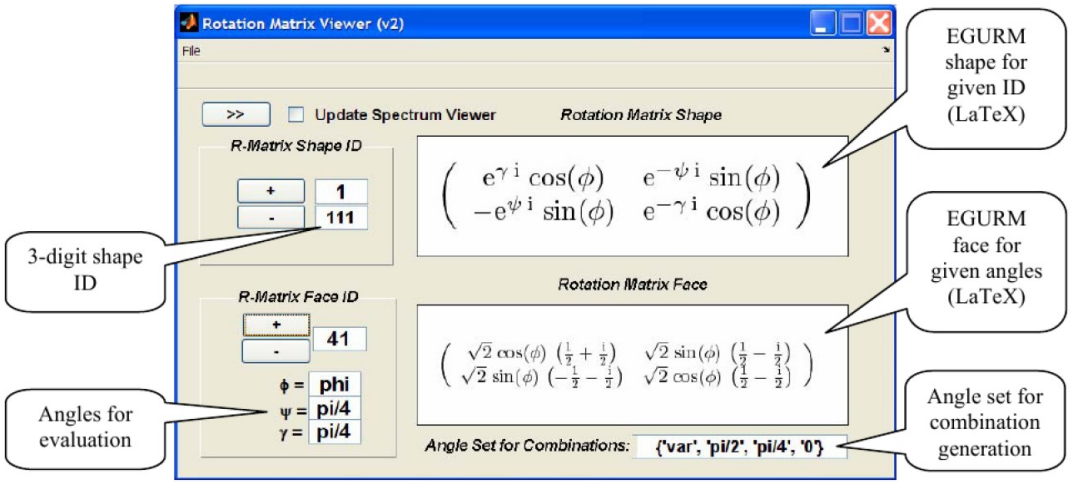

Att. 5.5. *Rotation Matrix Viewer* dialoglogs

5.2.1.1.2 Pārlūks Spectrum Expressions

Pārlūkā *Spectrum Expressions* (skat nākamo attēlu) notiek

- Elementārā spektra kalkulācijas izteiksmju LaTeX attēlojums
- Elementārā spektra koeficienta izvēle un tā aprēķināšanas ASCII izteiksmes
- Automātiska/manuāla signālu vārda garuma uzstādīšana
- *Embedded MatLab Function* koda ģenerācija

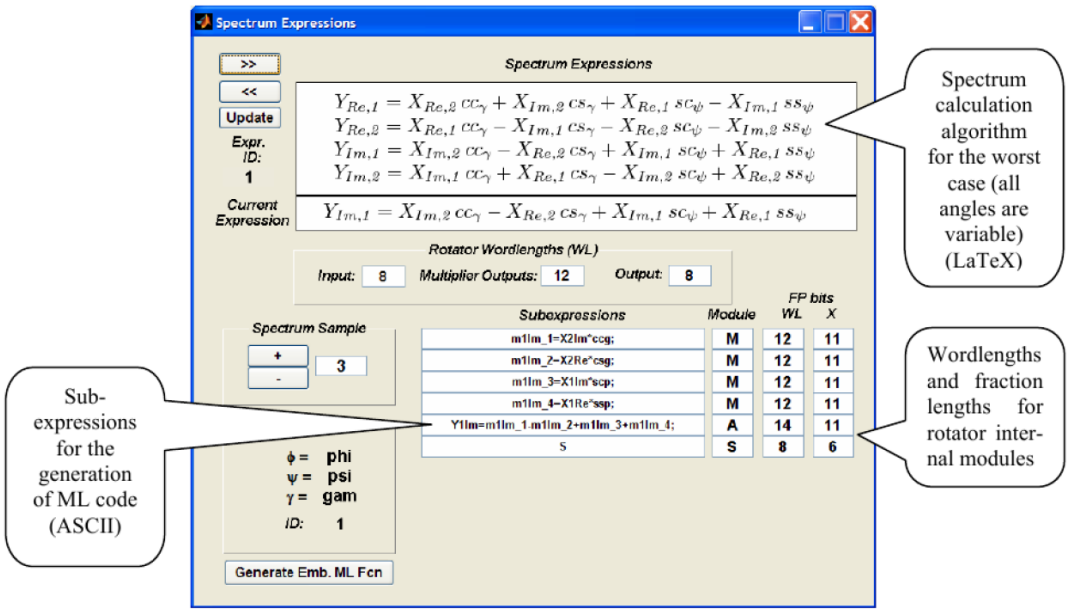

Att. 5.6. *Spectrum Expressions* dialoglogs

5.2.1.1.3 Simulink modelis

Uzģenerēto *Embedded MatLab* funkciju izmanto Attēlā 5.7 redzamais Simulink modelis.

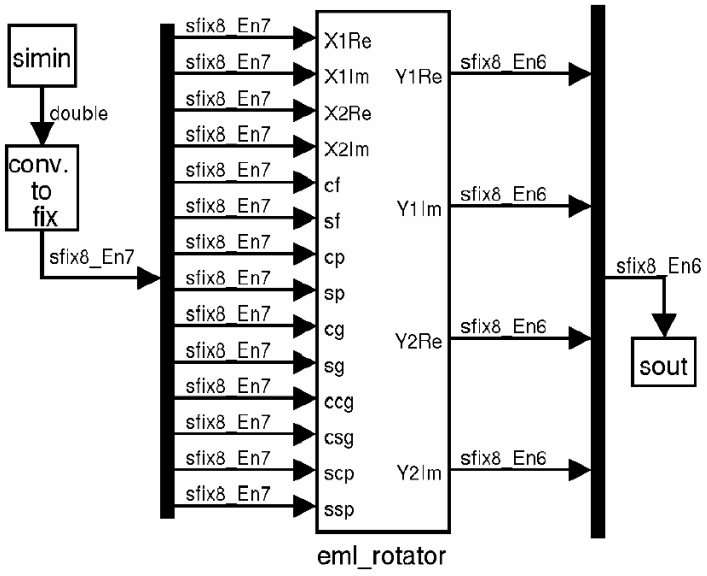

Att. 5.7. EGU-rotatora *Simulink* modeļa piemērs VHDL koda ģenerēšanai

5.2.1.1.4 HDL kodera konfigurācija

HDLCoderGUI, kura saskarsne ir redzama Attēlā 5.8, īsteno

- Peldošā punkta un Simulink testu
- VHDL koda, *Quartus II* un *ModelSim* skriptu ģenerāciju
- *Quartus II* projekta apakškatalogu sagatavošanu
- *ModelSim* testu un rezultātu salīdzināšanu ar Simulink rezultātiem
- *Quartus II* kompilāciju
- Rezultātu attēlošanu

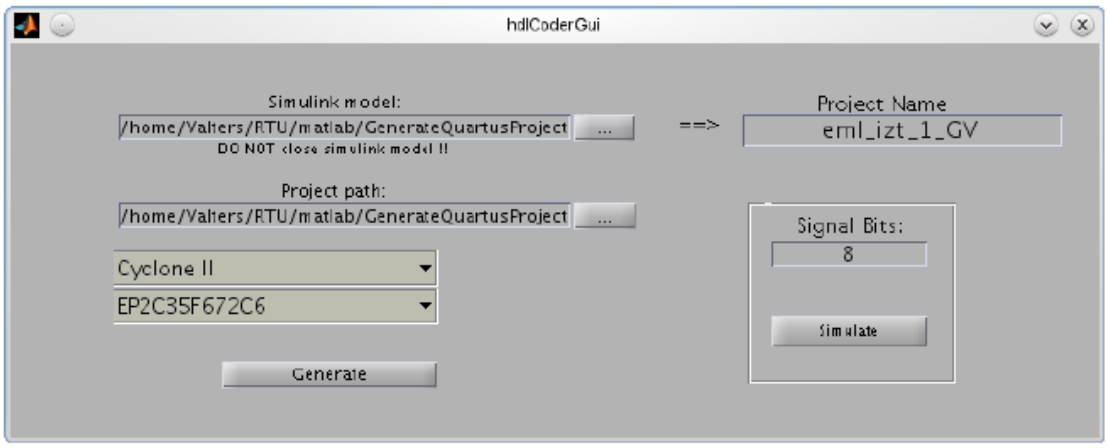

Att. 5.8. HDL Coder GUI dialoglogs

5.2.1.2 Perspektīva

Izstrādātā sistēma ir relatīvi vienkārši adaptējama arī citām izstrādes platformām (*Xilinx*, *Synopsys*), kurām ir iespējama t.s. skriptēšana (*scripting*).

Pašreiz izstrādes stadijā atrodas sistēma, kas realizē unitāro pārveidojumu VHDL kodu sintēzi – UNITIT (**UNI**tary **T**ransform **I**mplementation **T**ool – Unitāru Pārveidojumu Īstenošanas Rīks).

5.2.2 Eksperimentālais attēlu analizators-sintezators

HIMANSY (**H**ardware **IM**age **AN**alyzer **SY**ntesizer – Aparatūriskais Attēlu Analizators-Sintezators). Eksperimentālā ierīce ir izstrādāts uz Terasic FPGA izstrādes rīka DE2/DE3 bāzes, izmantojot gan skārienjūtīgu ekrānu, gan 5 Mps kameru.

Modulis ir veidots kā VIMANSY (virtuālā ierīce – skat. Attēlu 5.4.) aparatūriskais analogs un ir paredzēts attēlu analīzes/sintēzes/filtrācijas/kompresijas algoritmu aparatūriskajai prototipēšanai.

Eksperimentālā maketa vienkāršota blokshēma ir redzama nākamajā attēlā.

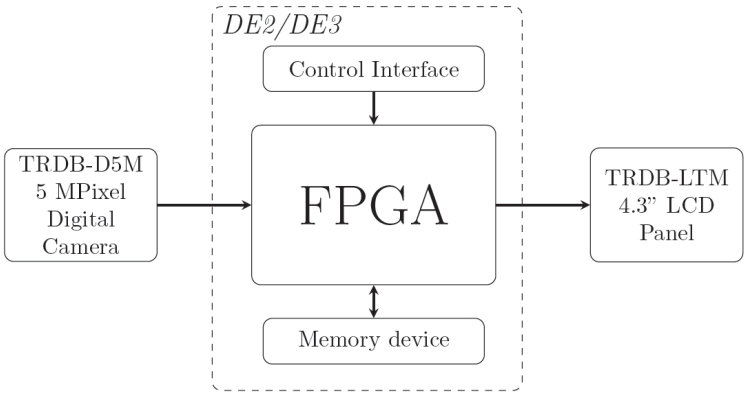

Att. 5.9. HIMANSY moduļa vienkāršota blokshēma

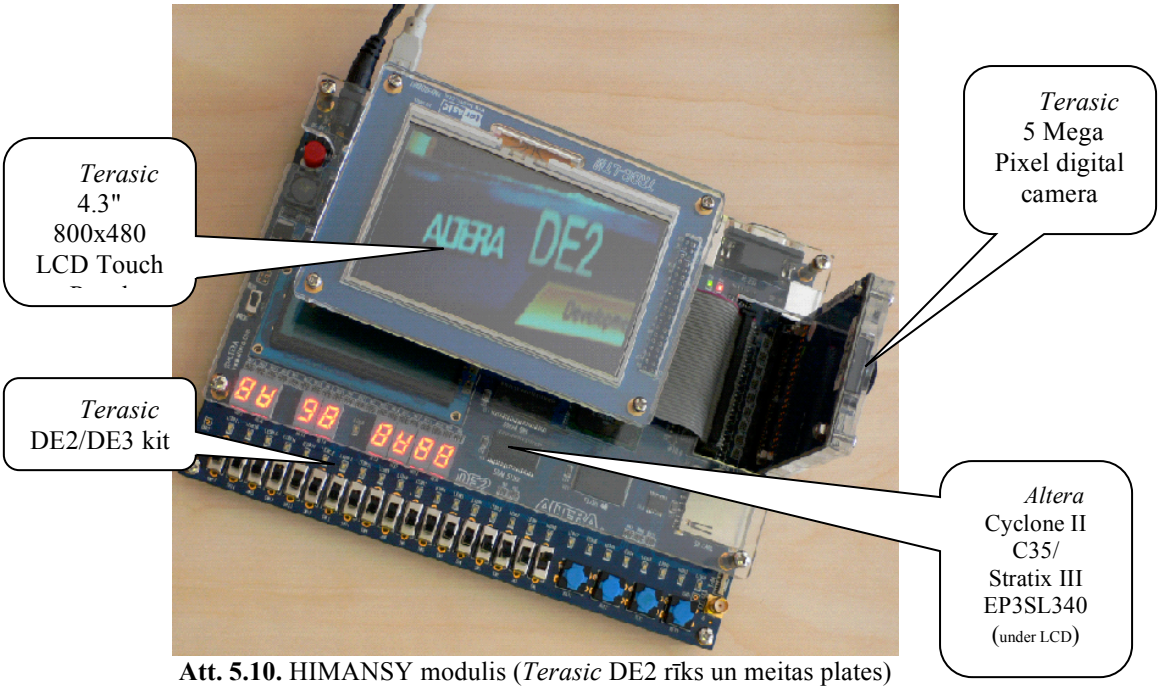

Att. 5.10. HIMANSY modulis (*Terasic* DE2 rīks un meitas plates)

5.3 Uz Vispārinātās Ortogonālās Nesinusoidālās Funkcijdales balstītas datu pārraides sistēmas pilnveidošana

2011.g turpinājās 2009.g. aizsāktā (iepriekšējā VPP) GONDM (Generalized Orthogonal Nonsinusoidal Division Multiplexing) datu pārraides sistēmas izstrāde. Ir iegūti vairāki būtiski rezultāti.

5.3.1 Galvenie rezultāti

Ir veikta GONDM un OFDM salīdzināšana dažādiem pārveidojumiem [5.3.1] un konstatēts, ka:

- PAPR (Peak to Average Power Ratio) koeficients CRAIMOT pārveidojuma gadījumā ir gandrīz 2 reizes mazāks nekā Adamāra un FFT pārveidojumiem,
- klasiskā kanāla ekvalizācijas procedūra ir derīga tikai FFT gadījumā.

Publikācijā [5.3.2] ir nodemonstrēts, ka

- arī fī-funkcijām arī ir iespējama sakaru kanāla ekvalizācija, izmantojot SVD (Singular Value Decomposition),
- ekvalizācijas kvalitāte ir būtiski atkarīga no kanāla novērtējuma,
- kanāla novērtēšana, kas balstīta uz LMS sistēmas identifikācijas dod gandrīz perfketu kanāla novērtējumu laika apgabalā,
- LMS un SVD kombinācijas balstīta kanāla novērtēšana dod ļoti labus ekvalizācijas rezultātus.

5.4 Izstrādātie funkciju/programmmu moduļi MATLAB/Simulink bibliotekām "Phi-FunctionsToolbox/Blockset"

2011.g. saistībā ar "izgudrotajiem" pārveidojumiem tika/tiek izstrādātas vairākas interaktīvas MATLAB programmas, kas ļauj darboties ar iepriekš aprakstītajiem 2D pārveidojumiem. Šeit aplūkosim vienu no tām.

5.4.1 Virtuālais 2D attēlu analizators-sintezators

5.4.1.1 Analizatora-sintezatora vispārējā uzbūve

VIMANSY (**V**irtual **IM**age **AN**alyzer **SY**ntesizer – Virtuālais Attēlu Analizators-Sintezators). Virtuālā ierīce ir izstrādāta MATLAB vidē un pašreiz ir paredzēta diviem galvenajiem pielietojumiem:

- lai definētu, izrēķinātu un attēlotu 2D bāzes funkciju kopu
- lai veiktu ātros 2D tiešos un inversos RABOT (RABFOT) pārveidojumus attēliem

VIMANSY, kurš ietver sevī galveno un ārējo logu, veic

- bāzes funkciju izskata vizualizāciju,
- bāzes funkciju parametru (leņķu) ievadu un vizualizāciju,
- analizējamo attēlu importu un sintezēto attēlu eksportu,
- interakciju ar atbilstošo *Simulink* modeli

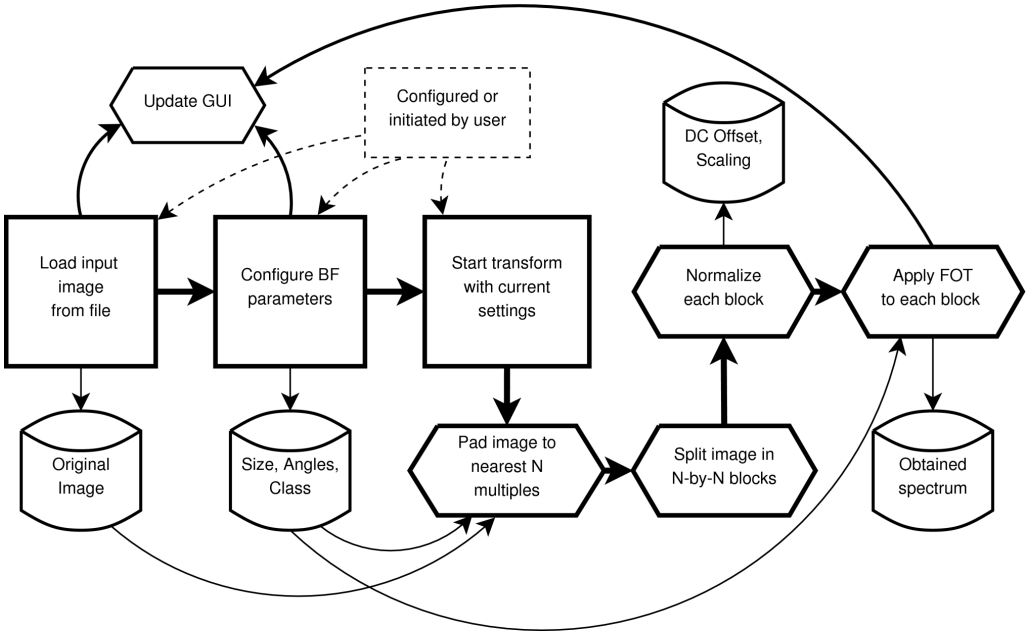

Att. 5.11. Attēlu analizatora-sintezatora vienkāršota uzbūves blokshēma

5.4.1.2 VIMANSY īss apraksts

VIMANSY pašreiz atļauj izmantot šādas iebūvētās pārveidojumu klases:

- CRAFOT – Constant Rotation Angle Fast Orthogonal Transform,
- CRAIMFOT – Constant Rotation Angle In Matrix Fast Orthogonal Transform,
- CRA-HT – Constant Rotation Angle Haar-Like transform,
- CRAIM-HT -Constant Rotation Angle In Matrix Haar-Like transform,
- CRM-45 – A modified Constant Rotation Angle In Matrix Haar-Like transform.

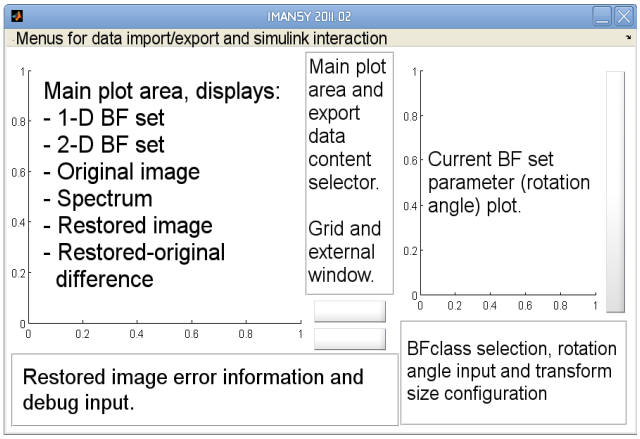

Att. 5.12. VIMANSY galvenā dialogloga struktūra

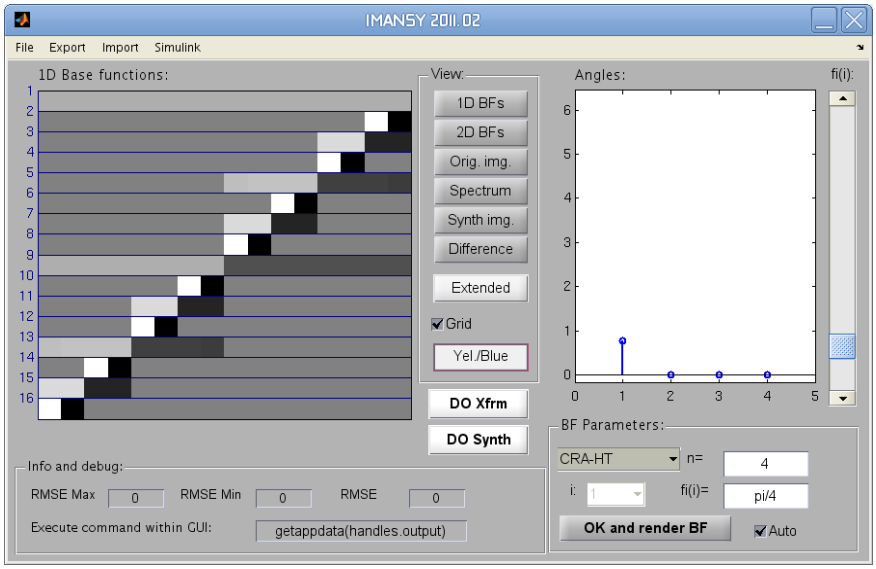

Att. 5.13. VIMANSY galvenais dialoglogs. Piemērs ir dots 1-D Hāra matric (pikselu spilgtums reprezentē matricas elementa vērtību). N=16, CRA-HT BF klase pie φ=[π/4, π/4, π/4, π/4]. Matricas rindas nav šķirotas

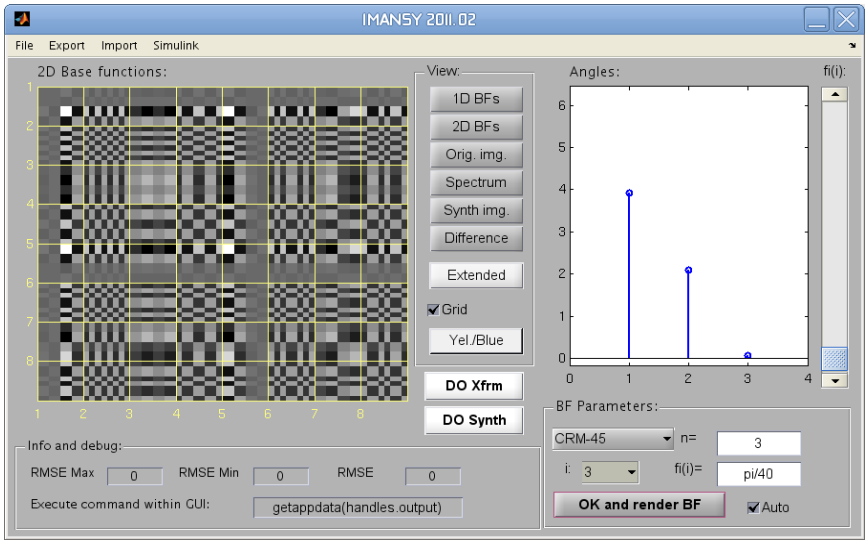

Att. 5.14. Galvenais VIMANSY dialoglogs. 2-D bāzes funkciju kopa. N=8, CRAIM-HT klase ar φ=[5π/4, 2π/3, π/40]

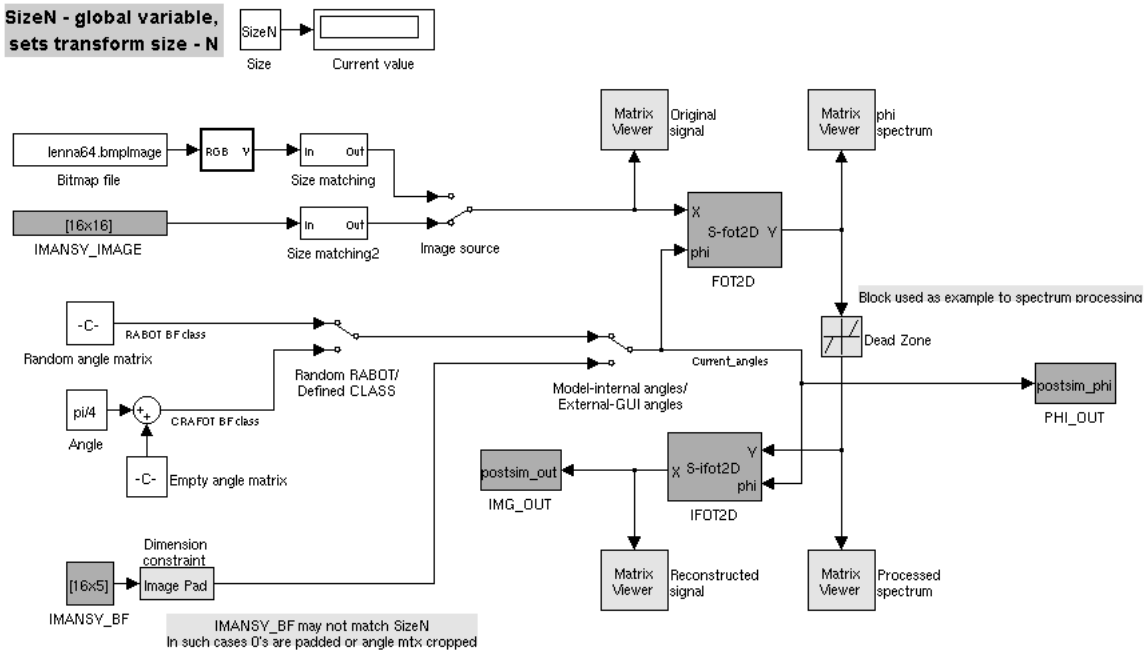

Att. 5.15. Izveidotais VIMANSY Simulink modelis.

5.4.2 Atsauces

[5.1.1.] Misans P., Derums U. Introduction into the novel two dimensional discrete orthogonal transforms based on rotation angles // Presented at the 12th International Conference Electronics, May 18-20, Kaunas, Lithuania, Proc. Electronics and Electrical Engineering. - Kaunas: Technologija, 2011, No. 6 (112), pp.95-100.

[5.1.2.] G. Valters, U. Derums, K. Osmanis, P. Misans, "Experimental Image Analyzer-Synthesizer based on the Novel Discrete Orthogonal Transforms", presented at the 15th International Conference Electronics, May 17-19, 2011, Kaunas, Lithuania. Submitted for publication in proc. Electronics and Electrical Engineering. - Kaunas: Technologija, 2012, No. X (112), 6 pages.

[5.2.1.] G. Valters, P. Misans, ”Automation of FPGA Implementation of Unitary Transforms Based on Elementary Generalized Unitary Rotation”, presented at the RTU 52th International Scientific Conference, section on Electronics and Telecommunications, Riga, Oct. 13-14, 2011, Latvia, submitted for publication Scientific Proc. of Riga Technical University, Telecommunications and Electronics, Riga, RTU, vol. 11, Dec., 2011, 6 pages.

[5.2.2.] G. Valters, ”Initial version of MATLAB/ SIMULINK based tool for VHDL code generation and FPGA implementation of Elementary Generalized Unitary Rotation”, presented at 29th IEEE Norchip 2011 Conference, Nov. 14-15, Lund, Sweden.

[5.2.3.] G. Valters, "Parametriskajiem ortogonālajiem pārveidojumiem atbilstošu signālu ciparapstrādes eksperimentālu ierīču īstenošana programmējamajos loģiskajos masīvos", Kopsavilkums par tematiski vienotu publikāciju kopu, ISBN 978-9934-10-261-5, Rīga, 2011.

[5.2.4.] G. Valters, U. Derums, K. Osmanis, P. Misans, "Experimental Image Analyzer-Synthesizer based on the Novel Discrete Orthogonal Transforms", presented at the 15th International Conference Electronics, May 17-19, 2011, Kaunas, Lithuania. Submitted for publication in proc. Electronics and Electrical Engineering. - Kaunas: Technologija, 2012, No. X (112), 6 pages.

[5.3.1] A. Aboltins, “Comparison of Orthogonal Transforms for OFDM Communication System”, presented at the 15th International Conference Electronics, May 17-19, 2011, Kaunas, Lithuania. Proc. Electronics and Electrical Engineering. - Kaunas: Technologija, 2011, No 5, 2011, pp.77-80.

[5.3.2] A Aboltins, P. Misans, "Singular Value Decomposition Based Phi Domain Equalization For Multi-Carrier Communication System", presented at the RTU 52th International Scientific Conference, section on Electronics and Telecommunications, Riga, Oct. 13-14, 2011, Latvia, 5 pages, in press.

[5.4.1.] U. Derums, P. Misans, "Virtual Image Analyzer-Synthesizer Based on the Novel Discrete Orthogonal Transforms", presented at the 15th International Conference Electronics, May 17-19, 2011, Kaunas, Lithuania. Submitted for publication in proc. Electronics and Electrical Engineering. - Kaunas: Technologija, 2012, No. X (112), 6 pages.

6 Tuvas darbības sakaros izmantojamo radioviļņu izplatīšanās modeļu nepilnību un zemas ticamības novērtēšana

The results obtained in this period:

- Ranged models and parameters of radio wave propagation models in the slow fading environment. Section 6.1
- Performed analysis of Doppler frequency shift parameters of radio wave propagation models in the slow fading environment. Section 6.1.
- Usability analysis of available spectrum for software defined radio for north-east part of Latvia. Section 6.2.

Results obtained have shown the attenuation level for static conditions in the multipath environment. i.e. without the motion. Further analysis will perform the multipath attenuation estimation for communication equipment in the case of motion.

6.1 Ranged Models for slow fading environment with Doppler frequency shift.

In general a number of models have been introduced along the lines of a general Hata–like power law such as:

$$L = L_1 + 10 \times \log\left(\frac{d}{d_1}\right)$$

where L_1 – the path loss at a reference distance *d1* of 1, 10 m or 100 m dependent of the scale of analysis. For a small scale of indoor object the reference distance have been stated as *d1*=1 m, for medium – 10 m, for large scale – 100 m. A *d* is distance. A propagation coefficient n is used to fit to the experiments.
Exponential attenuation model has been used as

$$L = L_1 + \alpha d$$

where α is path loss exponent and *d* is distance in meters.
Measurements at different frequencies: 850, 1900, 4000 and 5800 MHz in a large building have been performed. The path loss was matched to model with attenuation values: 0.54; 0.49 and 0.62.
Comparison with measurements shows standard deviation of an error around 10 dB for both models.
Conclusion. More accurate error estimation in static case and estimation of error for moving objects in the further evaluation is required.

6.2 Available spectrum for software defined radio for north-east part of Latvia.

Traditional hardware based radio devices limit cross-functionality and can only be modified through physical intervention. This results in higher production costs and minimal flexibility in supporting multiple waveform standards. By contrast, software defined radio technology provides an efficient and comparatively inexpensive solution to this problem, allowing multimode, multi-band and/or multi-functional wireless devices that can be improved using software upgrades.

The World Radio Conference is the venue for adapting the Radio Regulations, which declares cross-border aspects of the use of the radio spectrum, determining which uses have to adapt to other uses across an international border. All EU Member States are also

ITU members and play an active part in adapting the Radio Regulations. The next conference will take place in Geneva from 23 January to 17 February 2012.

This WRC agenda item concerns cross-border coordination of the use of spectrum in the upper part of the digital dividend (790–862 MHz). There is a representation of digital terrestrial TV channels (East-European distribution) used across Latvia. Last 6 channels fit in the band for digital dividend. The effective use of part of the digital dividend along the EU's eastern border is hampered by the use of a dated aeronautical navigation system in the same band on the other side of the border.

The EU should aim for fair coexistence between future uses on either side of the borders, enabling full use of the 790–862 MHz band for SDR or wireless broadband throughout the EU.

References

[6.1] G. Balodis EMC emission and imunity testing. Public Service Review. European Union. Nr. 21, 2011, pp. 638-639.

[6.2] G. Balodis H. Zeiļaks SDR in Riga Technical University. Public Service Review. European Union. N.22, 2011, pp. 622-623.

7 Trafika piekļuves sistēmas buferatmiņas apjoma un kanāla caurlaidspējas novērtēšanas algoritma un programmatūras izstrāde informācijas pārraides ātruma uzlabošanai, rīku izstrāde transporta līdzekļu pozicionēšanas precizitātes paaugstināšanai, kas kopā ļaus palielināt transporta plūsmu vadības efektivitāti

7.1 Rīku izstrāde transporta līdzekļu pozicionēšanas precizitātes paaugstināšanai

7.1.1 Rīku izstrāde transporta plūsmu vadības efektivitātes uzlabošanai

In 2011, our group had developed radar with a continuous unmodulated radiation (CW-Radar - Continuous Wave Radar) and of radar with a frequency modulation (FMCW-Radar – Frequency Modulation Continuous Wave Radar), designed to remote traffic count and speed of vehicles by means speed trajectory [7.1].

It was shown experimentally that for the registration of current number of vehicles and their speed for both directions it is more appropriate to use CW-radar, but not the FMCW-radar, as it is more resistant to noise of receiver and interferences that arise due to imbalance of phase and amplitudes of quadrature output IQ-mixer, because of the side-lobe antenna and reflections from low Doppler and stationary targets.

For CW and FMCW-radars software for signal records processing have been developed. Suggested design and processing software is currently implemented in the programmable logic integrated devices (PLD) FPGA Xilinx inside of the working prototype.

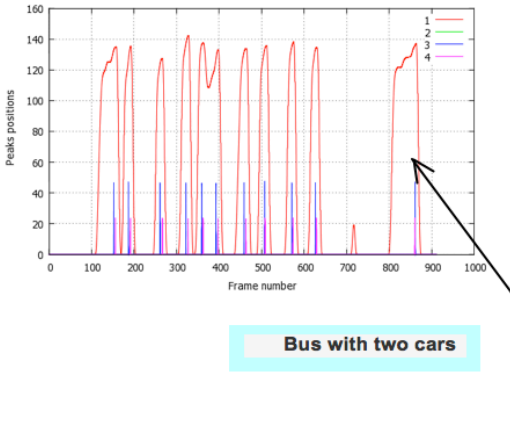

Fig 7.1. Example of CW-radar signal processing for speed trajectory in the direction “Left-to-Right”

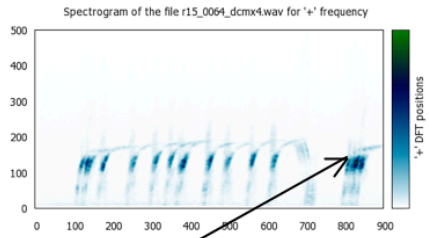

Fig 7.2. CW-radar signal for spectrogram in the direction “Left-to-Right”

Figure 7.1 is an example of a speed trajectory, obtained after processing of signal CW-radar for vehicle traffic in the direction "Left-to-Right" and in Figure 7.2. is shows the spectrogram of the same signal. The bus is clearly distinguished from two cars. The working model of the CW-radar was tested in the city and has shown good results. See [7.1] for more detail.

7.1.2 MEMS sensoru tīklu izpēte objekta orientācijas noteikšanas. MEMS sensor network research for object attitude estimation.

An important step for mobile sensor network developing is appropriate sensor and data fusion algorithm selecting. Different MEMS sensor network structures were analyzed for object attitude estimation. There are 3 accelerometers, 3 gyroscopes, 3 magnetometers in the sensor network. Output signals from each sensor were recorded on HDD of notebook for post-processing. Sensor data rate was 50Hz.

Quaternion based attitude algorithm was used for object pitch, roll and yaw estimation [7.3]. Kalman linear algorithm was used for MEMS gyroscopes and MEMS accelerometers data fusion [7.4, 7.5].

The object was fixed on tilt table with pitch $\theta=0°$ and roll ϕ =39.5° during experiments.

The results of pitch and roll estimation using gyros data are shown in Figure 7.3

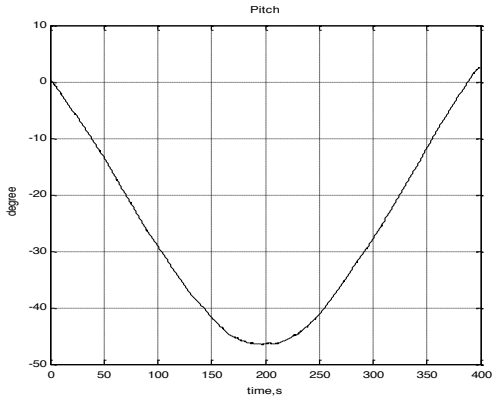

Fig.7.3 Pitch estimation

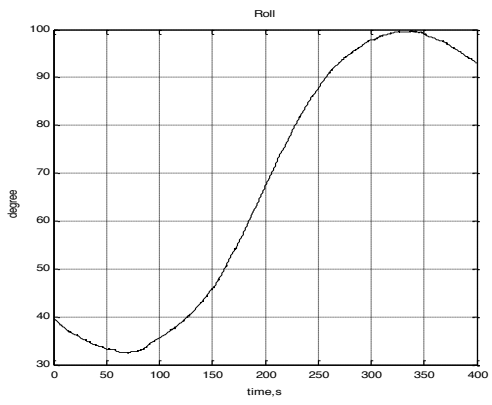

Fig. 7.4 Roll estimation

As we can see from Figures 7.3 and 7.4 the pitch and roll estimation error is high and even uncontrolled.

The results of pitch and roll estimation using gyro and accelerometer data are shown in Figures 7.5 and 7.6. In this case linear Kalman filter was used for sensor data fusion.

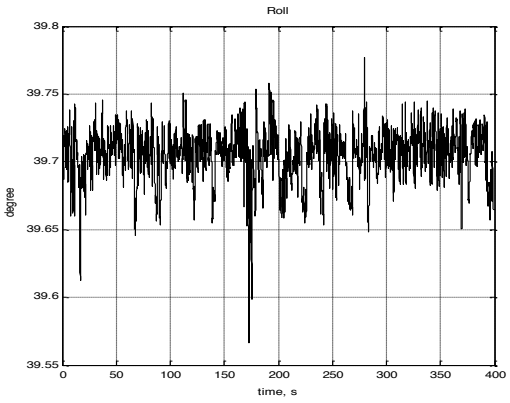

Fig. 7.5 Roll estimation

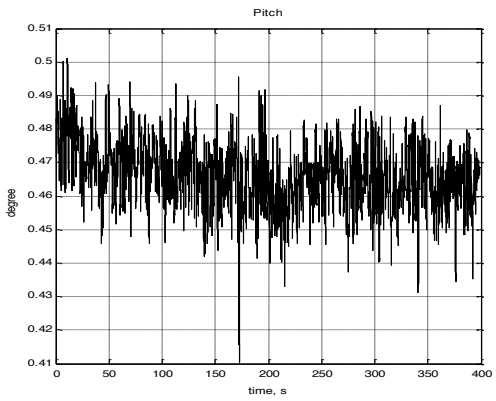

Fig. 7.6 Pitch estimation

In this case the estimation of pitch and roll is sufficiently accurate for applications in land object navigation algorithms. The statistical characteristics of estimated attitude angles values are shown in the Table 7.1

Table 7.1 Statistical characteristics of estimated roll and pitch

Statistical characteristics, degree, [°]	**Roll**	**Pitch**
Mean value	0.4661	39.7052
Standard deviation	0.0095	0.0188

In order to validate algorithm for yaw estimation using magnetometer data, the object was rotated around Up-axis of local coordinate frame North-West-Up. The MEMS gyroscopes data cannot be used for yaw estimation due to the high level of internal (sensor) noise. The yaw estimation using magnetometers data is shown in Figure 7.7.

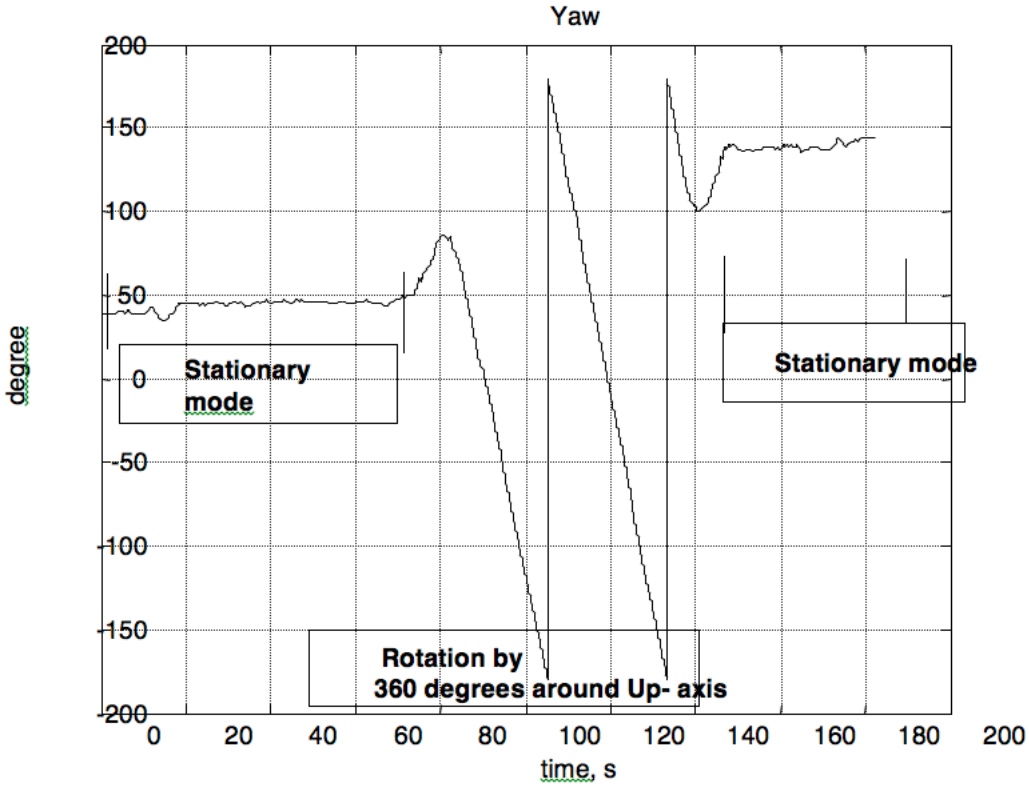

Fig. 7.7 Yaw estimation

The experimental results show that 3 accelerometers and 3 gyroscopes and 2 magnetometers are required in order to provide altitude estimation data suitable for land mobile object navigation tasks (To remind MEMS sensors are considered in this research). If object is in stationary mode, then only data from 3 accelerometers and 2 magnetometers is necessary to provide object attitude estimation.

The noise characteristics of MEMS sensors are not simple and require special methods for it reduction and identification. This is very important as high sensor noises result in high errors of estimated parameters. This is highly undesirable for navigation application. The future work will be devoted for analyzing estimation error decreasing effect from combining sensor noise reduction special algorithms and data fusion algorithm.

7.1.3 GPS satelītu sistēmas ar fāzu mērījumiem precizitātes pētījumi

The GRS-1 receiver was used for the measurements. Measurements have been made by different solution types. These types are fixed, float and DGPS. The Re-reference system was used to retranslate the satellite signal from outside antenna to inside antenna. So if there is known the precise coordinates of outside antenna, it is possible to determine receiver's accuracy. Measurements that are made in auditory are shown in Figure 7.8. GRS-1 receiver accuracy is shown in Figure 7.9 and measurement's root mean square error is shown in Figure 7.10. It follows that the centimeter accuracy could get by using fixed solution type. While decimeter accuracy we could get by using float and DGPS solution type.

To know how precise GRS-1 receiver is outside, we should make the measurements at the well-known geodetic points. So this is the next task to do.

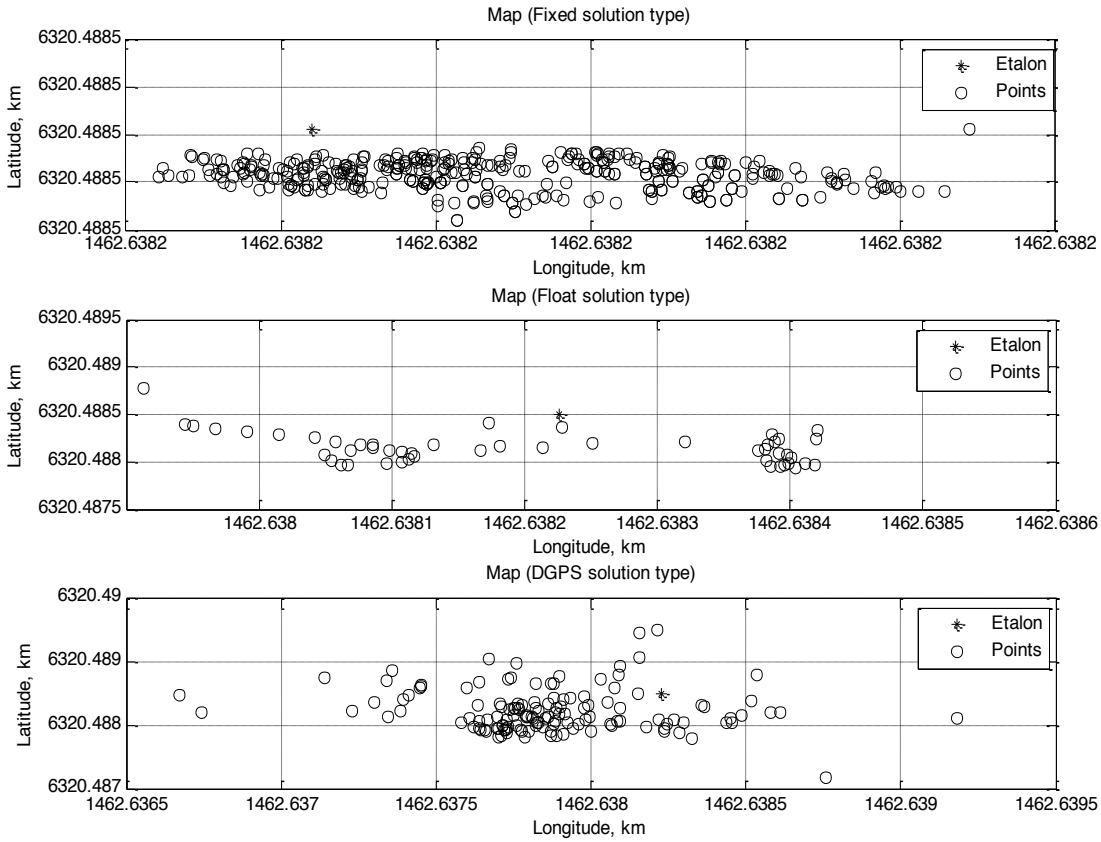

Fig.7.8. Measurements interpretation

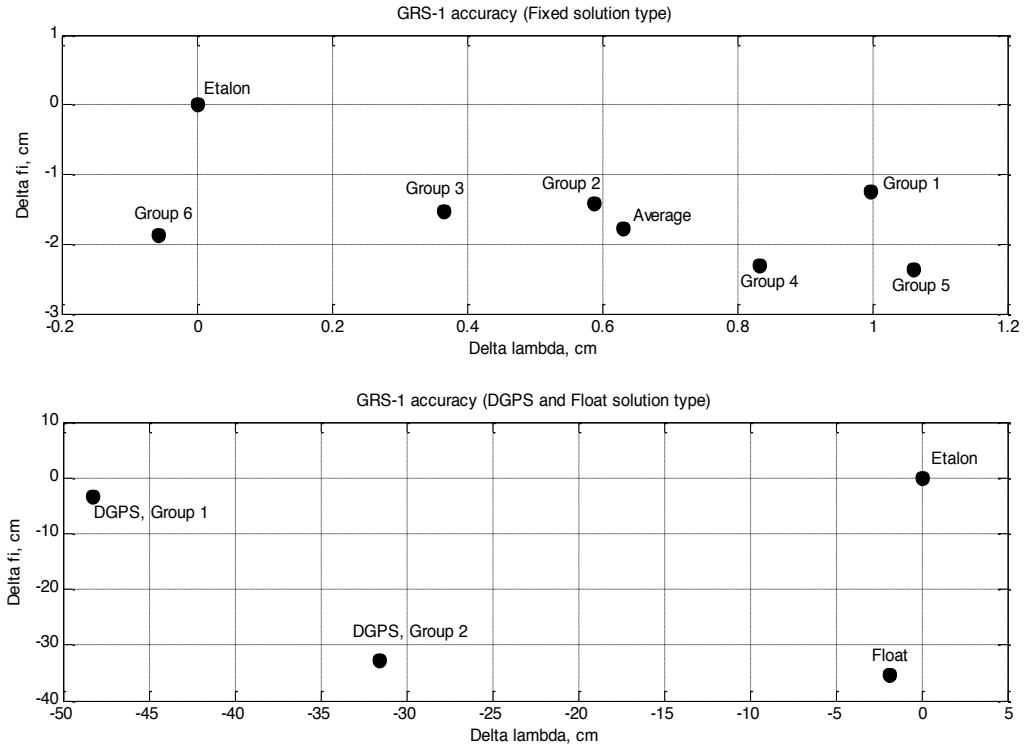

Fig.7.9. GRS-1 receiver accuracy

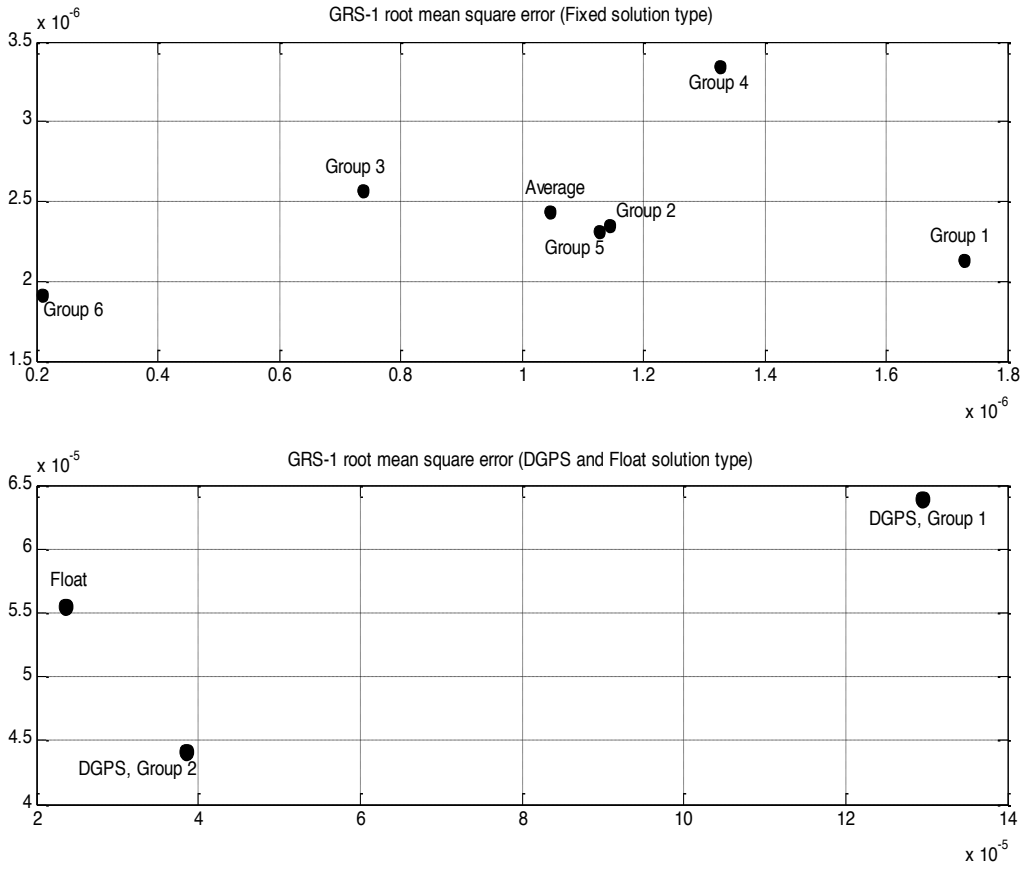

Fig.7.10. GRS-1 receiver root mean square error

7.1.4 Slīdošā loga un adaptīvā Kalmana filtra metodes salīdzinājumi dinamisko koordinātu datu filtrācijai. Comparison of LSM and Kalman filter

To compare these two methods, we use two values – estimated position and estimation root square error. We start with simplest case, when both filters has no adaption and LSM uses constant window length w=50, see Figure 7.11 and Figure 7.12.

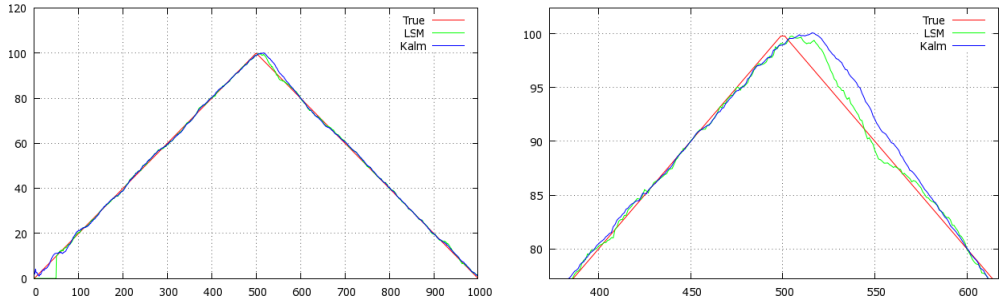

Fig.7.11 No adaption for both filters LSM window is constant w=50.

As we can see both methods improves results. We can reduce LSM max estimation error, if decrease constant window. For example from w=50 to w=10. Results are shown in Fig.7.12 and Fig.7.13.

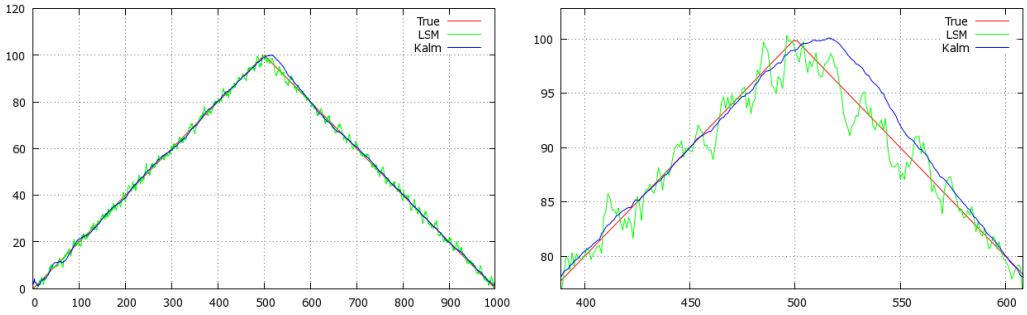

Fig.7.12 No adaption for both filters, LSM window is constant w=10.

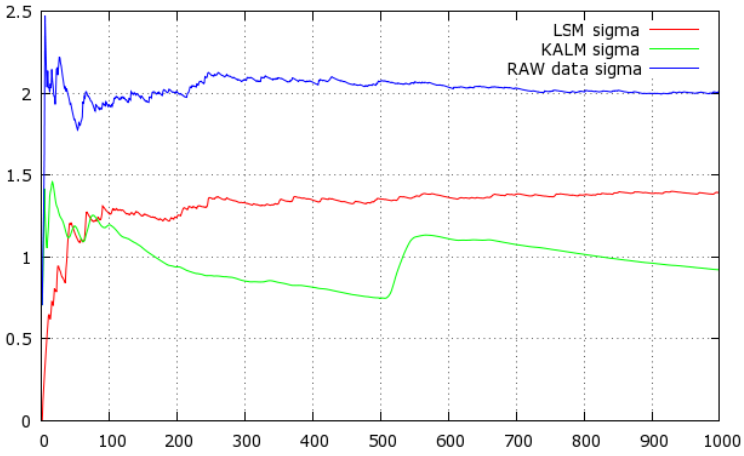

Fig.7.13 σ calculation. No adaption for both filters, LSM window is constant w=10.

Results are better, but now there are "saw" effect in LSM results and we use expressions (3) to make adaptive LSM. Results are shown in Figure 7.14 and Figure 7.15.

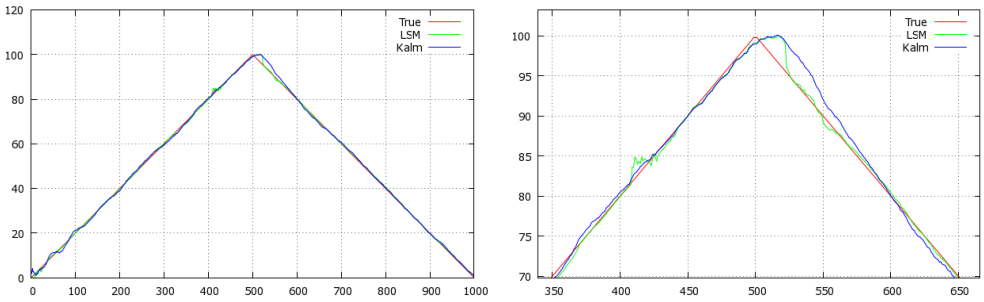

Fig.7.14 LSM has adaption using expressions (3), sliding window starts with w=10. Kalman filter has no adaption.

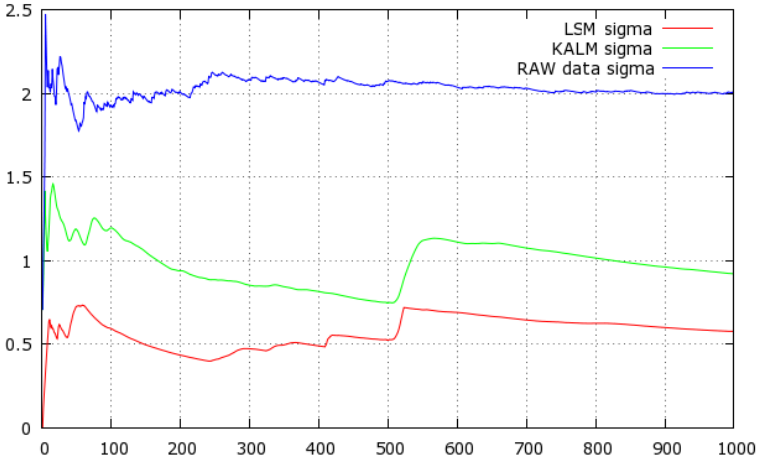

Fig.7.15 σ calculation. LSM has adaption using expressions (3), sliding window starts with w=10. Kalman filter has no adaption.

As we can see, if there is just one source of information, both methods give very similar results. However, Kalman filter has an advantage, that we can estimate velocity by using the same source of information or another source, for example inertial sensor [7.2]. And we expect that result will be much better, if we add second independent source of information for velocity. That is a part of future work.

7.2 Trafika piekļuves sistēmas buferatmiņas apjoma un kanāla caurlaidspējas novērtēšanas algoritma un programmatūras izstrāde informācijas pārraides ātruma uzlabošanai.

The main purpose of the present research is the development of managing algorithms in the control system that admits data flows to communication resources, thus providing the required quality of service. The algorithms covered in the study are admission control and flows redistribution, the algorithms of resources redistribution and maximization of system load that lead to fulfillment of quality of service requirements.

The research resulted into elaboration of recommendations regarding optimization of admission control system functioning. In order to test the recommendations an OPNET modeling system has been applied.

The work on the project is based on previous work of Mihail's Kulikov's doctoral studies and diploma thesis [7.6]. This work provides control mechanism suggested by the author, which has been undergoing further research.

The effectiveness of the proposed algorithm has been tested in OPNET modeling framework. For modeling, according to Figure 7.16, the network with managed switch has been created. The algorithm has been realized as additional modules integrated in the switch. The performance has been tested on the basis of the scenario described in [7.6] traffic is created by the users of VoIP applications.

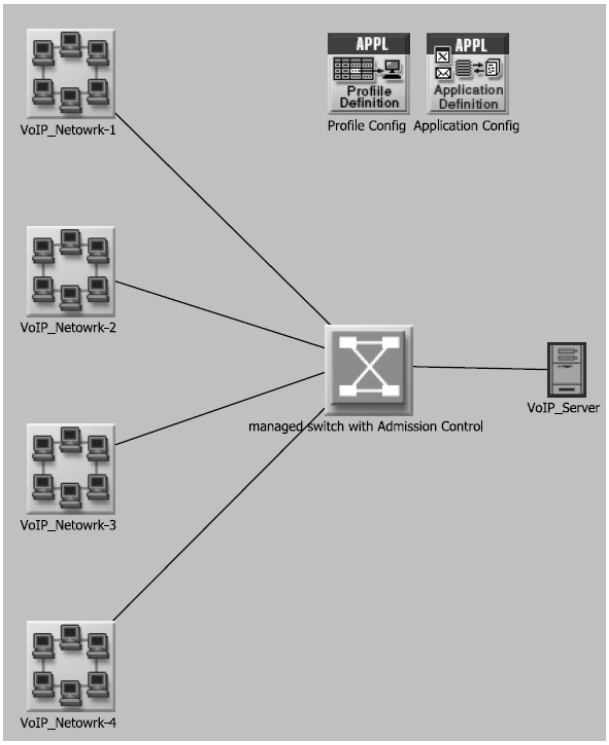

Fig. 7.16. The OPNET Project for VoIP Scenario.

It has been shown that for measurement based admission control the critical factor affecting the accuracy of the decision making, is the measurement window. The qualitative comparisons of the network performance with different admission control methods measurement window are presented in [7.6]. The results match the hypothesis that the best results can be gained while adaptive to traffic parameters window measurement is applied. The example of time delay for data packets in VoIP application depending on traffic parameters window length is depicted in Figure 7.17 for various values of this window length.

The best window measurement equals correlation interval. Also, simulation results prove that the costs of the correlated traffic, related to measuring process, can be decreased. That is supported by the proposed solution.

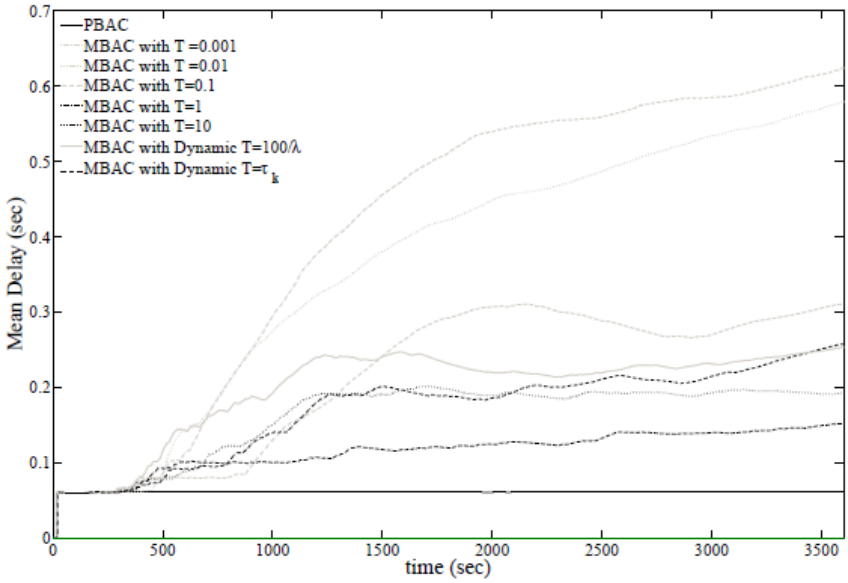

Fig. 7.17. The mean value of delay in queue for different AC parameters

Designed recommendations and results of give significant scope for future work and especially in wireless environment.

References

[7.1] А.В.Зеленков, Дидзис Лиепкалнс, А.Ершов, А.Маклаков. Разработка и экспериментальная проверка автоматического радилокационного регистратора числа и скорости транспортных средств на встречных направлениях движения //"Автоматика и вычислительная техника", 2012, in print

[7.2] A.Kluga, J.Kluga. Dynamic Data Processing with Kalman Filter. Electronics and Electrical Engineering- Kaunas: Telecommunications Engineering. - No. 5(111). (2011) pp. 33-36.

[7.3] Paul D. Groves, *Principles of GNSS, Inertial, and Multisensor Integrated Navigation Systems*. London: Artech House, 2008

[7.4] Priyanka Aggarwal, Zainab Syed Aboelmagd Noureldin and Naser El-Sheimy, *MEMS-Based Integrated Navigation.* London: Artech House, 2010.

[7.5] V. Bistrovs, "Analyse of Kalman Algorithm for Different Movement Modes of Land Mobile Object" , Electronics and Electrical Engineering. Kaunas: Technologija, No. 6(86) , pp. 89–92, 2008.

[7.6] Kuļikovs, Mihails. Piekļuves kontroles sistēmu efektīvu vadības algoritmu pētīšana un izstrāde telekomunikāciju tīkliem: promocijas darbs / M.Kuļikovs ; zinātniskais vadītājs E.Pētersons; Rīgas Tehniskā universitāte. Elektronikas un telekomunikāciju fakultāte. Transporta elektronikas un telemātikas katedra. Rīga: [RTU], 2010. 200 lpp.

8 Datplūsmu efektīvas pārraides risinājumu izpēte mobilos bezvadu ad-hoc tīklos (MANET) ievērojot m-pakalpojumu kvalitātes (QoS) nodrošināšanas kritērijus sadarbības scenārijiem.

Mobile Ad-hoc Networks (MANET) have a dynamic and unstable nature because nodes can be mobile, appearing and disappearing, can experience mutual interference if several nodes are trying to communicate at the same time and so on. Multimedia data transmission in such networks is a complicated task. One of the possible solutions for increasing throughput between the source and the destination is the implementation of multi-path routing.

Even if multi-path routing is used there are several issues to be solved. Mutual interference of nodes may appear in case if two or more routes are used simultaneously and their nodes are no radio disjoint (creating mutual interference). It is also not clear what is the optimal number of routes and which is the most efficient method for multi-stream video coding for multimedia data transmission.

In this work analysis was made to elaborate criteria for selecting an optimal number of routes and the appropriate coding method for video stream transmission. A special focus is placed on QoS provision as one of the most important characteristics in videoconferencing.

The Carrier Sense Multiple Access with Collision Avoidance (CSMA/CA) protocol may cause inter-node interference. Effectiveness of multipath routing with adaptive carrier sense method was investigated comparing results of simulation and experiments in wireless network test-bed.

The results obtained in this period:

1. Analysis performed of multi-path multimedia mobile service (m-service) data transmission methods over MANETs
2. Developed an efficient data transport method over MANET using Multi-path routing with adaptive carrier sense
3. Created a wireless ad-hoc network test-bed. Computer simulation and experiment performed in the test-bed with multi-path data transport.

Future research is planned using created test-bed for experimentation in combination with computer simulation. Research aims to increase an efficiency of multimedia data transport over multiple paths in MANETs using inter-layer linking and cognitive radio techniques.

8.1 Analysis of Multi-path Multimedia Mobile Service (M-service) Data Transmission Methods over MANETs

Multimedia data transmission in MANETs is a very complicated task because existing transport and routing protocols are not well suited for this task. Variable link capacity, dynamic nature, lack of centralized infrastructure and energy constraints of MANETs make the QoS provision over these networks a difficult task.

Multi-path routing can decrease the end-to-end delay and packets loss, jitter, delay time, the data transmission rate that are very important quality metrics (parameters) to

maintain QoS in video streaming. For introducing multi-path routing video stream must be, first, divided to Multiple Streams using one of coding methods and then transmitted using one of multi-path routing protocols.

Coding technology is important for media streaming QoS, which mainly includes Layered Coding, Multiple Description Coding, Scalable Coding and Network Coding:

- *Layered (video) coding* (LC) encodes video into several layers. The base layer (BL), which includes the crucial part of the video frames, guarantees a basic display quality. Each enhancement layer (EL) correctly received improves the video quality [8.1].
- *Multiple Description Coding* (MDC) generates multiple equally important streams, each giving a low but acceptable quality. A high-quality reconstruction is decodable from all bit streams together, while a lower but still acceptable quality reconstruction is achievable if only one stream is received [8.1].
- *Scalable Video Coding* (SVC) is a layered video codec and extension of the H.264/AVC [8.2] video coding standard. SVC support heterogeneous devices that use a scalable bit stream, which consists of a base layer and one or several enhancement layers. SVC standard provides the encoding of a high-quality video bit stream that contains one or more subgroups of bit streams that can be decoded with lower quality.
- *Network Coding* (NC) divides video flows into several data fragments, encodes and then send them out. For original video recovering it is necessary to receive linearly unrelated data, but there is no need in received/scheduling data blocks IDs [8.3].

The most popular protocols for multi-path transport are:

- a-MMDSR (adaptive-Multi-path Multimedia Dynamic Source Routing) protocol includes cross-layer techniques which improve the end-to-end performance of video-streaming services over IEEE 802.11e Ad Hoc networks [8.4].
- RDM (Radio Disjoint Multi-path) protocol provides purely radio disjoint paths (no nodes in the interfering range of each other), what is very important while using multiple routes simultaneously [8.5].
- MP-OLSR (Multi-Path Optimized Link State Routing Protocol) [8.6].

Comparison of different coding methods and routing protocols lead to following conclusions:

- MDC has a large bandwidth overhead, but better adaptation to heterogeneity than LC, large data repetition and very good improvement for fault-tolerance. LC has a smaller bandwidth overhead than MDC, good adaptation to heterogeneity, smaller than MDC data repetition and good improvement for fault-tolerance.
- If loss rates are high (above 10%) and channel condition is very bad, what is typical for MANET, MDC outperforms other coding schemes when FEC-based error protection is applied. When there is a large number of nodes (~ from 120 nodes), MDC with MP-OLSR using 4 paths simultaneously is the best solution for multimedia data transmission over MANET with QoS provision.

More detailed analysis is presented in the paper [8.7].

8.2 Efficient Data Transport over MANET using Multi-path Routing with Adaptive Carrier Sense

The CSMA/CA protocol was designed to reduce the collision probability between multiple nodes accessing a medium. A collision occurs at a receiver side if it receives packets simultaneously from multiple sources. Physical carrier sensing at transmitter side is performed to avoid such situation. When node wants to transmit, it senses the allocated frequency channel by monitoring RF signal level. If transmission by another node is sensed, transmission is deferred. Distance in which an eventual interference in the channel is sensed depends on physical carrier sense threshold (PCST). Although PCS method helps to prevent collisions, it may defer possibly successful transmissions due to "exposed station" problem [8.8, 8.9].

To avoid exposed station problem and thus increase network throughput, adaptive PCS mechanism could be used to tune PCST after every change in network topology, thus minimizing a number of nodes deferred from transmitting [8.8, 8.9]. RF interference level is monitored at each node and communicated between neighbours to choose some optimum threshold value, which is a minimum value from all offered values.

Multi-path routing is another approach to avoid limitations created by PCS. Instead of using one path, video traffic can be sent over multiple paths, thus distributing load. However, such approach works only if paths are radio disjoint. It means that paths must be selected so that there is no mutual RF interference between them. Otherwise if node of one path senses ongoing transmission in other path, transmission is still deferred. Such phenomenon is called route coupling.

Multi-path routing effectiveness has been analyzed comparing throughput of single and multi-path routing conditions through NS2 simulations. Simulation show that compared to single path, two high-interfering paths could increase throughput only by 12% but low-interfering paths about 65% [8.10].

Inter-path interference can be reduced if multi-path routing is used together with adaptive PCST. In our previous work [8.11] we proposed method where PCST is dynamically adjusted after path selection so that inter-path interference is prevented. That would allow decreasing the distance between paths, thus making path selection easier.

8.3 Computer Simulation and Experiment with Multi-path Data Transport over MANET

Wireless network test-bed consisting of 6 nodes in 2 parallel paths (3 nodes in each path) was created for experiments. Two laptop computers were used for data generation and monitoring. The same network configuration was used for simulation using NS2 software.

To simulate network traffic two FTP data transfer sessions were started (one for each path). Standard TCP transport protocol was used. Simulation parameters are summarized in the Table 8.1.

Table 8.1. NS2 simulation parameters

Nodes	6
Simulation time	110s
First FTP session period	10s - 100s
Second FTP session period	40s - 70s
Distance between nodes	10m
Inter-path distance	14, 24m
Transmission range	15m
Carrier sense range	25m
Wireless standard	802.11b
RTS/CTS	Off
TCP packet size	1500 bytes

Test-bed consists of 6 Cisco Linksys WRT160NL wireless routers equipped with Atheros AR9102 wireless network interface. Router has enough system memory (32 MB RAM and 8 MB flash) for firmware upgrade to more sophisticated platforms.

Two tests were performed each with different inter-path distance:

- d_{PATH}=14m. It is the distance at which maximum inter-path interference is possible. PCS areas of nodes overlap and therefore every node "hears" all the other nodes in the network.
- d_{PATH}=24m. Minimum inter-path interference is maintained. Every node hears only 3 neighbours (2 from own path and 1 from opposite).

RTS/CTS handshake was switched off because as pointed out in [8.11] it is ineffective for wireless ad-hoc networks and traffic overhead it creates decreases network *goodput*.

The experiment parameters are summarized in Table 8.2.

Table 8.2. Experiment parameters

Frame size	1500 bytes
RTS/CTS	Off
Inter- path distance	7, 23m
Distance between nodes	5m
Transmitter power	1mW
Transmission range	5-10m
First Iperf TCP session period	10s - 100s
Second Iperf TCP session period	40s - 70s

Figure 8.1 combines results both from simulation and experiment at high inter-path interference (nodes between two paths are close). One can see that when data transmission over Path 1 takes place (time interval 40-70), then it created interference for Path 2 and throughput of the second path decreases.

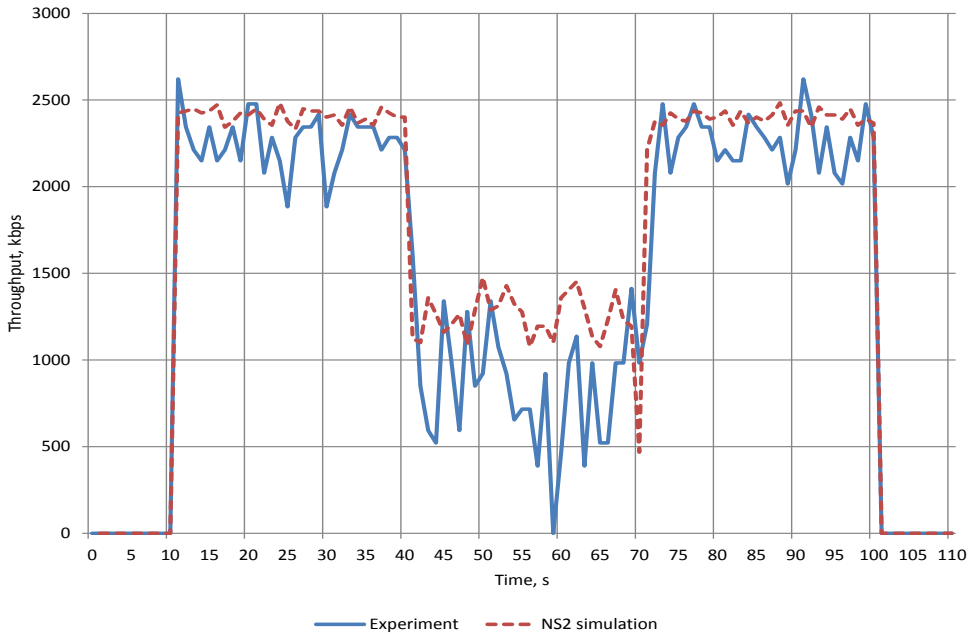

Fig. 8.1. Throughput of the second path at high inter-path interference

NS2 simulation show that throughput of the second path should reduce approximately by half during the interference period. Such distribution is logical because of symmetric topology. However, experimental measurements show that throughput drop in the second path is even greater, at the same time throughput of second path is higher. It means that second path has greater impact on first than vice versa. That could be explained by imperfect experiment conditions, example, direction of antennas, uneven ground etc. and it must be clarified in future experiments. Still the most important conclusion is that total throughput of network didn't change when the second path is added. Sum of the throughput in both paths is about 2500 kbps.

Figure 8.2 shows throughput of the second path in situation when there is a low inter-path interference. It was achieved by increasing distance between paths.

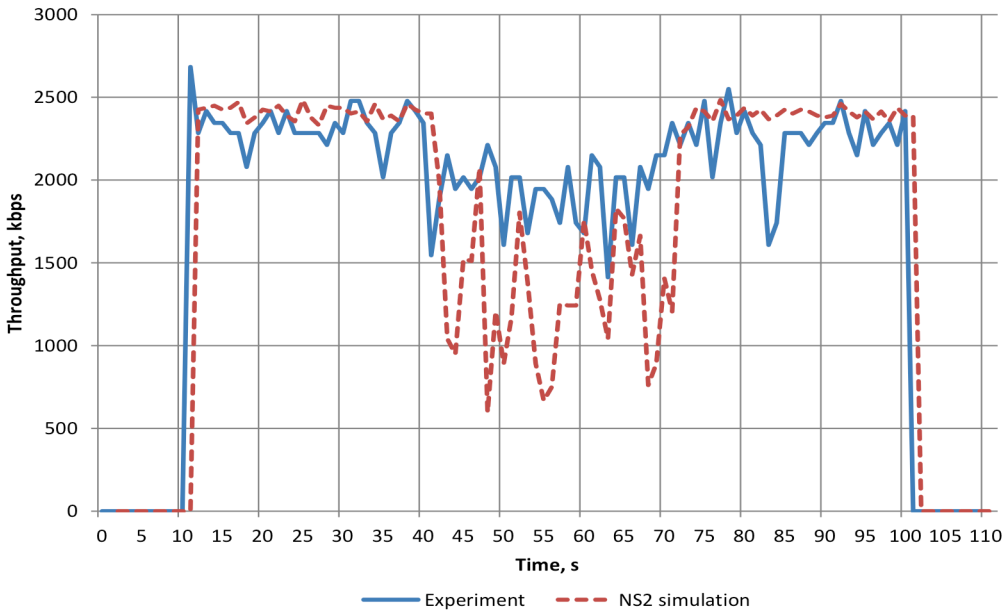

Fig. 8.2. Throughput of the second path at low inter-path interference

From above figures one can see that experimentally measured throughput reduces less during interference period. Simulated threshold still drops at 50% level.

More detailed description of the simulation, test-bed, experiment and result could be found in [8.12].

8.4 References

[8.1] S. Mao, S. Lin, S. S. Panwar, Y. Wang, E. Celebi. Video Transport over Ad Hoc Networks: Multistream Coding with Multipath Transport // IEEE Journal on Selected Areas in Communications. IEEE, 2003. Vol. 21. No. 10, pp. 1721-1737.

[8.2] Advanced Video Coding for Generic Audiovisual Services, ITU-T Recommendation H.264 & ISO/IEC 14496-10 AVC, v3: 2005.

[8.3] Y. Guangxue, J. Tao, L. Renfa , C. Zhi, S. Jiajia, X. Cheng. Underlying Technology of P2P Media Streaming, Journal of Networks, Vol. 6, No. 8, August 2011. pp. 1195-1205.

[8.4] M. A. Igartua, V. C. Frías, Self-configured multipath routing using path lifetime for video-streaming services over Ad Hoc networks, Elsevier B.V., 2010.

[8.5] K. Kuladinithi, Wireless Multi-hop Ad hoc Networks: Evaluation of Radio Disjoint Multipath Routing, Dissertation, December 2009.

[8.6] E. Cizeron, S. Hamma, MP-OLSR: Multi-Path OLSR for Mobile Ad hoc Networks, IEEE Wireless Communications and Networking Conference (2009)

Volume 3, IEEE, pp. 2235-2240.

[8.7] S. Vdovins, I. Slaidins, L. Cikovskis. Optimal Multipath Routing for Multimedia Data Transmission over MANET with QoS Provision. (To be published in The Scientific Journal of RTU. Series 7. Telecommunications and Electronics).

[8.8] C. Thorpe, S. Murphy, L. Murphy "IEEE802.11k Enabled Adaptive Physical Carrier Sense Mechanism for Wireless Networks (K-APCS)," in Proceedings of the 4th ACM International Workshop on Performance Monitoring, Measurement, and Evaluation of Heterogeneous Wireless and Wired Networks, 2009, pp.209–215.

[8.9] J. Zhu, X. Guo, L. Yang, "Adapting Physical Carrier Sensing to Maximize Spatial Reuse in 802.11 Mesh Network," in Wireless Communications and Mobile Computing, Vol. 4, Issue 8 : John Wiley & Sons Inc., 2004. pp. 933–946.

[8.10] Y. H. Wang, H. Z. Lin, S. M. Chang, "Interference on Multipath QoS Routing for Ad Hoc Wireless Network," in Proceedings of the 24th International Conference on Distributed Computing Systems Workshops, Vol. 7, No. 1, 2004, pp. 104 – 109.

[8.11] L.Cikovskis, S.Vdovins, I.Slaidiņš. "Multipath Routing with Adaptive Carrier Sense for Video Applications in Wireless Ad-hoc Networks, " in Electronics and Electrical Engineering, 2011. No.6, Lithuania, Kaunas, 2011, pp. 37-42.

[8.12] L. Cikovskis, I. Slaidins. Impact of Physical Carrier Sense Range on Network Throughput in Wireless Ad-hoc Networks. (6 pages, to be published in The Scientific Journal of RTU. Series 7. Telecommunications and Electronics, 2011)